S E D	12861	WILEY	Dispatch: 19.3.21	CE: Gomathi
Journal Code	Manuscript No.		No. of pages: 53	PE: Sudhakar G.

Sedimentology (2021) doi: 10.1111/sed.12861

Depositional and early diagenetic characteristics of modern saline pan deposits at the Bonneville Salt Flats, Utah, USA

JEREMIAH BERNAU* and BRENDA B. BOWEN*†
*Geology and Geophysics, University of Utah, Salt Lake City, UT, USA (E-mail: jeremiahbernau@gmail.com)
†Global Change and Sustainability Centre, University of Utah, Salt Lake City, UT, USA

Associate Editor – Giovanna Della Porta

ABSTRACT

The Bonneville Salt Flats form a saline pan in western Utah, USA. This modern saline pan has a unique history of land-speed racing and potash mining. Multi-decadal measurements record decreasing evaporite volume and extent, spurring multiple environmental studies. The goal of this work is to describe saline pan evaporite morphologies within the context of environmental measurements. Environmental data include field observations, groundwater and dust trap samples, precipitation, albedo, time-lapse photography, groundwater level, and temperature measurements of air, groundwater and the shallow evaporite crust. Petrographic data include thick sections, evaporite slabs and sediments, and X-ray computed tomography of evaporites. Diverse halite morphologies are formed at the surface, vadose and phreatic zones. The presence and preservation of these morphologies are influenced by spatially heterogenous natural and anthropogenic processes, including daily to seasonal changes in brine salinity, mineral saturation states, and water level within and across saline pan stages. In addition to hydrological balances delineated by the saline pan stages of flooding, evapoconcentration and desiccation, changes in vertical brine movement, temperature and surficial sedimentary structures influence evaporite morphologies. These results are transferable to the interpretation of altered evaporites and enhancing saline pan depositional models.

Keywords Brine, diagenesis, evaporates, petrography, saline pan, salinity, syndepositional.

INTRODUCTION

The Bonneville Salt Flats (BSF), Utah, USA, is a saline pan composed of bedded halite and gypsum sand (Fig. 1). Competing land uses have motivated studies and characterizations of this dynamic landscape since 1960 (e.g., Bowen *et al.,* 2017, 2018b). Multi-decadal decreases in saline pan thickness and extent leave questions about the role of natural and anthropogenic processes in altering the evaporites and how evaporite sedimentary structures are changed by prolonged periods of dissolution. Petrographic examination of evaporites paired with environmental measurements help to address these questions.

Evaporite minerals and depositional records are highly sensitive to environmental conditions. Petrographic and process-based studies of saline pans aid interpretation of evaporite morphologies. Saline pans are typically dry settings, with evaporite deposits that are influenced by stages of flooding, evapoconcentration, and desiccation (Fig. 2; Lowenstein & Hardie, 1985; Bowen *et al.,* 2017). Evaporites contain fluid inclusions that preserve the depositional temperature, atmospheric composition, and fluid composition and pH from their environment of formation (Fig. 3A;

COLOR

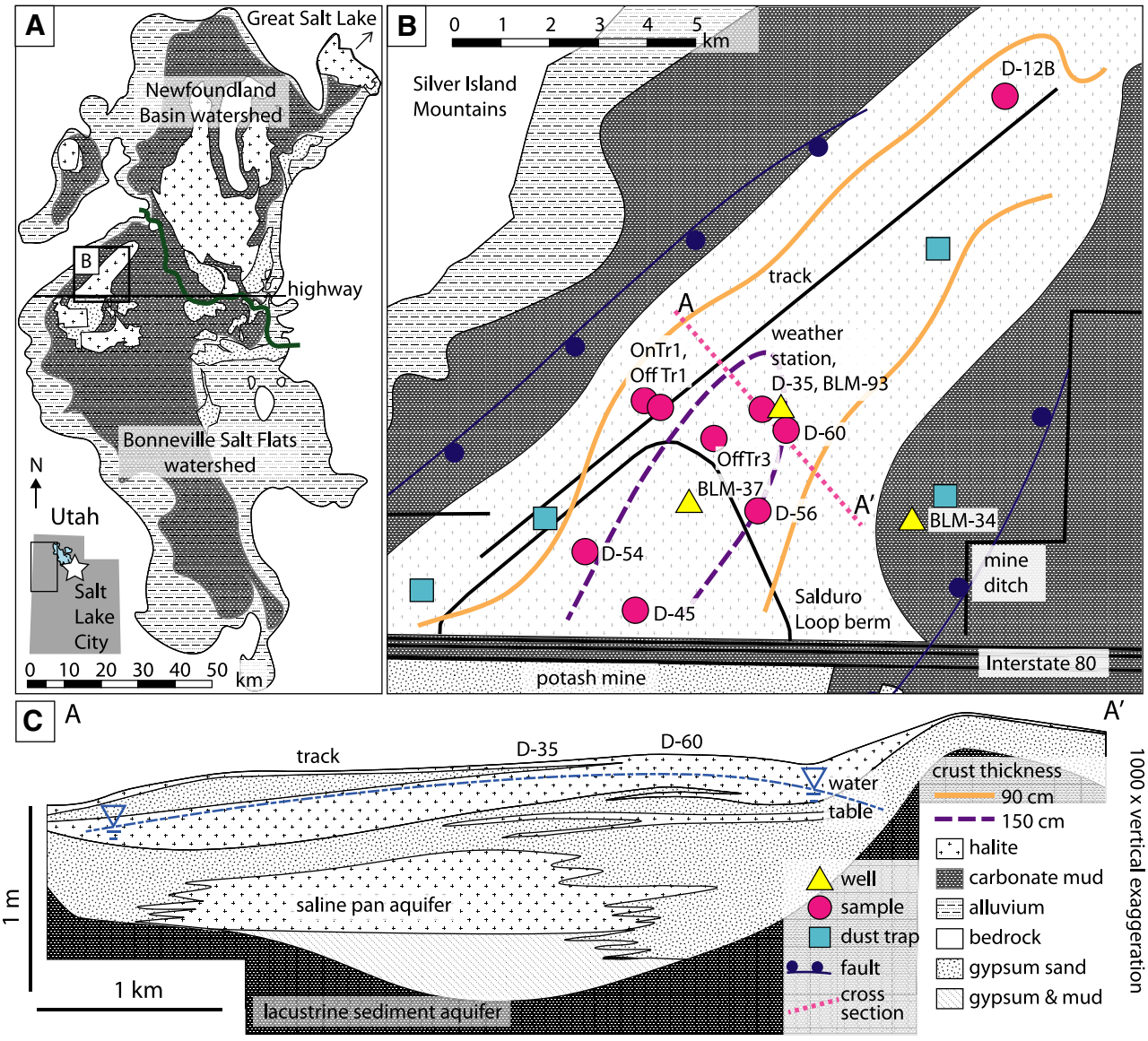

Fig. 1. Overview of the Bonneville Salt Flats and surrounding areas. (A) Location of the Bonneville Salt Flats in the Great Salt Lake Desert, Utah. The Great Salt Lake is north-east of this desert. Salt Lake City (white star) is *ca* 150 km east of the Bonneville Salt Flats. A drainage divide separates the Newfoundland Basin and Bonneville Salt Flat watersheds. Surface mineralogy consists of halite, gypsum, carbonate muds and mixed alluvium (autumn 2016 satellite imagery; Nolan, 1927; Wold & Waddell, 1994; Bowen *et al.,* 2017; Radwin & Bowen, 2021). (B) Overview of Bonneville Salt Flats setting, thickness and sample locations (after Bowen *et al.,* 2018b). Note the potash mine to the south, mine ditch to the east and the arcing Salduro Loop berm at the centre of the saline pan. The saline pan is bounded by the Wendover Graben (dark blue lines; Smith *et al.,* 2012). (C) Highly vertically exaggerated cross-section A – A′ interpreted from eight cores (Bowen *et al.,* 2018b). The surface and sediments dip to the north-west. The water table (dashed blue line; September 2016) is highest near the centre of BSF, which spatially coincides with the thickest surface halite layers. The saline pan aquifer is hosted in saline sediments. The underlying lacustrine aquifer is hosted in carbonate mud sediments. Time lapse imagery was collected at the weather station, the south-east dust trap and well BLM-37.

Rosasco & Roedder, 1979; Roedder, 1984a,b; Lazar & Holland, 1988; Davis *et al.,* 1990; Dubessy *et al.,* 1992; Goldstein & Reynolds, 1994; Roberts & Spencer, 1995; Goldstein, 2001; Lowenstein, 2012). Fluid inclusions also preserve biological material. Petrography constrains the

origin and guides the interpretation of fluid inclusions for palaeoenvironmental investigations. Furthermore, petrographic studies help delineate past fluid flow within evaporite beds, which is critical for siting infrastructure locations for industrial and radioactive waste, oil and gas storage, and carbon sequestration (Powers & Hassinger, 1985; Putnis & Mauthe, 2001; Dashtian *et al.,* 2018).

This work describes the evaporite depositional sequence, syndepositional petrographic features and environmental processes at BSF. This research builds upon decades of saline pan sedimentological research (Lowenstein & Hardie, 1985; Hovorka, 1987; Casas & Lowenstein, 1989; Li *et al.,* 1996; Benison & Goldstein, 1999; Benison *et al.,* 2007). Although these results are focused locally on the data-rich BSF, they describe evaporite morphologies and environmental processes applicable to saline pan depositional models and saline pan deposits' interpretation.

BACKGROUND

Setting

The Bonneville Salt Flats is located in the Great Salt Lake Desert subbasin (on traditionally Newe/Western Shoshone and Goshute lands), part of the Basin and Range physiographic province (Fig. 1A; Dickinson, 2006). The Great Salt Lake Desert, Great Salt Lake, Utah Lake, and Sevier subbasins comprise the Bonneville basin.

In the late Pleistocene, the Bonneville basin was filled by Lake Bonneville, which rose from 30 to 18 cal ka BP to cover a third of Utah (Spencer *et al.,* 1984). As water levels fell from 18 to 11.6 cal ka BP, isostatic rebound raised the topographic threshold between the Great Salt Lake and Great Salt Lake Desert subbasins (Crittenden, 1963; Oviatt, 2015). Only once since *ca* 11.6 cal ka BP have the two subbasins been hydrographically connected (Oviatt, 2014; Oviatt *et al.,* 2015). It is unclear when evaporite accumulation at the Bonneville Salt Flats first occurred (Eardley, 1962).

The Great Salt Lake Desert contains two watersheds, the Newfoundland Basin watershed to the north and BSF watershed to the south (Fig. 1A). The Bonneville Salt Flats is the only naturally occurring saline pan with a persistent halite crust within the Great Salt Lake Desert (Nolan, 1927; Wold & Waddell, 1994; Radwin & Bowen, 2021). BSF is bounded by the Silver Island Mountains' alluvial fan to the west/north-west, lacustrine mudflat to the east, and a potash mine and major interstate highway to the south. A north-east/south-west trending graben bounds BSF (Fig. 1B; Smith *et al.,* 2012).

Anthropogenic activities impact sediments by compacting them, removing solutes and altering BSF's hydrology. Since 1906, railways dissected and isolated BSF from most of its watershed to the south (Fig. 1A; Kipnis & Bowen, 2018). The hydraulic gradient from adjoining areas used to flow towards BSF. From 1960 to 2016, groundwater levels decreased near water extraction sites, reversing subsurface flow from a recharge source to a discharge source (Lines, 1979; Mason & Kipp, 1998; Kipnis & Bowen, 2018). Brines have been harvested from BSF for salt production since 1907. Mined solutes account for an estimated third of the observed decrease in saline pan volume since 1960 (Kipnis & Bowen, 2018). Racing events started in 1914 and now bring tens of thousands of visitors to BSF annually (Noeth, 2002; Bowen *et al.,* 2018a). Most summers, the crust is compacted to prepare extensive racetracks. The Salduro Loop berm isolates a portion of BSF from racing and limits

COLOR

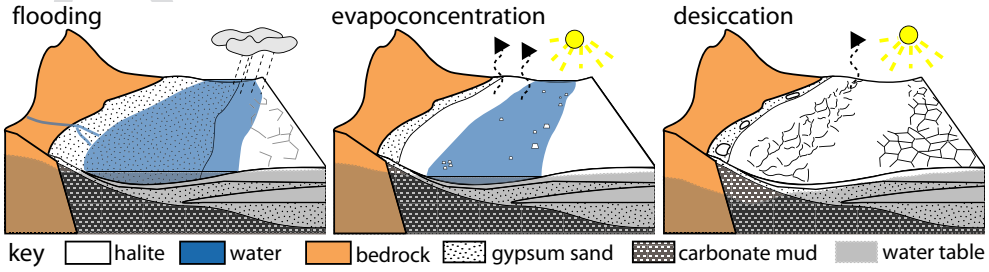

Fig. 2. Generalized schematic of flooding-evapoconcentration-desiccation hydrological stages at the Bonneville Salt Flats. Modified from Lowenstein & Hardie (1985). Wind also impacts the location of surface waters.

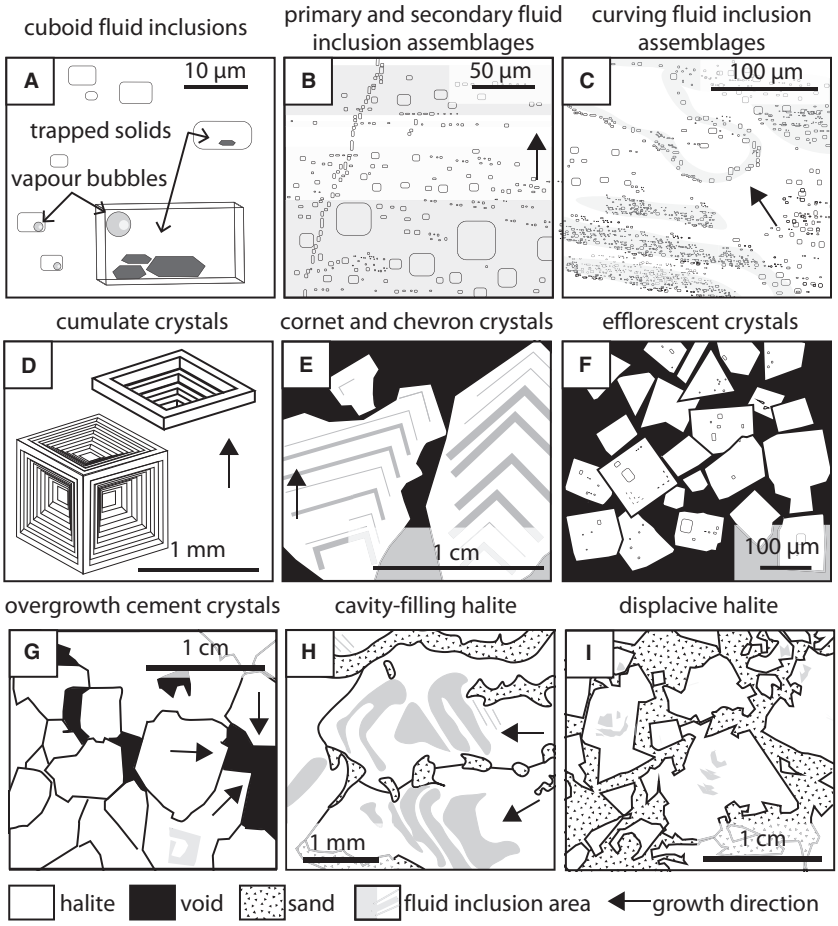

Fig. 3. Fluid inclusions, fluid inclusion assemblages and common primary and diagenetic halite crystal morphologies. Schematics have different scales and are oriented with stratigraphic up at the top of the page. Arrows demarcate growth direction. (A) Single-phase and multi-phase primary cuboid-shaped fluid inclusions in halite with all-liquid, liquid–vapour and liquid–vapour-solids compositions. (B) Primary and secondary fluid inclusion assemblages. (C) Primary curving fluid inclusion assemblages developed over a partially dissolved surface (after Roedder, 1984). (D) Millimetre-scale cumulate crystals. (E) Millimetre to centimetre-scale chevron and cornet crystals. (F) Small, 50 to 200 µm wide, efflorescent crystals with faint fluid inclusion assemblages. (G) Clear euhedral halite cement overgrowths terminating into voids. The crystals' faint fluid inclusion-rich centres may be chevron remnants (after Casas & Lowenstein, 1989). (H) Cavity-filling halite with growth towards cavity centre. Rounding of crystals from dissolution and overgrowth (after Li *et al.,* 1996). (I) Displacive halite crystals with random crystal orientation, faint fluid inclusion assemblages and incorporation of sediment into crystals (after Casas & Lowenstein, 1989).

surface and subsurface fluid flow (Fig. 1B). Mining companies added *ca* six million net tonnes of NaCl as halite-undersaturated brine to BSF from 1997 through to 2020 (White, 2002; Kipnis & Bowen, 2018; Kipnis *et al.,* 2020).

Several natural processes impact BSF's sediments. Meteoric precipitation and evaporation at BSF influence groundwater level fluctuations and flooding-evapoconcentration–desiccation stages (Bowen *et al.,* 2017). Maximum evaporation is estimated at 1.3 to 3.0 mm day^{-1}, when the surface is flooded, to 0.08 to 0.5 mm day^{-1}, when the surface is desiccated (Turk, 1973; Lines, 1979; Mason & Kipp, 1998). Wind influences surface fluid movement, and sediment accumulation, ablation and reworking (Bowen *et al.,* 2017; Kipnis & Bowen, 2018). The surface extent of ponded waters and halite were documented at BSF from 1986 to 2015 (Bowen *et al.,* 2017). Surface ponding is concentrated at the western margin of BSF, but wind-blown waters can extend rapidly across the entire saline pan

(Bowen *et al.,* 2017; Craft & Horel, 2019). Aeolian gypsum and oolitic carbonate sand are concentrated in sediments at the saline pan's edge (Jones, 1953; Eardley, 1962; Bowen *et al.,* 2018a).

Bonneville Salt Flats evaporites

Stakeholder concerns over the extent and thickness of saline pan sediments motivated measurements of saline pan sediment thicknesses five times from 1960 to 2016 (Christiansen *et al.,* 1962; McMillan, 1974; Brooks, 1991; White & Terrazas, 2006; Bowen *et al.,* 2018b; Kipnis & Bowen, 2018). The volume of BSF saline pan deposits decreased by 28% from 1960 to 2016 (*ca* 56 million tonnes; Bowen *et al.,* 2018b). The saline crust's surface extent generally decreased from 1986 to 2015 (ranging from 156 km^2 to 72 km^2; Bowen *et al.,* 2017).

The Bonneville Salt Flats' stratigraphic architecture and evaporite bed thickness were measured in September 2016 with 69 shallow cores (30 to 220 cm deep; Bowen *et al.,* 2018b; Kipnis & Bowen, 2018). Halite beds are thickest at the centre and taper to the edge of the lens-shaped evaporite package (Fig. 1C). Two-thirds of saline pan deposits at BSF consist of gypsum sand (Bowen *et al.,* 2018b). The thickest surface halite deposits occur in the area surrounded by and to the north-east of the Salduro Loop berm (Fig. 1 B; Appendix A). The saline pan overlies laminated aragonitic lacustrine deposits and gypsum with carbonate mud (Fig. 1C; Bowen *et al.,* 2018b). In the lacustrine sediments, the aquifer is highly-permeable, halite undersaturated, and decreases in salinity away from the saline pan's centre (Turk, 1973; Lines, 1979). An environmental DNA-based microbial census of BSF sediments found a high biomass microbial community concentrated in shallow (<30 cm) halite and gypsum layers (McGonigle *et al.,* 2019).

Saline pan evaporite sediments

Evaporite morphologies related to each saline pan stage are reviewed here (Lowenstein & Hardie, 1985; Casas & Lowenstein, 1989; Li *et al.,* 1996). The results of this work build upon these descriptions of syndepositional morphologies. Assemblages of genetically related fluid inclusions aid interpretation of evaporites. Primary fluid inclusion assemblages form concurrently with crystal growth and record rapid growth as cloudy, inclusion-rich layers, and slow growth as transparent, inclusion-poor layers (Roedder, 1984a; Benison & Goldstein, 1999). Growth banding defined by primary fluid inclusion assemblages is parallel to crystal faces or, when it develops over partially dissolved surfaces, curving (Fig. 3B and C; Roedder, 1984a; Goldstein *et al.,* 1994). Secondary fluid inclusion assemblages form after crystal growth, along healed fractures and deformation surfaces (Fig. 3B).

Crystals are altered by dissolution concentrated at the surface and vadose zone during the flooding stage. Horizontal dissolution surfaces form at the saline-pan surface, truncate bottom-growth crystals, and are overlain by detrital sediment or halite overgrowths. Dissolution of surface evaporite layers concentrates authigenic and detrital gypsum, creating gypsum layers. Evaporite structures and water table level influence pore morphology. Vugs develop at the water table, beneath shelter voids, and at layer boundaries (Lowenstein & Hardie, 1985). Vertical dissolution pipes form between bottom-growth crystals in the vadose zone and are limited in height and quantity by the groundwater depth, bedding thickness and degree of dissolution (Shearman, 1970; Lowenstein & Hardie, 1985; Li *et al.,* 1996; Schubel & Lowenstein, 1997; Holt & Powers, 2011; Taj & Aref, 2015). Sand or mud can line or fill pores. Cement crystals are rounded by phreatic zone dissolution (Casas & Lowenstein, 1989; Li *et al.,* 1996).

Cumulate, chevron and cornet halite crystals form during the evapoconcentration stage. The morphology of halite crystallized from ponded water is controlled by water depth and evaporation rate (Southgate, 1982; Lowenstein & Hardie, 1985). Sub-millimetre to millimetre-scale platy, hollow pyramid and cubic cumulate crystals form within the water-column as individual crystals or at the air–water interface as crystal aggregates. During periods of rapid evaporite growth randomly oriented cumulate crystals are preferentially deposited (Fig. 3D; Dellwig, 1955; Shearman, 1970; Arthurton, 1973; Lowenstein & Hardie, 1985). Chevrons and cornets are millimetre to centimetre-scale vertically oriented competitive crystals with dense primary fluid inclusion banding (Fig. 3E; Shearman, 1970; Arthurton, 1973). Upward-pointing chevrons and flat-topped cornets form in shallow waters at the sediment–water interface.

During the desiccation stage the crust buckles and deforms, efflorescent crystals develop on

the surface, and diagenetic halite cement crystals form in the subsurface. Efflorescent crusts develop from evaporating groundwater or reworked halite dust and consist of micron-scale crystals (20 to 100 μm) with faint primary fluid inclusions (Fig. 3F; Hunt, 1966; Smoot & Castens-Seidell, 1994; Taj & Aref, 2015). Preserved efflorescent crusts, although rare, are microcrystalline or consist of interlocking millimetre-scale crystals (Benison & Goldstein, 2001; Bobst *et al.,* 2001). Experimental studies indicate that pore-filling halite cement develops in near-surface sediments in the vadose and phreatic zone concurrently with efflorescent growth, with smaller pores filling before larger pores (Nachshon *et al.,* 2011; Eloukabi *et al.,* 2013).

Most halite cements develop beneath the water table. Halite cement can crystallize because of brine temperature changes, evaporative concentration or brine mixing (Hsu & Siegenthaler, 1969; Raup, 1970; Valyashko, 1972; Gornitz & Schreiber, 1981). Pore-filling euhedral halite cement overgrowths are generally clear with few fluid inclusion assemblages (Fig. 3G; Hardie *et al.,* 1985; Casas & Lowenstein, 1989). Primary crystals are replaced under repeated cycles of dissolution and overgrowth crystallization. In contrast to vertically oriented chevron crystals, cavity-filling halite crystals have faint primary fluid inclusion assemblages and growth directed towards a cavity centre (Fig. 3H; Li *et al.,* 1996). Clear randomly oriented displacive halite crystals with fluid-inclusion-rich patches develop in fine-grained matrices, disturbing bedding and incorporating host sediment as solid inclusions (Fig. 3I; Gornitz & Schreiber, 1981; Casas & Lowenstein, 1989; Benison & Goldstein, 2001).

METHODS AND MATERIALS

Environmental, field and laboratory measurements and observations were used to describe evaporite morphologies and environmental processes. Saline pan surface observations were made with time-lapse-cameras (Brinno TLC200, Taipei, Taiwan; Axis Communications web camera, Lund, Sweden) and regular site visits (Appendix A). Weather station measurements of surface and shallow subsurface temperatures, incoming and outgoing radiation, and meteoric precipitation were used to constrain environmental conditions and saline pan stages (Fig. 1 B; Appendix B). Using the methods of Craft & Horel (2019), the crust's albedo was used to measure surface moisture changes (Appendix B).

Pressure-temperature data loggers were placed in shallow wells to record changes in water level and temperature (Fig. 1B; U20L-04 and U20L-01, Onset, Bourne, Massachusetts, USA; Appendix C). One well (BLM-93C) was screened within the saline pan. All other wells were screened within the underlying lacustrine-sediment-hosted aquifer. The hydraulic head for co-located wells BLM-93C and BLM-93 was corrected for density and used to measure local vertical hydraulic gradients (Post *et al.,* 2007; Appendix C). Brine density and temperature were measured in the field (Densito 30PX, Mettler Toledo, Columbus, Ohio, USA). Brine quasi-salinity and degree of halite saturation were calculated with an adaptation of Sirota *et al., &*'s (2016) methods (Appendix D). Quasi-salinity (σ_{30}) is computed from brine density at 30°C (kg m^{-3}; Anati, 1999). The degree of halite saturation (in quasi-salinity units) was calculated by subtracting the density of a brine sample at field conditions from the density of that sample equilibrated with halite at the same temperature. The effect of temperature on the degree of halite saturation was also measured (Appendix D). Four dust traps modelled after Reheis & Kihl (1995) collected sediment for 1.2 to 2.5 years (Fig. 1B; Appendix E). Sediments collected with dust traps were analysed with an optical microscope and weighed.

Surface and subsurface evaporite slab samples were collected during the desiccation stage in 2016 and 2017 (Appendix F; Bowen *et al.,* 2018b). Prior years, 2014 and 2015, were very wet (Bowen *et al.,* 2018b). Forty-six large-format thick section slabs (0.1 to 3.0 mm thick) and one small format thin section were prepared from ten sites. Nine surface sites were sampled to cover a range of surface conditions across BSF (Fig. 1B). Sites varied in crust thickness, flooding frequency, water table depth, and surface use. Three subsurface samples (30 to 80 cm depth), two with corresponding surface samples, were collected. Subsurface samples were limited by sample quality and the spatial extent of halite below 30 cm depth.

Surface crust blocks were collected using a reciprocating saw and crowbar. Subsurface samples were collected with a continuous track-mounted vibracore and free-standing vibracore (Fig. 6A). Samples were wrapped with a polyethylene wrap to maintain their structural integrity and desiccated for several months at room

temperature. Samples were cut with a dry rotary saw and examined. Thick section slabs impregnated with pink (rhodamine B), blue (blue supra; to accentuate pores) or clear epoxy, doubly polished, and mounted on glass slides using minimal water or heat (mineral oil fluid, Wagner Petrographic, Utah, USA; Appendix F). Cleaved halite chips were examined to confirm that features did not originate from sample preparation.

Crystal morphology in thick section slabs were examined with photomosaic images made with a Zeiss Axio Imager.M2m microscope (Carl Zeiss AG, Oberkochen, Germany) with 25× magnification, reflected, plane-transmitted, and cross-polarized illumination. Small, millimetre to micron-scale features, such as fluid inclusion assemblages, were characterized with an Olympus BX53M microscope equipped with an ultraviolet-visible (UV-vis) light source (Olympus U-RFL-T, Tokyo, Japan; 20 to 1000× magnification) with plane transmitted, cross-polarized and UV-vis light using a Leica camera (MC 120 HD, Buffalo Grove, Illinois, USA). Relative elemental concentrations of layers were previously confirmed using portable X-ray fluorescence spectroscopy (Bowen *et al.,* 2018b). Halite and gypsum were differentiated with optical extinction, cleavage planes and crystal habit. Sand grain composition, size and shape from thick section slabs and cores were analysed to constrain the structure and origin of gypsum sand beds (Appendix G).

Eight bedded halite samples were measured with X-ray computed tomography (CT; Zeiss Volumax and Zeiss Xradia High-Resolution Micro CT; Appendix H). The program FIJI was used to characterize sample morphology and porosity (Schindelin *et al.,* 2012).

RESULTS

Environmental measurements

Environmental measurements were used to provide a context for sedimentological interpretations by constraining the types, size, timescales and spatial heterogeneity of syndepositional processes at BSF (Appendices B to E).

Surface moisture

Precipitation and albedo provide measures of surface moisture (Appendix C, Fig. 4A; Craft & Horel, 2019). Autumn 2019 precipitation raised water levels, but the surface pond partially desiccated in November, raising albedo. The surface remained wet in the winter with increased rainfall and low evaporation. In late winter/spring, as evapoconcentration and surface desiccation advanced, newly deposited halite was exposed, increasing surface albedo. Albedo plateaued during the desiccation stage, only increasing slightly after new efflorescent crystals formed after rain in October 2020.

Water level, temperature, quasi-salinity and degree of halite saturation

Groundwater measurements document seasonal and daily cycles in temperature, water level and quasi-salinity (Figs 4 and 5). The groundwater measurements discussed here span from the relatively dry period of September 2019 to December 2020. July 2020 was selected to show daily fluctuations in groundwater levels and temperatures because it has the highest potential evapotranspiration (Bowen *et al.,* 2017).

Temperatures vary across groundwater, air, and the shallow crust (Figs 4B and 5A). The average temperature of the shallow crust (10 cm) was slightly warmer and less variable than the air. In the summer, the difference in groundwater temperature between the surface and 2 m depth was up to 10°C. In the winter this difference decreased to <3°C (Fig. 4B). Diurnal groundwater temperature fluctuations decreased with depth (<1°C below 50 cm depth; Fig. 5A).

Groundwater levels changed spatially and temporally (Figs 4C and 5B; Appendix C). Surface flooding maintained high water levels in the central part of the saline pan (BLM-93, BLM-93C and BLM-37) more than the eastern edge (BLM-34; Fig. 4C). From June to August 2020, water levels remained within 10 cm of the surface near BSF's centre, and fell sharply near the brine removal ditch at BSF's eastern edge (BLM-34) where the effect of brine removal was marked. After pumping ceased BLM-34's groundwater levels rapidly increased by *ca* 10 cm (Appendix C). Water levels near the centre of BSF dropped much more (30 cm) from September to November 2020 than they did in the preceding desiccation period; groundwater temperatures also decreased. There was a seasonal difference in the density-corrected hydraulic head between BLM-93C, screened in saline pan sediments, and the co-located BLM-93, screened in the underlying lacustrine sediments (Figs 4C and F). In the winter, regardless of surface moisture, there was a downward hydraulic gradient. In the summer, the hydraulic gradient and flow were upward.

COLOR

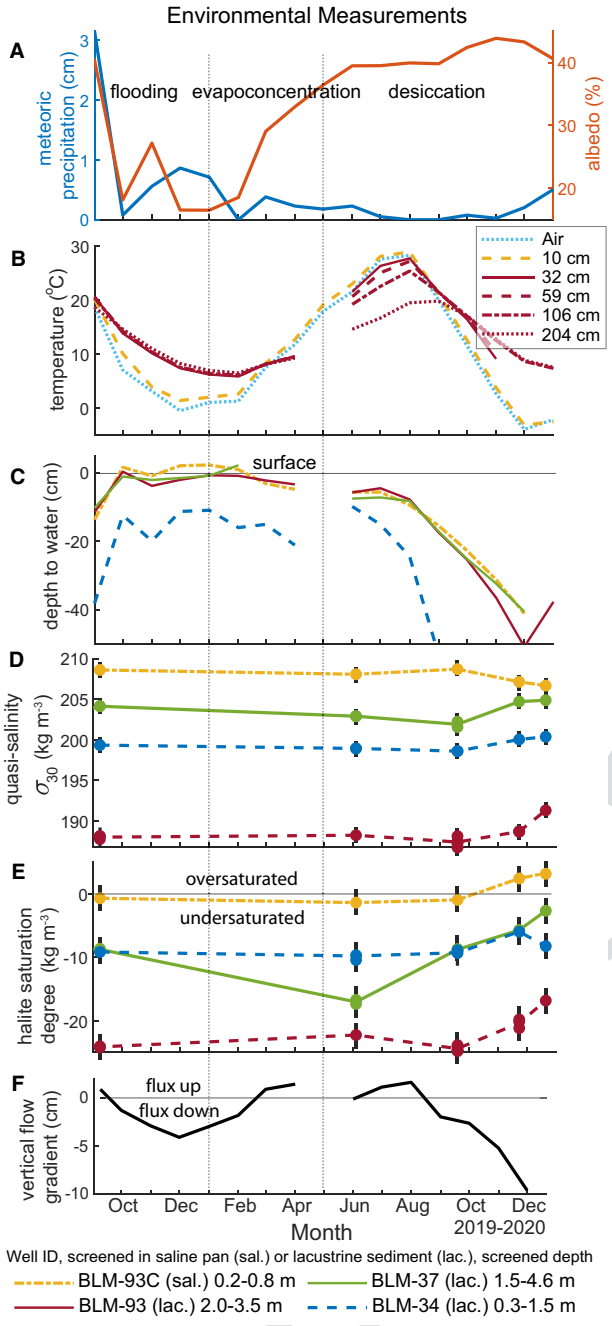

Fig. 4. Environmental measurements of temperature, water level and quasi-salinity from September 2019 to December 2020 (Appendices B, C and D). Months denoted at base. Measurements made with weather station (A) and (B), pressure-temperature loggers (B), (C) and (F), and brine samples (D) and (E). Data gaps originate from limited site access and data logger storage capacity. (A) Measures of water availability at the surface: total monthly meteoric precipitation and monthly average albedo. High albedo is indicative of low surface moisture and new halite growth. Different saline pan stages demarcated with dashed lines. (B) Average monthly temperature of air, crust (10 cm depth) and BLM-93's groundwater (32 to 204 cm depth). Key for (C) to (E) at figure base. (C) Average monthly water level fluctuations across four wells (see Fig. 1B). The water level of BLM-93 (co-located with the shallower BLM-93C) is adjusted to equivalent head at a reference density of 1.2 g cm-3 to make hydraulic head measurements comparable between BLM-93 and BLM-93C (Appendix C). (D) Quasi-salinity at 30°C of brine samples from wells. Lines added to (D) and (E) to highlight trends. (E) Degree of halite saturation in quasi-salinity units. Measurement error of ±1 kg m^{-3} for (D) and ±2 kg m^{-3} for (E) (quasi-salinity) shown as vertical black lines behind markers. (F) The difference in density-corrected hydraulic head between BLM-93 and BLM-93C shows a downward hydraulic flow gradient in the autumn to winter and an upward hydraulic gradient in the spring to summer.

In July, the water level in BLM-93C, the well screened in saline pan sediments, varied daily by 6.1 cm on average (Fig. 5B). This significant change in water depth across the day at BLM-93C coincides with daily temperature changes of *ca* 6°C in the shallow crust. Peaks and troughs in crust temperature and water level coincided (Fig. 5).

Brine sample salinity and degree of halite saturation varied with well depth, location and time (Figs 4D and F; Appendices C and D). Changes within brine composition in lacustrine-sediment-screened wells can inform interpretation of halite alteration and brine movement between the saline pan and underlying aquifer. Brines from BLM-93C, in contact with evaporite sediments, had the highest quasi-salinities and were consistently at or near halite saturation (within measurement error of ±2 kg m^{-3}). Experiments indicate that the degree of halite saturation change would be <1.5 kg m^{-3} (quasi-salinity) for a 10°C temperature change (Appendix D). The quasi-salinity of wells screened in underlying lacustrine sediments changed by less than 3 kg m^{-3} throughout the year (Fig. 4D). In brines from the lacustrine-sediment aquifer, the degree of halite saturation generally increased throughout the unusually long 2020 desiccation stage (Fig. 4E).

Dust traps

Dust traps accumulated non-soluble material at a depositional rate of *ca* 150 mg m^{-2} day^{-1} or 3.3 mm/100 years (Appendix E). Dust traps

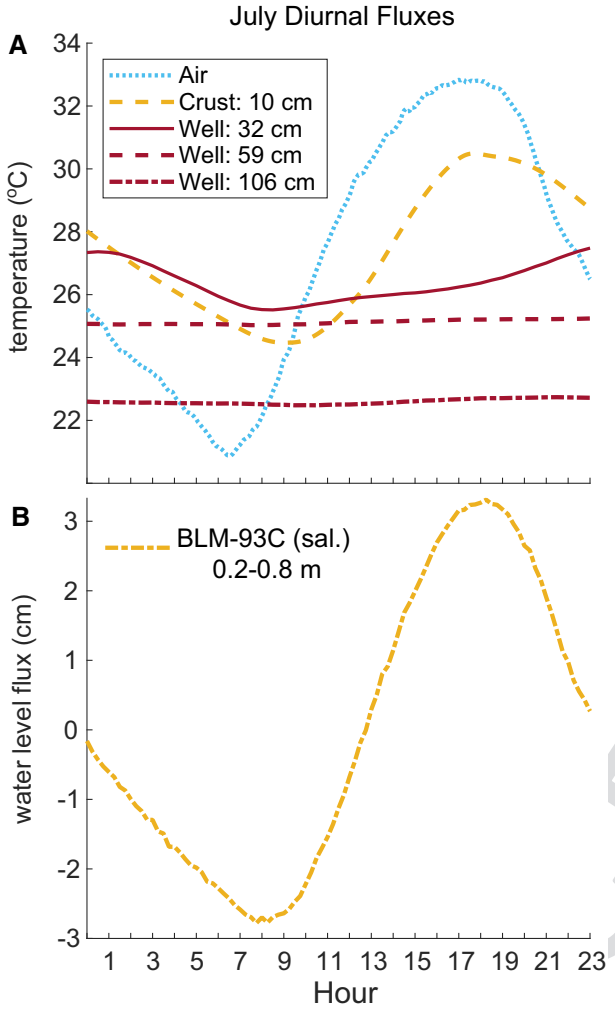

Fig. 5. Average diurnal fluxes in temperature and water level in July 2020. (A) Average daily air, shallow crust and groundwater (well BLM-93) temperature fluctuations. (B) Average daily groundwater level fluctuations in BLM-93C, which is screened within saline pan sediments. The daily high-water level in BLM-93C coincides with the daily peak in crust temperature (10 cm depth). The daily change in water depth in other wells is not discussed because they are not screened within saline pan sediments.

collected very-fine sand to silt-sized carbonate clumps (60%, abraded to rounded aragonite crystals, rod-shaped faecal pellets), gypsum grains (20%, abraded crystals), clay and mafic minerals (10%), and organic material (insects, 10%). Dust trap accumulation rates were highest on the western side of BSF and lowest on the eastern side. Silt-sized particles, especially carbonate material, were a minor portion (<1% volume) of saline pan sediments.

Surface observations

Field and time-lapse observations constrained the timescales and distribution of growth and alteration of surficial evaporites and sedimentary structures (Appendix A).

Flooding stage

Time-lapse cameras document dissolution, first of efflorescent crusts, followed by cumulate, chevron and cornet crystals (Appendix A). Dissolution created a smooth surface with rounded to flat crystals. During extended flooding periods, centimetre to metre-scale dissolution pits developed in areas with thinner surface halite (1 to 2 cm thick). Dissolution pits preferentially formed near efflorescent ridges and pressure buckles. The crust at the edge of the saline pan regularly dissolved. During the study period, the surficial saline crust at BSF's centre only partially dissolved. Dissolution was concentrated along polygonal fractures and pressure buckles. Dissolution was brief, on an hourly scale, or extended several days after a rain event, indicating a lag in brine reaching equilibrium with the halite crust. During winter, the surface pond fluctuated between dissolving halite and precipitating cumulate crystals.

Large circular (10 to 30 cm wide) raised (3 to 10 cm) distributed (several metres) blisters formed during surface ponding in thin halite crust areas (1 to 3 cm thick). A blister had smoothed partially dissolved crystals on top of it and cumulate crystals and insect bodies encircling it. Newly crystallized chevron and cumulate crystals were deposited in the area. The blister surface, near the race track, was planar during the desiccation stage in September; blisters appeared in December 2017, after a 15-day period of flooding and evapoconcentration. The partially dissolved crystals and the crystal growth encircling blisters indicate blisters formed during surface ponding, and falling water levels exposed blister tops before waters reached halite saturation.

Evapoconcentration stage

Cumulate rafts formed on the surface and were transported by wind. Rafts developed within days of a flooding event and at the end of the evapoconcentration stage. Rafts accumulated near raised features and the pond's edge.

Chevron and cornet crystals also could develop within days of surface flooding. Randomly distributed clumps of bottom-growth

crystals ranged in size (1 to 15 cm). Bottom-growth crystals >1 cm wide could crystallize within a few hours. Bottom-growth crystals preferentially developed on raised features such as the crust near polygonal fractures.

Desiccation stage

Pressure buckles and efflorescent crusts and ridges developed during the desiccation stage. Efflorescent growth rates were high in the first days of the desiccation period and then decreased. Efflorescent growths had several forms: popcorn halite, distributed patches and efflorescent ridges. Popcorn halite occurred as irregularly spaced finely-crystalline botryoidal nodules (2 to 30 mm wide). Popcorn halite could grow rapidly. Some efflorescent florets increased in size by *ca* 30% over 30 min (Appendix A). Very large (10 to 30 cm wide) popcorn nodules occurred on the edge of the saline pan. Distributed (30 to 100 cm spacing) efflorescent patches preferentially occurred above former dissolution pits. Patches could expand in diameter by >20 cm day^{-1}. Efflorescent ridges occurred along cracks associated with pressure buckles and polygonal fractures. Ridges increased in size throughout the desiccation stage. The tallest ridges developed over the largest polygonal fractures. Efflorescent ridge growth occurred primarily on either side of a fracture, but not in a narrow interval immediately above it. Wind-blown sediment preferentially accumulated along raised ridges.

The surface expression of halite crusts varied across BSF (Appendix A). The crust thickness and age correlate with its surface expression. Polygonal pressure buckles developed at the edges where the halite crust was thin and dissolved every year. Polygon diameter could vary year to year from 0.5 to >3.0 m. Near the centre of BSF the surface changed from relatively flat with small discontinuous buckles (<15 cm tall, near D-35) to large efflorescent ridge-filled polygonal fractures (1 to 3 m wide polygons; near D-60). Areas with relatively flat, one to three centimetre thick crust were flooded longer than sites with polygonally-fractured crust (Craft & Horel, 2019). The crust in areas with polygonally-fractured crust was thicker (*ca* 4 to 15 cm thick) and older (several flooding–evapoconcentration–desiccation cycles) than the crust in other areas.

A cross-section across a large polygonal fracture revealed that the crust was altered beneath and adjacent to fractures (Fig. 6B). The void beneath a fracture expanded with depth and was filled by detrital sediment and small randomly-oriented halite crystals (0.2 to 1.0 mm wide). The fractured layer of bedded halite was separated from the underlying continuous unfractured layer by a porous interval with gypsum. The bedded halite laterally adjacent to the fracture was altered by horizontal voids that connected to the fracture.

Suspect organic material coated near-surface bedded halite and gypsum layers (Fig. 6B; Appendix F). The material varied in colour throughout the year from pink, green, black and yellow during the desiccation period to tan and black during the flooding stage. In thick section, amorphous to spherule-shaped suspect organic material was clear to yellow in plane-polarized light. Like organic material in other systems, it fluoresced golden yellow to blue under UV-vis illumination (Mormile & Storrie-Lombardi, 2005; Conner & Benison, 2013).

Petrographic observations

Petrographic observations of primary bedded evaporites, dissolution features and diagenetic overprints were integrated to develop a syndepositional history of BSF evaporites. Local processes impact variations in sample morphology and layer thicknesses (Tables 1 and 2).

Primary bedded evaporites

Primary bedded evaporites are the subject of many evaporite palaeoenvironmental studies, and their fabrics influence the morphology of dissolution and diagenetic overprints. Primary halite crystals were partially identified by their well-defined parallel primary fluid inclusion assemblages (Fig. 9A). At BSF, the average primary fluid inclusion in primary halite was 2 to 5 μm wide and all-liquid. Some primary fluid inclusion assemblages in cumulate and chevron and cornet crystals had inclusions that averaged 10 μm wide. Cumulate crystals occurred as hollow cubes with indented faces (1 to 2 mm diameter, some >5 mm) with well to faintly defined primary all-liquid fluid inclusion assemblages. Loosely layered cumulate rafts created porous millimetre-scale planar voids (30 to 45% porosity; Fig 8B). Porosity in primary bedded evaporite layers was reduced beneath racetracks. Surface samples (<1 to 2 cm depth) near racetracks had an average off-track porosity of 34%, while on-track porosity was 19% (Appendix H).

COLOR

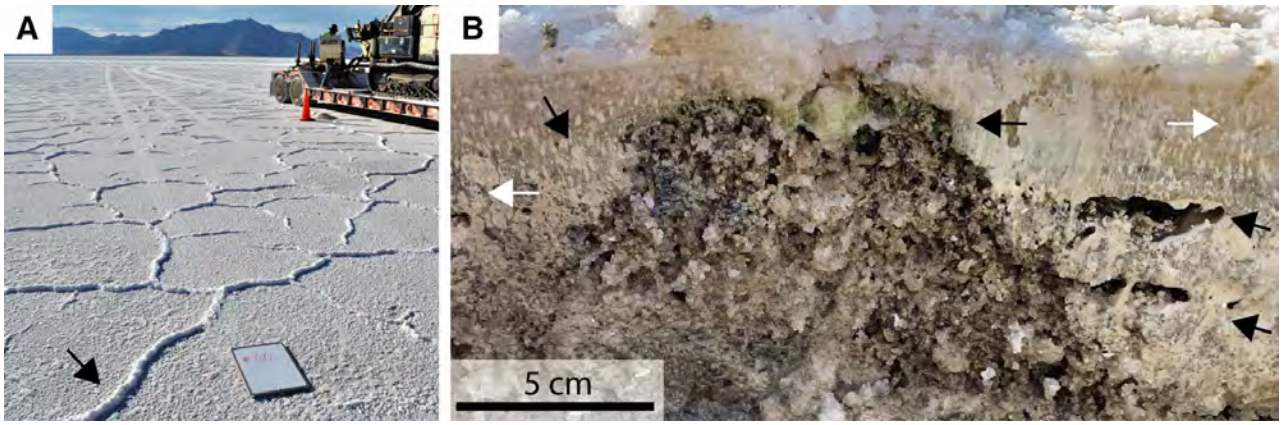

Fig. 6. (A) Polygonal fractures filled by efflorescent ridges (arrow) occur in areas with a thicker (*ca* <4 cm, Appendix A) surface halite layer. Vibracore drill rig in the upper right (7 September 2016 at D-60). (B) Cross-section of halite crust across a large polygonal fracture similar to (A). Note the horizontal vugs (arrows on right), downward-widening brown altered area (centre), vertical dissolution pipes (white arrows) and areas that are green and pink from microbial communities (left black arrow; 9 September 2020 at BLM-37).

Chevron and cornet crystals varied in size from 3 to 10 mm wide (average 5 mm, up to 15 mm). Approximately ten per cent of large primary fluid inclusions (>30 μm) were two-phase vapour–liquid inclusions; their vapour to liquid ratios were consistent within individual fluid inclusion assemblages. Five per cent of large primary fluid inclusions were two-phase liquid–-solid inclusions with accidental bladed birefringent crystals. The youngest, relatively unaltered layers of bottom-growth crystals had low porosity (10 to 15%) relative to other BSF halite layers (Fig. 8B and C). Bottom-growth crystal layers varied in thickness (Table 2; Fig. 7 A, B and D). Recent chevron and cornet layers were thinnest on the eastern side of BSF (2016) and thickest in the area inside the Salduro Loop berm (2016) and beneath the racetracks (2017).

Efflorescent crusts consisted of randomly oriented small (50 to 200 μm, some <25 μm) euhedral halite crystals with sparse primary fluid inclusion assemblages (Fig. 9B). Large (<20 μm) primary fluid inclusions in efflorescent halite were subcubic. Approximately one out of every four large inclusions were two-phase, either liquid–vapour or liquid–solid. Three-phase liquid–-solid–vapour inclusions were rare. Because these crystals form subaerially, vapour in fluid inclusions may be atmospheric. Efflorescent crusts had high primary intercrystalline porosity (45 to 50%; Fig. 8). Only halite crystals were optically differentiated in the efflorescent layer, the mineralogy of trace (<5% volume) silt to clay-sized amorphous and birefringent grains was not identified.

Gypsum sand layers varied in thickness (Table 2). Faint silty lamina were visible in some layers (Fig. 7A). Bottom-growth gypsum crystals that would indicate *in situ* growth were absent. However, rare gypsum splays occurred in voids. Gypsum grain size generally increased with depth from fine-grained to very fine-grained sand at the surface to coarse sand to very coarse sand at the base of saline pan sediments (Appendix G). Trace carbonate ooids occurred within gypsum sand beds. Upper gypsum beds were well-sorted and consisted of pitted and rounded to subangular grains. In contrast, lower gypsum beds were moderately sorted and consisted of angular grains.

Dissolution features

The morphology of halite dissolution features is influenced by the volume of dilute fluid input, its movement and groundwater levels. Dissolution was concentrated at the surface and at pre-existing intercrystalline voids and crystallographic weaknesses. Maximum void size generally increased with depth in the upper 30 cm of the crust; it then decreased as diagenetic halite filled pores. Small gypsum crystals (2 to 10 μm wide) and suspect organic material lined some dissolution surfaces (Fig. 11B).

Bedded halite layers in hand samples and thick-sections contained clear to tan horizontal dissolution surfaces that truncated underlying crystals (Fig. 7B and D). Horizontal dissolution

Table 1. Descriptions of sediment types identified at the Bonneville Salt Flats.

Sediment type	Textures	Description	Figure examples
Primary bedded evaporites	Efflorescent crusts	Efflorescent halite crystals	7A, 9B
	Cumulate halite	Cumulate halite crystals	7B
	Chevron and cornet halite	Chevron and cornet halite crystals with no to minor clear halite cement overgrowths, horizontal dissolution surfaces, tubular dissolution features	7A, 7B, 7D, 9A, 10
	Gypsum sand	Detrital and authigenic gypsum sand, minor detrital carbonates	7A
Altered bedded halite	Bedded halite with secondary porosity and halite cement	Chevron and cornet halite crystals with clear halite cement overgrowths, dissolution pipes, vugs and blocky tubule-dissected crystals	7B, 7D, 11
Remnant bedded halite	Halite cement crystals with secondary porosity and remnant chevrons	Subhedral to euhedral halite cement crystals with remnant chevrons and cornets, abundant curving fluid inclusion assemblages, rare cavity-filling crystals, minor dissolution pipes and vugs, gypsum in some intercrystalline voids	7C, 7F, 12, 13
Halite in gypsum	Random halite crystals in gypsum matrix	Gypsum sand (halite cemented or uncemented) with randomly oriented halite cement crystals	7E

Primary bedded evaporites form at the surface. Altered bedded evaporites contain primary bedded evaporites, secondary pores and halite cement. Remnant bedded halite primarily consists of halite cement crystals. The transition between sediment types is gradational.

Table 2. Surface sample (Fig. 1B) layer thicknesses.

	Layer thickness (mm)								
Sediment type and textures	D-12B	D-35	D-45	D-54	D-56	D-60	OffTr1	OnTr1	OffTr3
Efflorescent crusts	3	6.9	6.3	5.2	6.2	2.6	1.3	8.5	1.6
Cumulate halite	2	10.6	NA	1.2	7.6	2.5	4.4	NA	NA
Chevron and cornet halite	1		12.7	11.1		5	15	17	13.2
Gypsum sand	32.7	1.2	NA	NA	NA	NA	41.3	33.5	9.5
Altered bedded halite	NA	41.9	41	58.5	63	60	–	–	10
Gypsum sand	NA	NA	NA	37	4	1	–	–	11
Altered bedded halite	NA	NA	NA	NA	32.2	41.4	–	–	13.7
Remnant bedded halite	67.3	18.1	67	15	–	–	–	–	–
Halite in gypsum	20	–	–	–	–	–	–	–	–
Remnant bedded halite	30	–-	–	–	–	–	–	–	–

Sediment type and, where helpful, textures, are listed in order of occurrence from the surface to the sample base. If a layer was not present at a site, it is listed as NA. Cumulate and chevron crystals were intermixed at D-56 and D-35; as such, their collective thickness is listed.

surfaces were sharply (planar) to diffusely defined (eroded crystal edges; Figs 7B and 10B) and contained detrital material and micron-scale tubular dissolution features. Horizontal dissolution surfaces became increasingly poorly defined with depth.

COLOR

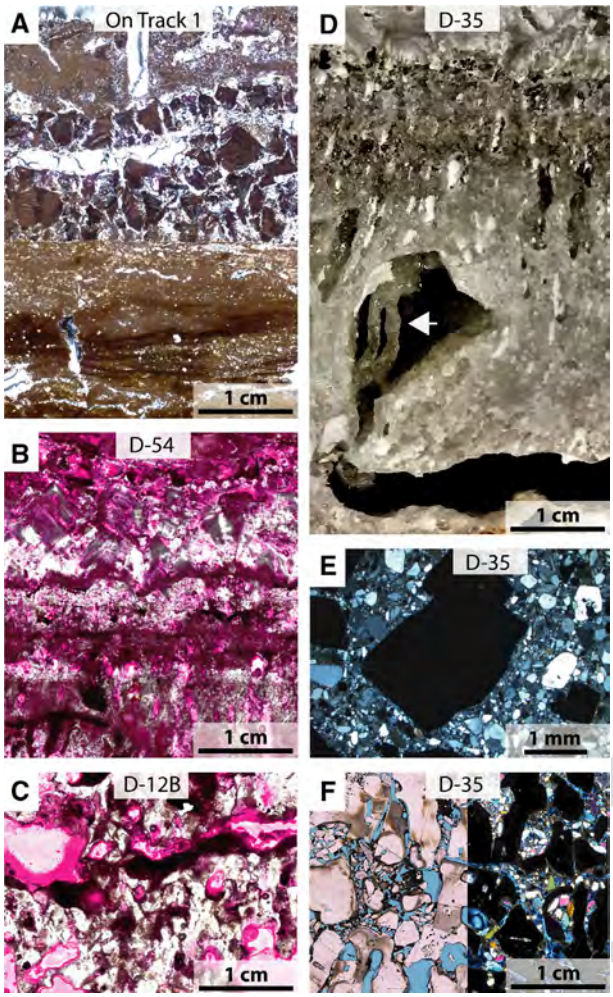

Fig. 7. Representative examples of depositional and diagenetic textures at BSF from thick section and slab samples. All panels are oriented with the top of the page as stratigraphic up and have the same scale – except for (E) which is magnified. Sample location name is shown at the top of each panel. The pink colour in (B) and (C) is from rhodamine B dye in epoxy. The top of (A), (B) and (D) is at the surface of the saline pan. (A) Primary bedded evaporates in thick section sample from On Track 1 (OnTr1) in cross-polarized light with clear epoxy. (B) Primary and slightly altered bedded evaporites in thick section from D-54 in plane polarized light. Crystal morphologies become increasingly poorly defined with depth. (C) Remnant bedded halite thick-section with gypsum-lined vugs and halite cement crystals in plane polarized light (from D-12B). (D) to (F) Samples from D-35 that are not stratigraphically contiguous. (D) Slab sample showing the transition from primary bedded halite to altered bedded halite. The large upper vug has pillars in it (white arrow). Dissolution pipes near the vug are sub-vertical and deviate away from the vug centre. (E) and (F) Thin sections of halite cement crystals and gypsum in from *ca* 40 to 63 cm depth. (E) Randomly oriented halite cement crystals (black) in gypsum matrix in cross-polarized light (*ca* 40 cm depth). (F) Halite cement crystals with secondary pores (blue epoxy), remnant bedding (horizontal gypsum layer) and intercrystalline gypsum (55 to 63 cm depth). Left side of (F) is in plane polarized light, right side is in cross-polarized light.

At BSF, vertical dissolution pipes truncated the edges of chevron crystals, rarely branched, and each pipe had relatively consistent widths (Figs 6B, 7D, 8A, 11A1, and B). Vertical dissolution pipes in uppermost layers were constrained to one bedded evaporite layer and were 0.5 to 4.0 mm wide and circular in cross-section. With increasing depth, dissolution pipes became wider and vertically extended across layers.

Vugs at BSF were millimetre to centimetre-scale and were identified by their nonuniform shape, which was equant to horizontally extensive, and variable in width and depth. Vertical dissolution pipes became sub-vertical and deviated away from the broadest part of larger vugs, indicating that vugs pre-date vertical dissolution pipes (Figs 7D and 8A). Some vugs contained internal pillars (Fig. 7D). Gypsum sand and halite cement crystals partially filled large centimetre-scale vugs in the northern part of BSF (Fig. 7C).

Microscopic tubules differed from dissolution pipes in scale and morphology. Tubules branched at sharp angles near crystallographic weaknesses, voids and fluid inclusions within crystals (Figs 10A and 11). Tubules at BSF ranged from 20 to 100 μm wide and were increasingly present with depth in shallow altered bedded halite layers. Many tubules contained suspect organic material and bladed gypsum crystals. Tubule concentrations increased at horizontal dissolution surfaces in both underlying and overlying crystals. With increasing depth, tubules dissected chevron and cornet crystals, creating a fragmented fabric of smaller crystals (100 to 500 μm wide; Fig. 11). Tubules did not occur in deeper layers of remnant bedded halite.

Diagenetic evaporites

Diagenetic halite formed from halite saturated groundwaters. Cement crystals occurred as euhedral to rounded overgrowths and void and cavity-filling crystals. Older crystals underwent multiple cycles of partial dissolution and overgrowth. Primary fluid inclusion assemblages in

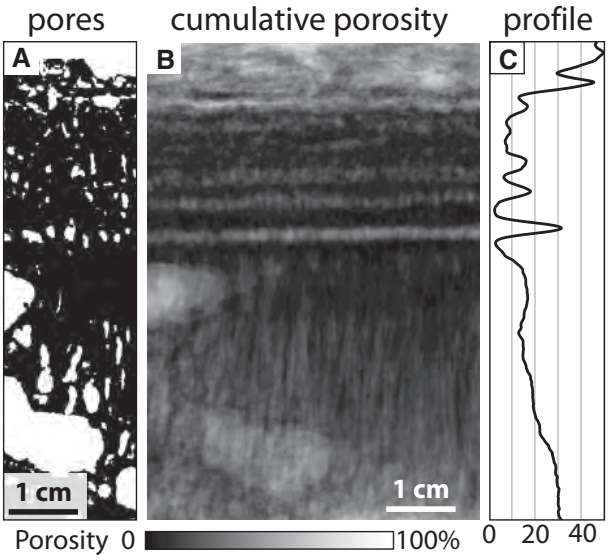

Fig. 8. X-ray computed tomography (CT) porosity data of crust from D-54. Stratigraphic up is at the top of the page. Saline pan-surface occurred at sample top. Porosity is shown as (A) a binary slice, (B) cumulative values averaged horizontally, (C) and as total porosity with depth. Black areas denote lower porosity, while light areas denote higher porosity. This sample's bulk porosity is 29% (±5%).

diagenetic halite were fainter and more curved than those of primary bedded halite; average fluid inclusion size was also smaller, ranging from 1 to 3 μm wide, indicating slower growth rates.

Small (0.2 to 1.0 mm) loose aggregated subhedral to euhedral void-filling halite cement crystals occurred in millimetre to centimetre-scale vugs connected to the surface, such as those adjacent to polygonal efflorescent ridges (Fig. 6). Detrital material coated void-filling crystals. The microscopic void-filling crystals with their faint, parallel primary fluid inclusion assemblages were larger than, but resembled, efflorescent halite crystals. Microscopic void-filling halite was not identified in bedded evaporite layers below 15 cm depth.

Halite cement overgrowths filled pores within and outside of pre-existing crystals. Overgrowth cement was generally clear. Some cement overgrowths contained faint distributed primary fluid inclusion assemblages with large (>200 μm) fluid inclusions.

Halite cement crystals typically contained multiple primary curving fluid inclusion assemblages. Curving primary fluid inclusion assemblages at BSF were subparallel three-dimensional thin layers (50 to 200 μm wide) of clear halite with faint, crystallographically aligned, predominantly single-phase all-liquid small cuboid fluid inclusions. Curving primary fluid inclusion assemblages occurred at the contact between partially dissolved crystals and halite cement overgrowths. Some vertical dissolution pipes were partially filled by halite cement overgrowths with multiple curving assemblages (Fig. 12B). Curving primary fluid inclusion assemblages along all sides of voids indicates growth in the phreatic zone. Younger, curving primary fluid inclusion assemblages truncated older assemblages, indicating multiple periods of dissolution and crystallization. Individual curving primary fluid inclusion assemblages may represent growth on surfaces eroded by dissolution or growth rate changes in cement crystals.

Large millimetre to centimetre-scale vugs contained subhedral crystals (1 to 5 mm wide) with

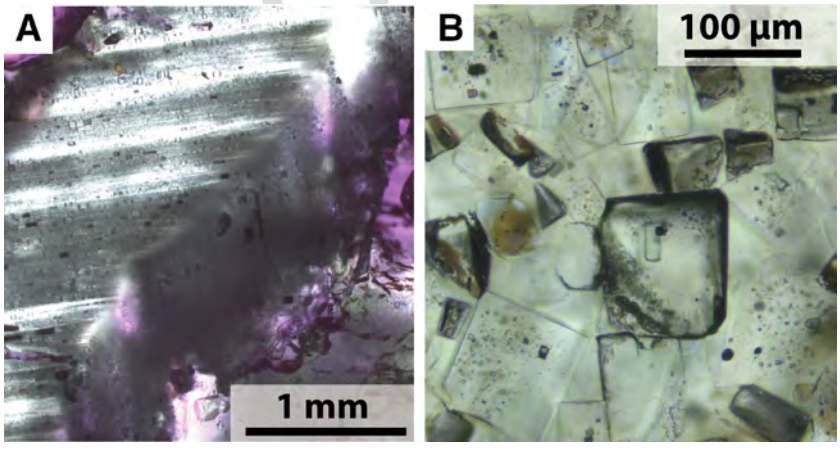

Fig. 9. (A) Cornet and (B) efflorescent crystals in plane polarized light and oriented with stratigraphic up at the top of the page. (A) Cornet crystal with well-defined fluid inclusion banding (from D-45). Pink epoxy (rhodamine B dye) used. (B) Efflorescent halite crystals with faint fluid inclusion assemblages (from OnTr1). Clear epoxy used.

COLOR

COLOR

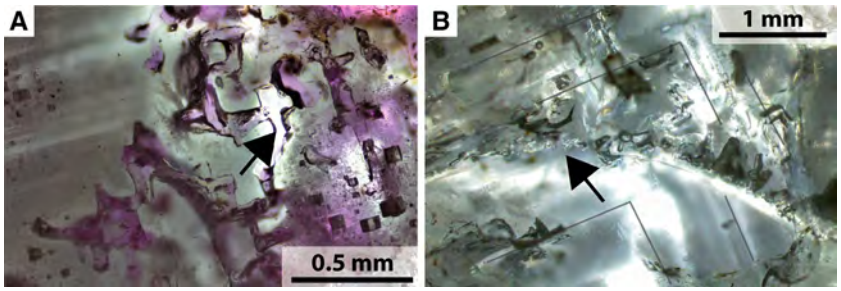

Fig. 10. Dissolution features in relatively unaltered bedded halite layers imaged with plane polarized light. (A) Branching tubular dissolution features (arrow) in cornet crystal (from D-35). (B) Minor truncation surface in chevron crystal (arrow; from D-45). Grey lines added to highlight growth banding of fluid inclusion assemblages. Oriented with stratigraphic up at page top. Images have different scales. Clear (B) and pink (A) (rhodamine B dye) epoxy used.

growth directed towards the cavity centre (Fig. 12A). Cavity-filling crystals had well-defined primary fluid inclusion assemblage banding with some large (>100 μm) fluid inclusions.

Randomly oriented small (0.5 to 3.0 mm wide on average) euhedral to subhedral halite crystals with faint curving primary fluid inclusion assemblages occurred in a gypsum sand matrix with minor carbonate grains. This texture occurred in gypsum-filled vugs and halite-cemented gypsum sand layers (Fig. 7E). Gypsum-filled vugs occurred in layers of remnant bedded halite (Fig. 7C). Halite-cemented gypsum sand layers did not show bedding. Gypsum grains were incorporated into some cement crystals as solid inclusions. This sediment type may originate from incomplete halite cement dissolution and mobilization of gypsum grains and halite cement crystals into vugs.

Halite crystals evolved through cycles of crystallization and partial dissolution. Deeper (>30 cm) halite beds (*ca* 15 cm thick) consisted of large crystals (0.5 to 1.5 cm) with millimetre-scale intercrystalline porosity partially filled by coarse gypsum crystals (Figs 7F and 13A1). The coarse gypsum crystals are much larger than those seen in upper intervals and may have grown *in situ*. These high porosity (*ca* 35 to 45%) remnant bedded halite layers contrast upper layers of segmented or cemented crystals (Figs 11A and 13A1). Segmented crystals were absent, indicating removal by dissolution or cement overgrowth. Halite cement crystals contained secondary vertical dissolution pipes. The number of secondary pores varied with stratigraphic interval. Despite the apparent random crystal orientation, the vertical fabric of chevron and cornet crystals and some horizontal dissolution surfaces were retained (Figs 7F and 13A). In contrast to thinner younger bedded halite layers, these layers had centimetre-scale spacing between horizontal dissolution surfaces (Table 2; Appendix F). Minor horizontal dissolution surfaces may have been removed by halite dissolution and crystallization.

Crystals with parallel to sub-parallel primary fluid inclusion banding indicative of chevron or cavity-filling halite cement crystals were common in deeper halite beds (Fig. 13A). These crystals had curving primary fluid inclusion assemblages indicative of partial dissolution and halite cement overgrowth (Fig. 13B). Rare halite crystals had cloudy fluid inclusion rich cores, solid gypsum inclusions and large (50 to 400 μm) two-phase (liquid-solid) primary fluid inclusions containing accidental gypsum crystals.

Vertical sediment trends

Primary bedded evaporite layers were increasingly altered by dissolution and diagenetic halite growth with depth (Table 1; Fig. 7). The distribution and thickness of depositional and diagenetic textures were spatially variable (Table 2). Layers with poorly-defined horizontal dissolution surfaces, tubule-dissected-crystals, and halite cement crystals developed from unaltered chevron and cornet halite layers. The final layer in this sequence consisted of remnant bedded evaporites with halite cement crystals. This was the only halite-dominant sediment type to remain below 30 cm depth. Similar trends occur in Death Valley saline pan sediments (Li *et al.,* 1996). Halite layers may be partially to fully

COLOR

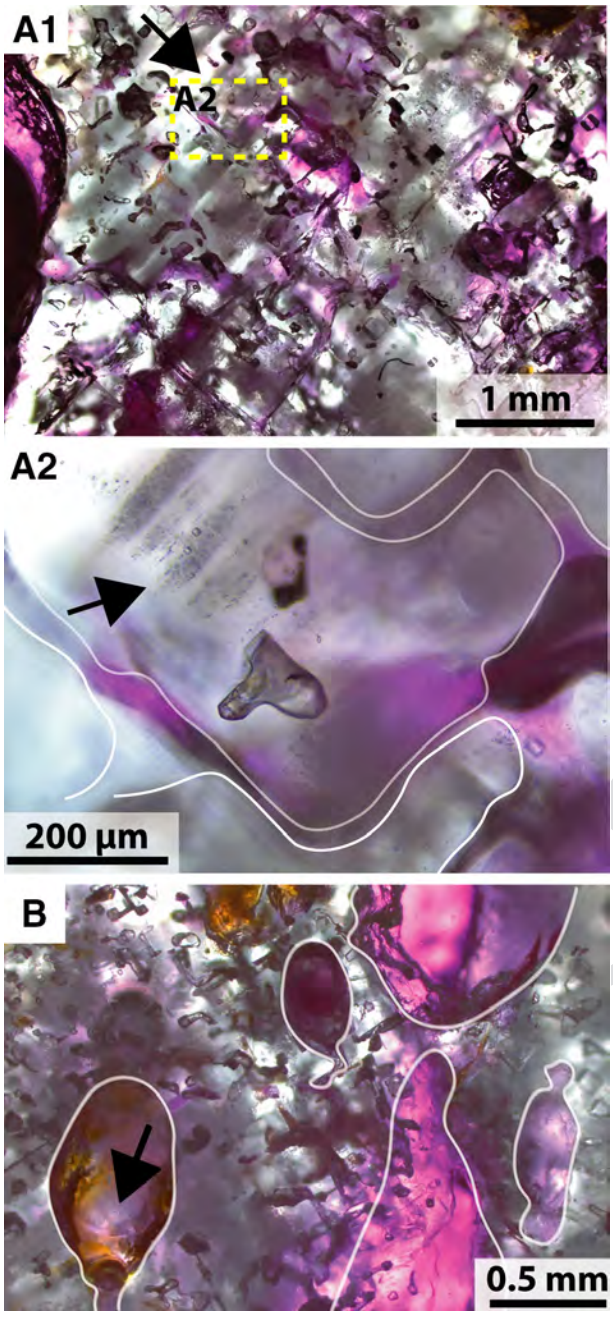

Fig. 11. Dissolution features imaged with plane polarized light and oriented with stratigraphic up at page top. Some voids are outlined in grey. (A1) Tubule segmented chevron crystals (from D-54). Inset image (A2) shows segmented chevron with remnant primary fluid inclusion assemblages (black arrow). (B) Dissolution pipes and tubules partially lined with amorphous yellow material (black arrow; from D-54). Pink (rhodamine B dye) epoxy used.

COLOR

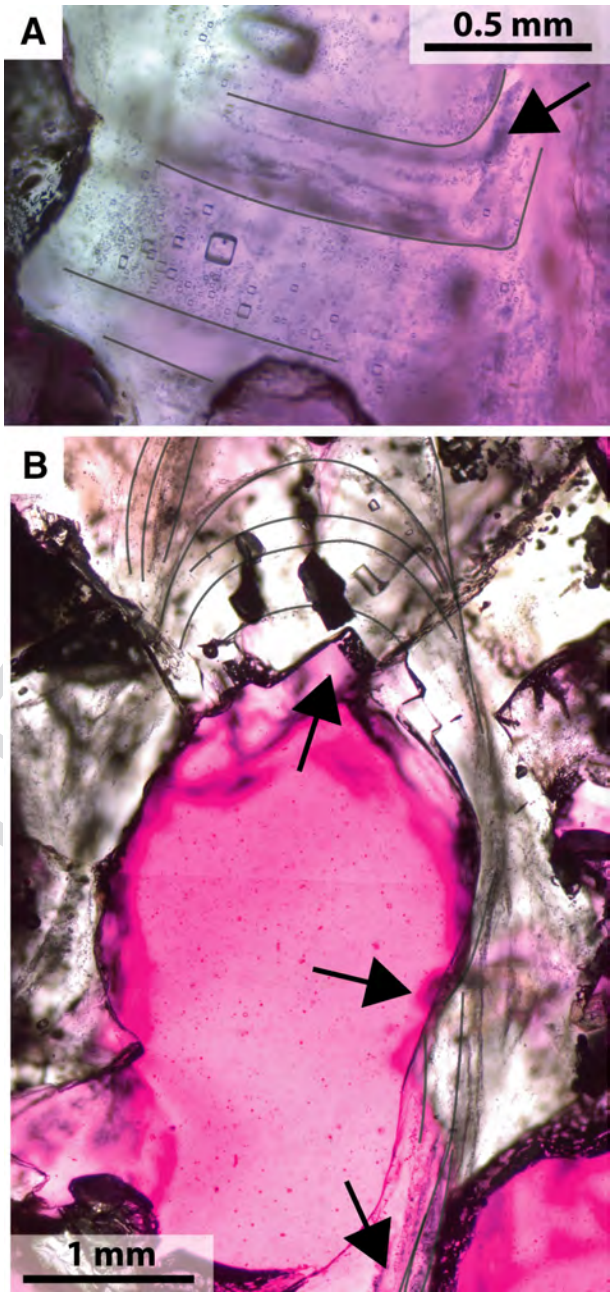

Fig. 12. Shallow (<30 cm depth) halite cements imaged in plane polarized light and oriented with stratigraphic up at page top (from D-12B). Grey lines added to highlight fluid inclusion assemblages. (A) Cavity-filling halite cement crystal. The slightly curving growth bands indicate downward growth from the crystal centre (the top of the image). (B) Halite cement overgrowth along a vertical dissolution pipe. Note curving fluid inclusion assemblages, euhedral overgrowth (upper arrow), truncated growth bands (middle arrow) and curving growth bands near the vertical dissolution pipe's base (lowest arrow). Pink (rhodamine B dye) epoxy used.

removed and filled by mobilized gypsum, creating gypsum beds or beds with remnant halite crystals in a gypsum matrix (Fig. 7E).

COLOR

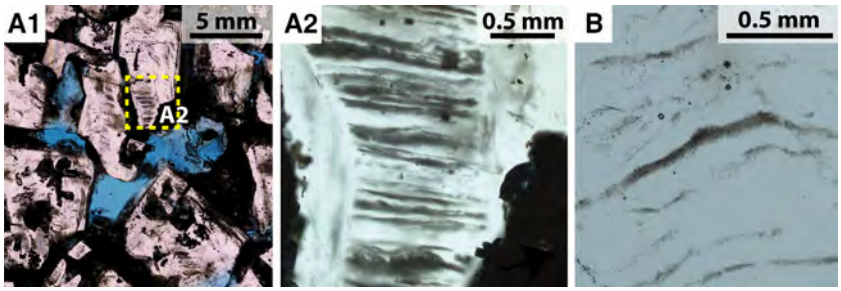

Fig. 13. Diagenetic halite crystals from 50 to 80 cm depth imaged with plane polarized light (from D-35). (A) Halite cement crystals. Inset image (A2) shows upward widening crystal with curving to parallel dense fluid inclusion assemblage banding. (B) Curving fluid inclusion assemblages in halite cement crystal. Blue supra epoxy used. Oriented with stratigraphic up at page top.

Upper halite layers (<15 cm) had an hourglass-shaped porosity (Fig. 8C). Porosity was highest at the top (efflorescent-crust) and bottom (altered bedded halite with vugs and dissolution pipes) of this interval. Porosity was lowest in layers of chevron and cornet crystals with pore-filling halite cement and incipient millimetre-scale vertical dissolution pipes. The high porosity in the upper halite layers at BSF is similar to other saline pans (Casas & Lowenstein, 1989). The porosity of deeper, remnant bedded halite layers (*ca* 35 to 45%) was higher than similar sediments in other modern saline pans (Casas & Lowenstein, 1989).

DISCUSSION

Seasonal and spatial changes in environmental and anthropogenic processes influence evaporite morphologies. There are clear differences between evaporite morphologies created and altered at the surface, vadose, and phreatic zones (Fig. 14).

Flooding stage

Small flooding events with minor dissolution last only hours to weeks at BSF, while the winter flooding stage, with potentially considerable dissolution, extends for several months. Evaporite dissolution is concentrated at the surface and along high-porosity areas in the vadose zone during flooding stages (Fig. 6B). The salinity and degree of halite saturation of brines from BLM-93C (screened within saline pan sediments) decreased after the winter flooding stage of 2020, indicating that potential phreatic zone dissolution occurred during the winter flooding stage (Fig. 4D and E).

Surficial dissolution is heterogeneous and is concentrated at pressure buckles and polygonal fractures. Surface flooding enhances detrital input by carrying sediments in suspension, contributing to silty lamina in gypsum layers and possibly enhancing dust-trap sediment accumulation rates on the western side of BSF. Dust deposition is a minor portion of sedimentation at BSF, indicating that most gypsum formed *in situ* and was then reworked. Distributed circular blisters indicate surface deformation can occur during surficial ponding. A low porosity, flexible crust beneath a racetrack could trap air, mobilized air bubbles could then accumulate underneath blisters, lifting the crust. Blisters may develop into dissolution pits. Distributed circular blisters described here differ from the irregularly-shaped, closely packed blisters of other systems (Goodall *et al.,* 2000).

The majority of secondary pores within bedded halite layers develop along intercrystalline pores within the vadose zone, which is controlled by the water table depth. Declining temperatures contribute to significant (*ca* 10 to 30 cm) water table decreases each autumn (Fig. 4C; Meyer, 1960; Turk, 1975). This increases the vadose zone size, making fall flooding stages have a greater impact than spring flooding stages upon evaporite alteration at depth. Vadose zone dissolution will be greater at the saline pan's edge, where the water table is lower.

Microscopic tubular dissolution features form at dissolution fronts. Tubules resemble irregularly shaped secondary fluid inclusions identified in Permian halite crystals (Benison &

COLOR

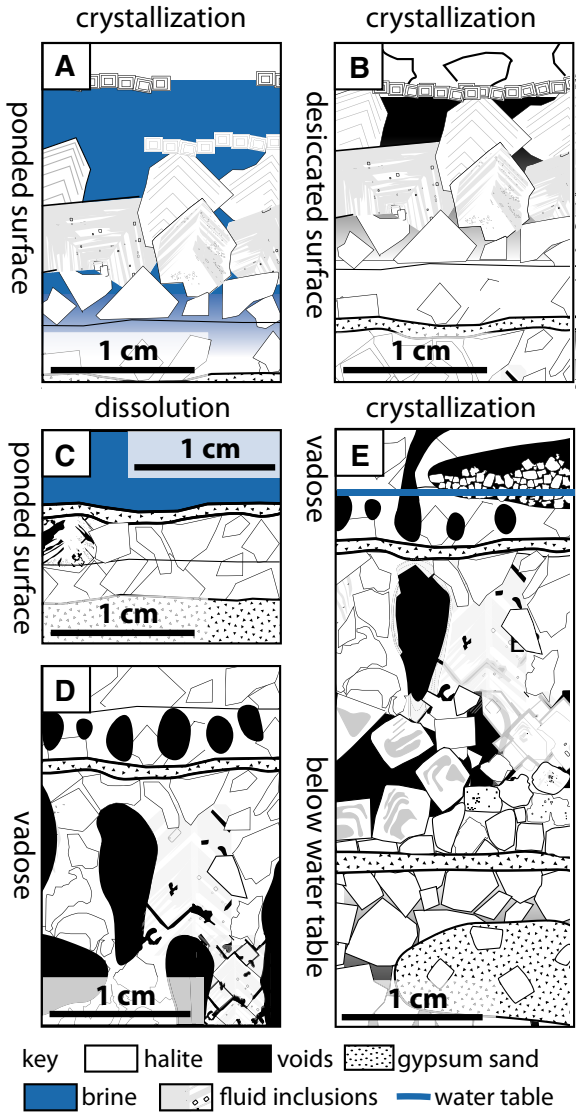

Fig. 14. Schematic of the evolution of evaporite morphology across a range of environmental conditions and depths, which are noted above and to the left of the figures. Stratigraphic up is page top. Conditions vary from crystallisation or dissolution above the ground, in the vadose zone, or below the water table. (A) Chevron, cornet and cumulate crystals form in halite saturated ponded brines. (B) Efflorescent crystals and clear halite cement form near and at the surface during desiccated conditions. (C) Horizontal dissolution surfaces and rounded and skeletal bottom growth crystals develop during haliteundersaturated ponding. (D) Altered bedded halite with dissolution features that develop within the vadose zone, including dissolution pipes, centimetre-scale vugs, segmented bottom growth crystals and dendritic tubules. (E) The transition from altered to remnant bedded halite. Diagenetic evaporites include interstitial cement, microscopic void-filling and cavity filling halite crystals, as well as halite cement crystals in gypsum sand and gypsum overgrowths.

Goldstein, 1999). Tubules dissect chevron crystals, creating a scaffold for halite cement overgrowths and halite cement crystals with remnant chevron crystal cores (e.g. Casas & Lowenstein, 1989).

Centimetre-scale horizontal vugs are concentrated near surface deformation features, such as polygonal fractures, which direct and concentrate dilute fluids and dissolution at the water table (Fig. 6). Horizontal vugs also influence flow paths; vertical dissolution pipes grow away from vugs (Fig 7D). Dissolution remobilizes sand and halite crystals into vugs (Fig. 7C), creating a sediment interval with halite cement crystals floating in gypsum sand (Fig. 7E). Mobilized crystals may become substrates for displacive halite growth. Remnant bedded halite layers may have formed in the phreatic zone during spring months when saline pan aquifer brine salinity decreased, and there was an upward flux of low salinity brines (Fig. 4D and F).

Evapoconcentration stage

Evapoconcentration stage crystal morphologies are well-described and are not focused upon here (Fig. 14A). Time-lapse imagery indicates that bottom-growth crystals can develop rapidly, within a few hours, possibly influencing the density of primary fluid inclusion assemblage banding. The consistent fluid-vapour ratio's in some fluid-inclusion assemblages suggest crystallization temperatures above 20°C (laboratory temperature), with vapour bubbles forming because of thermal contraction.

Desiccation stage

During the desiccation stage the saline pan surface deforms and efflorescent crusts and diagenetic halite develop. As also noted by Shearman (1970), efflorescent growth rates are highest immediately after the evapoconcentration stage. Efflorescent growth within the crust leads to expansion and buckling of the surface. Sub-centimetre thick crust tends to develop pressure buckles, while thicker crust (*ca* 5 cm) has polygonal fractures (Appendix A). Few surficial sedimentary structures develop at the western part of BSF, which has persistent seasonal flooding and a shorter desiccation stage (Craft & Horel, 2019). Similar to today, in 1975 and 1976 'rough polygonally-fractured' crust occurred near the saline pan centre, smooth crust occurred in areas of thinner halite and more flooding, and

pressure buckles formed near BSF edges (Lines, 1979). The spatial distribution and expression of surface deformation is important because deformation influences subsurface pore development (Fig. 6B).

There is no evidence for contractional features in the BSF crust. Dissolution, however, is clearly demonstrated and occurs preferentially along pre-existing voids, such as compressional pressure-buckles. Therefore, similar to modern intertidal polygons, the polygonal fractures were likely pre-dated by compressional buckles that were altered by dissolution (Appendix A; Christiansen, 1963; Lowenstein & Hardie, 1985; Lokier & Steuber, 2009). Buckles are conduits for dissolution, and if the dissolution of a buckled layer is incomplete, a crack remains as a preferential hydraulic conduit for efflorescence development (Eloukabi *et al.,* 2013; Shokri-Kuehni *et al.,* 2017). Multiple periods of crust deposition and dissolution along a fracture may have contributed to the downward-widening voids underlying polygonal fractures (Fig. 6B).

Sugary, microscopic void-filling halite crystals occurred in the vadose zone. These crystals only occur in voids with connections to the surface, such as polygonal fractures. Evaporation along efflorescent ridges may increase localized halite saturation. Sediments coating these crystals are transported from the surface during the flooding stage, when efflorescent ridge dissolution exposes fractures. Microscopic void-filling crystals are not preserved in deeper halite beds and may be misinterpreted as efflorescent crystals formed at the surface.

The temperature and groundwater depth at BSF and other saline pans vary throughout the day, causing periodic wetting and drying of the crust, and likely thermally-driven dissolution and crystallization of halite (Fig. 5; Turk, 1973; Macumber, 1991). Little removal of water from evaporation occurs from a desiccated crust, making it behave like a hydrologically closed system (Kampf *et al.,* 2005). Halite becomes slightly more soluble as temperatures increase. Diurnal temperature changes of 10°C in the shallow crust (<10 cm depth) could dissolve and crystallize a small volume (<1.5 kg m^{-3}, quasi-salinity) of halite each day (Appendix D). High water levels and high temperatures coincide, contributing to dissolution at the upper extent of the water level, and halite crystallization at the lower extent of the water level when brines are coolest (Fig. 5). The cumulative effect of these variations would enhance vertical flow-paths. Relatively stable summer water levels would concentrate this effect within a small depth interval (Fig. 4C). Olivella *et al.* (2011) previously demonstrated that temperature gradients have a significant effect upon porosity within saline media. Seasonal shallow-crust temperature changes of 10 to 30°C from 2 m depth to the surface would also contribute to evaporite alteration, as was suggested by Casas & Lowenstein (1989).

Curving primary fluid inclusion assemblages develop in the phreatic zone at the contact between dissolution and overgrowth (Fig. 12B). Multiple assemblages indicate several periods of partial dissolution and overgrowth. More generally, the small fluid-inclusion size in cement crystals is indicative of slower crystal growth rates.

Vertical gradients in temperature and water flow

Brine salinity and vertical hydraulic gradients change seasonally at BSF (Fig. 4D and F). Similar seasonal patterns in groundwater flux occur at the nearby Pilot Valley Playa (Duffy & Al-Hassan, 1988). In the winter, independent of saline pan stage, downward groundwater flow occurs, and is associated with increasing salinity in the lower, lacustrine-sediment-hosted aquifer. This flux indicates increasing potential for halite crystallization at depth (<50 cm) in winter months. Upward groundwater flow in the spring/summer is associated with increasing temperature and a salinity decrease in the lacustrine-sediment hosted aquifer (September 2020), representing growing potential for phreatic-zone halite dissolution. In other areas, without vertical flow gradients, thermal temperature decreases with depth could lead sinking dense brines to cool by 10°C, increasing the potential for evaporite deposition at depth. Further study is needed to fully constrain the effect of these small-scale hydrological processes (Mason & Kipp, 1998). Vertical flow gradients may also contribute to gypsum growth at the saline pan's base, where gypsum grains are larger and more angular. Prior studies found that vertical hydraulic gradients are spatially heterogenous at BSF (Lines, 1979). In contrast to other wells, at BLM-34 the saline pan is so thin that groundwater typically does not contact the evaporite-matrix, possibly contributing to the groundwaters' relatively stable quasi-salinity (Fig. 4D).

Heterogeneous surface processes and anthropogenic activities impact sediments

Heterogeneous spatial processes at BSF influence the distribution and morphology of saline sediments and sedimentary structures. Ponding is concentrated on the western side of BSF, which has higher detrital sediment accumulation rates and thinner and generally less deformed surficial halite layers. The thickest surficial halite layers accumulate at BSF's central high because it: floods less frequently; has lower detrital depositional rates; has the highest water table levels; the lacustrine-sediment aquifer underlying the saline pan is most saline here; and dilute surface waters are blocked by the Salduro loop berm or achieve halite saturation by the time they reach the central high, limiting dissolution to local meteoric precipitation.

Anthropogenic activities and infrastructure create different hydrological regimes within BSF, influence crust porosity and contribute to increasing the dissolution-prone vadose zone. Cumulate and bottom-growth crystal layers beneath racetracks have 15% less total porosity than undisturbed layers (from 34% to 19%). Distributed circular blisters form during shallow ponding at and near the racetrack. Thicker accumulations of efflorescent crusts at racetracks indicate racetrack preparation may enhance efflorescent growth (Table 2). Water extraction depresses the water table on the eastern and western edges of BSF, increasing the dissolution-susceptible vadose zone (Lines, 1979; Mason & Kipp, 1998). Water removed from the saline pan aquifer by mining may increase the upward flow gradient of halite-undersaturated lacustrine-sediment aquifer brines into the saline pan aquifer. Anthropogenic activities may decouple some aspects of BSF sedimentation from natural hydroclimatic processes.

The Bonneville Salt Flats within the closed-basin sedimentary cycle

Benison & Goldstein (1999, 2000) describe saline pans as a stage in the closed-basin sedimentary cycle. Perennial freshwater lakes, followed by shallow saline lakes, pre-date saline pans in the cycle. The sediments underlying BSF reflect this with a shift from laminated aragonitic muds to aragonite mixed with gypsum (Fig. 1C). The saline lake then shifts to a shallow saline pan, which is reflected at BSF by decreasing spacing between horizontal dissolution surfaces over time, indicating smaller flooding and evapoconcentration stages. The saline pan transitions into a saline mudflat in the next phase of the cycle. Observations of sediments with high porosities, and prior studies indicating decreasing volume and areal extent of persistent halite crust, indicate that BSF is shifting towards a saline mudflat depositional environment similar to the current mudflat at its edge (Bowen *et al.,* 2017, 2018b; Kipnis & Bowen, 2018).

CONCLUSIONS

Evaporite deposition and alteration at the Bonneville Salt Flats are influenced by saline pan stages, variable groundwater levels, vertical groundwater fluxes and surficial sedimentary structures. Brine chemistry, presence and degree of halite saturation within saline pans are controlled by seasonal to daily changes in temperature, evaporation and fluid inputs. Across the saline pan stages of flooding, evapoconcentration and desiccation, the juxtaposition of different evaporite structures and brines of different mineral saturation states and variable water levels over time lead to a diversity of evaporite morphologies developed at the surface, vadose and phreatic zones in saline pans (Fig. 14). Seasonal changes within the vertical hydraulic gradient between the saline-sediment hosted aquifer and the underlying halite-undersaturated aquifer affect brine salinity and may influence evaporite morphologies. Sedimentary structures created by the desiccation of surface crusts, such as polygonal fractures, influence the development of secondary porosity. The evaporite sequence at the Bonneville Salt Flats shows increasing alteration and poor preservation of primary halite morphologies. Most gypsum formed *in situ* and was reworked. Gypsum crystals continued to grow over time. This poor halite preservation, linked with past studies of the system and declining water levels (Kipnis & Bowen, 2018), indicates that the system is nearing the end of the saline pan stage of the closed basin cycle. Consideration of these sedimentological examples and environmental processes could improve saline pan depositional models and interpretation of altered evaporites.

ACKNOWLEDGEMENTS

The authors acknowledge that this study was conducted on traditionally Newe/Western Shoshone

and Goshute lands. Field and laboratory assistance for this research were provided by Evan Kipnis, Jory Lerback, Elliot Jagniecki, Benjamin Marconi, Hannah Stinson, Lily Wetterlin, Mark Radwin, Amanda Jayo, and Melissa Wolfe. Jan Miller and Chen-Lun Lin facilitated the CT analysis of samples. We thank John Longino for identification of insects at BSF and discussion of salt blisters. This manuscript was much improved through discussions with Marie Jackson, Elliot Jagniecki, Jory Lerback, Evan Kipnis, and Ido Sirota and the helpful comments of Kathleen Benison, Nadav Lensky, Tim Lowenstein and an anonymous reviewer. Kathleen Ritterbush provided access to the Zeiss microscope. This work was made possible with the support of the BLM West Desert District office staff, including Kevin Oliver, Matt Preston, Mike Nelson, Cheryl Johnson, Steve Allen, and Roxanne Tea. The support of Intrepid Potash, including Craig Peterson and Russ Draper, contributed to the success of this project. Funding for this research was provided by a NSF Coupled Natural Human Systems Award #1617473 to Brenda Bowen and a Geological Society of America Graduate Student Research Grant and Colorado Scientific Society Research Grant.

DATA AVAILABILITY STATEMENT

The data that support the findings of this study are openly available in Zenodo at https://doi.org/10.5281/zenodo.4171331, https://doi.org/10.5281/zenodo.4268710, https://doi.org/10.5281/zenodo.4197277 and https://doi.org/10.5281/zenodo.4167214.

REFERENCES

Anati, D.A. (1999) The salinity of hypersaline brines: concepts and misconceptions. *Int. J. Salt Lake Res.*, **8**, 55–70.

Arthurton, R.S. (1973) Experimentally produced halite compared with Triassic layered halite rock from Cheshire, England. *Sedimentology*, **20**, 145–160.

Benison, K.C., **Bowen, B.B.**, **Oboh-Ikuenobe, F.E.**, **Jagniecki, E.A.**, **LaClair, D.A.**, **Story, S.L.**, **Mormile, M.R.** and **Hong, B.Y.** (2007) Sedimentology of acid saline lakes in southern Western Australia: newly described processes and products of an extreme environment. *J. Sediment. Res.*, **77**, 366–388.

Benison, K.C. and **Goldstein, R.H.** (1999) Permian paleoclimate data from fluid inclusions in halite. *Chem. Geol.*, **154**, 113–132.

Benison, K.C. and **Goldstein, R.H.** (2000) Sedimentology of ancient saline pans: an example from the Permian Opeche Shale, Williston Basin, North Dakota, U.S.A. *J. Sediment. Res.*, **70**, 159–169.

Benison, K.C. and **Goldstein, R.H.** (2001) Evaporites and siliciclastics of the Permian Nippewalla Group of Kansas, USA: a case for non-marine deposition in saline lakes and saline pans. *Sedimentology*, **48**, 165–188.

Bobst, A.L., **Lowenstein, T.K.**, **Jordan, T.E.**, **Godfrey, L.V.**, **Ku, T.-L.-T.-L.** and **Luo, S.** (2001) A 106 ka paleoclimate record from the Salar de Atacama, northern Chile. *Paleogeography Palaeoclimatol. Palaeoecol.*, **173**, 21–42.

Bowen, B.B., **Bernau, J.**, **Kipnis, E.**, **Lerback, J.**, **Wetterlin, L.** and **Kleba, B.** (2018a) The making of a perfect racetrack at the Bonneville Salt Flats. *Sediment. Rec.*, **16**, 4–11.

Bowen, B.B., **Kipnis, E.L.** and **Raming, L.W.** (2017) Temporal dynamics of flooding, evaporation, and desiccation cycles and observations of salt crust area change at the Bonneville Salt Flats, Utah. *Geomorphology*, **299**, 1–11.

Bowen, B.B., **Kipnis, E.L.** and **Pechmann, J.M.** (2018b) Observations of salt crust thickness change at the Bonneville Salt Flats from 2003–2016. In: *Geofluids of Utah*, 47th edn, pp. 247–285. Utah Geological Association Publication. 5

Braitsch, O. (1971) *Salt Deposits, Their Origin and Composition*. Springer, Berlin, Berlin, 297 pp.

Brooks, S.J. (1991) A comparison of salt thickness on the Bonneville Salt Flats, Tooele County, Utah during July 1960, October 1974, and October 1988. *Bureau of Land Management*. 6

Buades, A., **Coll, B.** and **Morel, J.-M.** (2011) Non-local means denoising. *Image Process. Line*, **1**, 208–212.

Casas, E. and **Lowenstein, T.K.** (1989) Diagenesis of saline pan halite: comparison of petrographic features of modern, Quaternary and Permian halites. *J. Sediment. Petrol.*, **59**, 724–739.

Christiansen, F.W. (1963) Polygonal fracture and fold systems in the salt crust, Great Salt Lake Desert. *Science*, **139**(3555), 607–609.

Christiansen, J.E., **Watkins, R.K.**, **Thorne, J.P.**, **Nielson, D.**, **Patil, B.B.**, **Judd, H.**, **Hill, R.O.**, **Thorpe, J.D.**, **Tea, R.D.**, **Davis, S.C.** and **Frandsen, A.D.** (1962) Salt Flats investigations: Utah State University Engineering Experiment Station. In: *Salt Flats Annual Progress Report, Parts VI–XIII*. 7

Conner, A.J. and **Benison, K.C.** (2013) Acidophilic halophilic microorganisms in fluid inclusions in halite from Lake Magic, Western Australia. *Astrobiology*, **13**, 850–860.

Craft, K.M. and **Horel, J.D.** (2019) Variations in surface albedo arising from flooding and desiccation cycles on the Bonneville salt flats, Utah. *J. Appl. Meteorol. Climatol.*, **58**, 773–785.

Crittenden, M.D. (1963) *New Data on the Isostatic Deformation of Lake Bonneville*. Washington D.C., 1–31 pp.

Darbon, J., **Cunha, A.**, **Chan, T.F.**, **Osher, S.** and **Jensen, G.J.** (2008) Fast nonlocal filtering applied to electron cryomicroscopy. In: *2008 5th IEEE International Symposium on Biomedical Imaging: From Nano to Macro, Proceedings, ISBI*, pp. 1331–1334.

Dashtian, H., **Shokri, N.** and **Sahimi, M.** (2018) Pore-network model of evaporation-induced salt precipitation in porous media: the effect of correlations and heterogeneity. *Adv. Water Resour.*, **112**, 59–71.

Davis, D.W., **Lowenstein, T.K.** and **Spencer, R.J.** (1990) Melting behavior of fluid inclusions in laboratory-grown halite crystals in the systems NaCl-H_2O, NaCl-KCl-H_2O,

NaC-$MgCl_2$-H_2O, and NaCl-$CaCl_2$-H_2O. *Geochim. Cosmochim. Acta*, **54**, 591–601.

Dellwig, L.F. (1955) Origin of the Salina salt of Michigan. *J. Sediment. Res.*, **25**, 83–110.

Dickinson, W.R. (2006) Geotectonic evolution of the Great Basin. *Geosphere*, **2**, 353–368.

Dubessy, J., **Sretenskaya, N.**, **Boiron, M.C.**, **Moissette, A.** and **Monnin, C.** (1992) Determinations of water, hydrates and pH in fluid inclusions by micro-Raman spectrometry. *Eur. J. Mineral.*, **4**, 885–894.

Duffy, C.J. and **Al-Hassan, S.** (1988) Groundwater circulation in a closed desert basin: Topographic scaling and climatic forcing. *Water Resour. Res.*, **24**, 1675–1688.

Eardley, A.J. (1962) Gypsum dunes and evaporite history of the Great Salt Lake Desert. *Utah Geological and Mineral Survey*, 1–27.

Eloukabi, H., **Sghaier, N.**, **Ben Nasrallah, S.** and **Prat, M.** (2013) Experimental study of the effect of sodium chloride on drying of porous media: the crusty-patchy efflorescence transition. *Int. J. Heat Mass Transf.*, **56**, 80–93.

Goldstein, R.H. (2001) Clues from fluid inclusions. *Science*, **294**, 1009–1011.

Goldstein, R. and **Reynolds, J.** (1994) Systematics of fluid inclusions in diagenetic minerals: Society for Sedimentary Geology. 1–199 pp.

Goldstein, R.H., **Reynolds, T.J.** and **Reynolds, J.** (1994) Systematics of fluid inclusions in diagenetic minerals. 199 pp.

Goodall, T.M., **North, C.P.** and **Glennie, K.W.** (2000) Surface and subsurface sedimentary structures produced by salt crusts. *Sedimentology*, **47**, 99–118.

Gornitz, V. and **Schreiber, B.C.** (1981) Displacive halite hoppers from the Dead Sea: some implications for ancient evaporite deposits. *Sediment. Petrol.*, **51**, 787–794.

Hardie, L.A., **Lowenstein, T.K.** and **Spencer, R.J.** (1985) The problem of distinguishing between primary and secondary features in evaporites. *Sixth Int. Symp. Salt*, **1**, 173–195.

Holt, R.M. and **Powers, D.W.** (2011) Synsedimentary dissolution pipes and the isolation of ancient bacteria and cellulose. *Bull. Geol. Soc. Am.*, **123**, 1513–1523.

Horel, J., **Splitt, M.**, **Dunn, L.**, **Pechmann, J.**, **White, B.**, **Ciliberti, C.**, **Lazarus, S.**, **Slemmer, J.**, **Zaff, D.** and **Burks, J.** (2002) Mesowest: cooperative mesonets in the western United States. *Bull. Am. Meteorol. Soc.*, **83**, 211–225.

Hovorka, S.D. (1987) Depositional environments of marine-dominated bedded halite, Permian San Andres Formation, Texas. *Sedimentology*, **34**, 1029–1054.

Hsu, K.J. and **Siegenthaler, C.** (1969) Preliminary experiments on hydrodynamic movement induced by evaporation and their bearing on the dolomite problem. *Sedimentology*, **12**, 11–25.

Hunt, C. (1966) Hydrologic basin, Death Valley, California (Vol. **494**). *US Government Printing Office*.

Jones, D.J. (1953) Gypsum-oolite dunes, Great Salt Lake Desert, Utah. *AAPG Bull.*, **37**, 2530–2538.

Kampf, S.K., **Tyler, S.W.**, **Ortiz, C.A.**, **Muñoz, J.F.** and **Adkins, P.L.** (2005) Evaporation and land surface energy budget at the Salar de Atacama, Northern Chile. *J. Hydrol.*, **310**, 236–252.

Kipnis, E.L. and **Bowen, B.B.** (2018) Observations of salt crust change from 1960–2016 and the role of humans as geologic agents at the Bonneville Salt Flats, Utah. In: *Geofluids of Utah*, 47th edn, pp. 287–301 Utah Geological Association Publication.

Kipnis, E.L., **Bowen, B.B.**, **Hutchings, S.J.**, **Hynek, S.A.** and **Benison, K.C.** (2020) Major ion geochemistry in Na-Ca-Mg-K-Cl-SO4 brines using portable X-ray fluorescence spectrometry. *Chem. Geol.*, 135577.

Lazar, B. and **Holland, H.D.** (1988) The analysis of fluid inclusions in halite. *Geochim. Cosmochim. Acta*, **52**, 485–490.

Li, J., **Lowenstein, T.K.**, **Brown, C.B.**, **Ku, T.L.** and **Luo, S.** (1996) A 100 ka record of water tables and paleoclimates from salt cores, Death Valley, California. *Palaeogeogr. Palaeoclimatol. Palaeoecol.*, **123**, 179–203.

Lines, G.C. (1979) Hydrology and surface morphology of the Bonneville Salt Flats and Pilot Valley playa, Utah. *Geol. Surv. Water-Supply Pap.*, **2057**, 1–107.

Lokier, S. and **Steuber, T.** (2009) Large-scale intertidal polygonal features of the Abu Dhabi coastline. *Sedimentology*, **56**, 609–621.

Lowenstein, T.K. (2012) Microorganisms in evaporites: review of modern geomicrobiology. In: *Advances in Understanding the Biology of Halophilic Microorganisms*, pp. 117–139.

Lowenstein, T.K. and **Hardie, L.A.** (1985) Criteria for the recognition of salt-pan evaporites. *Sedimentology*, **32**, 627–644.

Macumber, P.G. (1991) *Interaction Between Groundwater and Surface Systems in Northern Victoria*. Department of Conservation and Environment.

Mason, J.L. and **Kipp, K.L.** (1998) Hydrology of the Bonneville Salt Flats, Northwestern Utah, and Simulation of Ground-Water Flow and Solute Transport in the Shallow-Brine Aquifer. 108 pp.

McGonigle, J.M., **Bernau, J.A.**, **Bowen, B.B.** and **Brazelton, W.** (2019) Robust archaeal and bacterial communities inhabit shallow subsurface sediments of the Bonneville Salt Flats. *mSphere*, **4**, e00378-19.

McMillan, D. (1974) Bonneville Salt Flats: A comparison of salt thickness in July 1960 and October 1974. 189–192 pp.

Meyer, F.A. (1960) Effect of temperature on ground-water levels. *J. Geophys. Res.*, **65**(6), 1747–1752.

Mormile, M.R. and **Storrie-Lombardi, M.** (2005) The use of ultraviolet excitation of native fluorescence for identifying biomarkers in halite crystals (5906A-27). *Proc. SPIE Vol. 5906, Astrobiol. Planet. Mission*, **5906**, 246–253.

Nachshon, U., **Weisbrod, N.**, **Dragila, M.I.** and **Grader, A.** (2011) Combined evaporation and salt precipitation in homogeneous and heterogeneous porous media. *Water Resour. Res.*, **47**, 1–16.

Noeth, L.A. (2002) *Bonneville: The Fastest Place on Earth*. MotorBooks International.

Nolan, T.B. (1927) Potash Brines in the Great Salt Lake Desert, Utah. In: *Chapter B in Contributions to Economic Geology (Short Papers and Preliminary Reports)*, No. 795-B. US Government Printing Office, 25–44.

Olivella, S., **Castagna, S.**, **Alonso, E.E.** and **Lloret, A.** (2011) Porosity variations in saline media induced by temperature gradients: Experimental evidences and modelling. *Transp. Porous Media*, **90**, 763–777.

Oviatt, C.G. (2014) The Gilbert Episode in the Great Salt Lake Basin, Utah. *Utah Geol. Surv.*, Miscellane, 1–20.

Oviatt, C.G. (2015) Chronology of Lake Bonneville, 30,000 to 10,000 yr BP. *Quat. Sci. Rev.*, **110**, 166–171.

Oviatt, C.G., **Madsen, D.B.**, **Miller, D.M.**, **Thompson, R.S.** and **McGeehin, J.P.** (2015) Early Holocene Great Salt Lake, USA. *Quat. Res.*, **84**, 57–68.

Post, V., **Kooi, H.** and **Simmons, C.** (2007) Using hydraulic head measurements in variable-density ground water flow analyses. *Ground Water*, **45**, 664–671.

Powers, D.W. and **Hassinger, B.W.** (1985) Synsedimentary dissolution pits in halite of the Permian Salado Formation,

southeastern New Mexico. *J. Sediment. Petrol.*, **55**, 769–773.

Putnis, A. and **Mauthe, G.** (2001) The effect of pore size on cementation in porous rocks. *Geofluids*, **1**, 37–41.

Radwin, M.H. and **Bowen, B.B.** (2021) Mapping mineralogy in evaporite basins through time using multispectral Landsat Data: examples from the Bonneville Basin, Utah, USA. *Earth Surf. Process. Landforms*, esp.5089.

Raup, O.B. (1970) Brine Mixing: an Additional Mechanism for Formation of Basin Evaporites. *AAPG Bull*. https://doi.org/10.1306/5d25cc8d-16c1-11d7-8645000102c1865d

Reheis, M. and **Kihl, R.** (1995) Dust deposition in southern Nevada and California, 1984–1989: relations to climate, source area, and source lithology. *J. Geophys. Res.*, **100**, 8893–8918.

Roberts, S.M. and **Spencer, R.J.** (1995) Paleotemperatures preserved in fluid inclusions in halite. *Geochim. Cosmochim. Acta*, **59**, 3929–3942.

Roedder, E. (1984a) The fluids in salt. *Am. Mineral.*, **69**, 413–439.

Roedder, E. (1984b) Volume 12: fluid inclusions. *Mineral. Soc. Am.*, 1–646.

Rosasco, G.J. and **Roedder, E.** (1979) Application of a new Raman microprobe spectrometer to nondestructive analysis of sulfate and other ions in individual phases in fluid inclusions in minerals. *Geochim. Cosmochim. Acta*, **43**, 1907–1915.

Schindelin, J., **Arganda-Carreras, I.**, **Frise, E.**, **Kaynig, V.**, **Longair, M.**, **Pietzsch, T.**, **Preibisch, S.**, **Rueden, C.**, **Saalfeld, S.**, **Schmid, B.**, **Tinevez, J.Y.**, **White, D.J.**, **Hartenstein, V.**, **Eliceiri, K.**, **Tomancak, P.** and **Cardona, A.** (2012) Fiji: an open-source platform for biological-image analysis. *Nat. Methods*, **9**, 676–682.

Schubel, K.A. and **Lowenstein, T.K.** (1997) Criteria for the recognition of shallow-perennial-saline-lake halites based on recent sediments from the Qaidam Basin, Western China. *J. Sediment. Res.*, **67**(1), 74–87.

Shearman, D.J. (1970) Recent halite rock, Baja California, Mexico. *Institute of Mining and Metallurgy Transactions*, vol. **79**, pp. B155–B162.

Shokri-Kuehni, S.M.S., **Vetter, T.**, **Webb, C.** and **Shokri, N.** (2017) New insights into saline water evaporation from porous media: complex interaction between evaporation rates, precipitation, and surface temperature. *Geophys. Res. Lett.*, **44**, 5504–5510.

Sirota, I., **Arnon, A.** and **Lensky, N.G.** (2016) Seasonal variations of halite saturation in the Dead Sea. *Water Resour. Res.*, **52**, 7151–7162.

Smith, R.P., **Breckenridge, R.P.** and **Wood, T.R.** (2012) *Assessment of Geothermal Resource Potential at a High-Priority Area on the Utah Testing and Training Range-South (UTTR-S)*. Idaho Falls, ID.

Smoot, J.P. and **Castens-Seidell, B.** (1994) Sedimentary features produced by efflorescent salt crusts, Saline Valley and Death Valley, California. *Sedimentol. Geochem. Mod. Anc. Saline Lakes*, 73–90.

Southgate, P. (1982) Cambrian skeletal halite crystals and experimental analogues. *Sedimentology*, **29**, 391–407.

Spencer, R.J., **Baedecker, M.J.**, **Eugster, H.P.**, **Forester, R.M.**, **Goldhaber, M.B.**, **Jones, B.F.F.**, **Kelts, K.**, **Mckenzie, J.**, **Madsen, D.B.**, **Rettig, S.L.**, **Rubin, M.** and **Bowser, C.J.** (1984) Great Salt Lake, and precursors, Utah: the last 30,000 years. *Contrib. Mineral. Petrol.*, **86**, 321–334.

Taj, R.J. and **Aref, M.A.** (2015) Structural and textural characteristics of surface halite crusts of a supratidal, ephemeral halite pan, South Jeddah, Red Sea Coast, Saudi Arabia. *Facies*, **61**. https://doi.org/10.1007/s10347-014-0426-0

Tanaka, M., **Girard, G.**, **Davis, R.**, **Peuto, A.** and **Bignell, N.** (2001) Recommended table for the density of water between 0°C and 40°C based on recent experimental reports. *Metrologia*, **38**, 301–309.

Turk, L.J. (1973) *Hydrogeology of the Bonneville Salt Flats*. Salt Lake City, 1–82 pp.

Turk, L.J. (1975) Diurnal fluctuations of water tables induced by atmospheric pressure changes. *J. Hydrol.*, **26**, 1–16.

Valyashko, M. (1972) Playa lakes - a necessary stage in the development of a salt-bearing basin. In: *Geology of Saline Deposits*, pp. 41–52.

Videla, A.R., **Lin, C.L.** and **Miller, J.D.** (2008) Simulation of saturated fluid flow in packed particle beds - The lattice-Boltzmann method for the calculation of permeability from XMT images. *J. Chin. Inst. Chem. Eng.*, **39**, 117–128.

White, W.W. (2002) Salt Laydown Project - Replenishment of Salt to the Bonneville Salt Flats. In: *Great Salt Lake: An Overview of Change*, pp. 433–486.

White, W.W. and **Terrazas, M.** (2006) Analysis of recent and historical salt-crust thickness measurements and assessment of their relationship to the salt laydown project, Bonneville Salt Flats, Tooele County, Utah. Salt Lake City, 1–31.

Wold, S.R. and **Waddell, K.M.** (1994) Salt Budget for West Pond, Utah, April 1987 to June 1989. Water-Resources Investigations Report 93-4028.

APPENDIX A. TIME LAPSE AND FIELD IMAGERY

Surface observations of BSF crust across salinepan stages (Fig. A1) and across a range of surface morphologies (Fig. A2). Note the raised circular blister shown in Fig. A1B3. The relationship between surface halite layer thickness and surface morphology is shown in Fig. A3. Time-lapse imagery from the BFLAT weather station can be found online at http://home.chpc.utah.edu/~u0790486/wxinfo/cgi-bin/uunet_came

COLOR

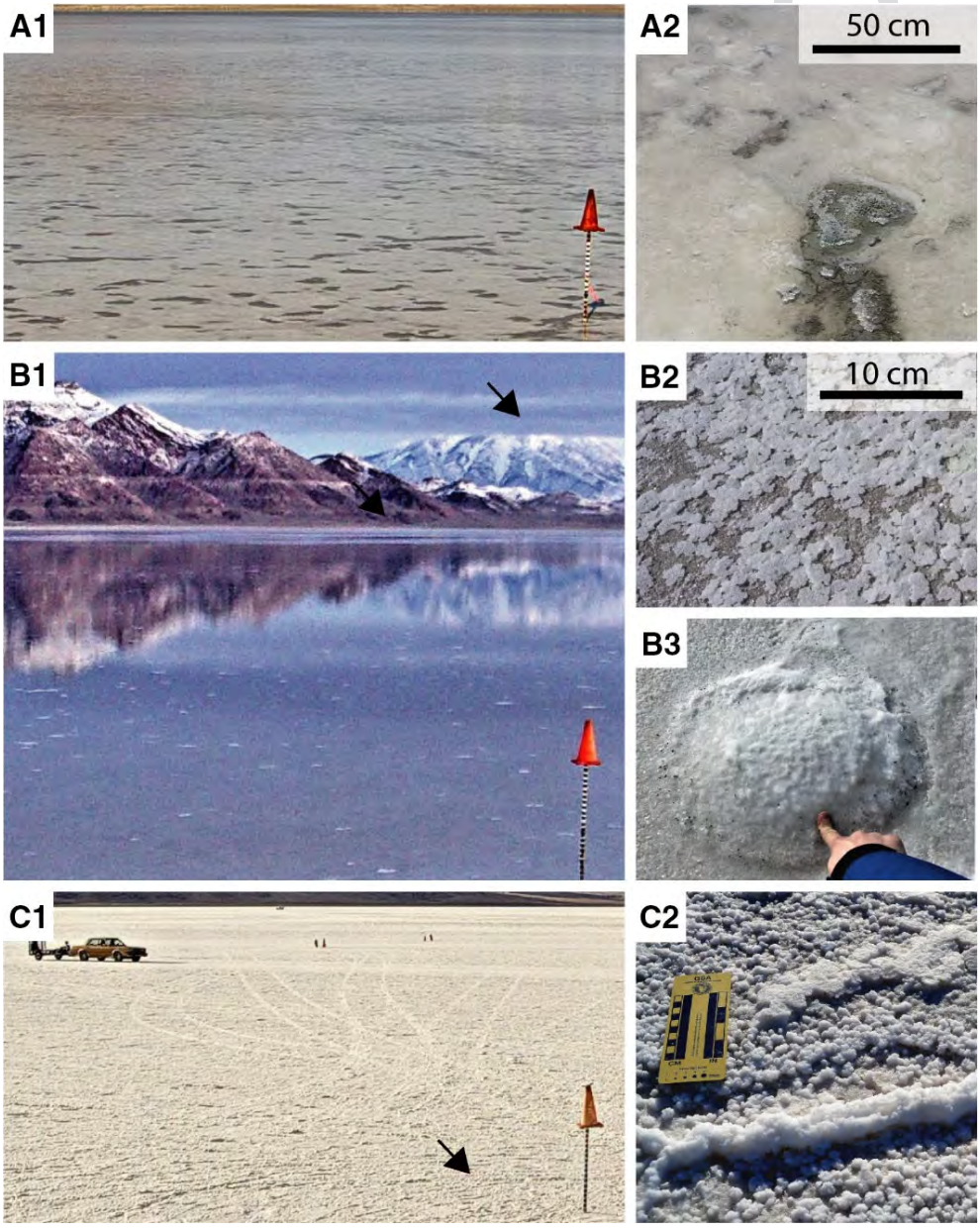

Fig. A1. Surface observations of the Bonneville Salt Flats during different hydrological stages. Images on the left were taken with a time-lapse camera on the weather station, traffic cone shown for scale. (A) Flooding stage with dissolution pits exposing darker underlying gypsum layers. (B1-B2) Evapoconcentration stage with cumulate rafts forming on the surface. Note the horizontal lines on the mountains demarcating Lake Bonneville shorelines. (B3) Circular raised blisters, finger for scale. (C) Desiccation stage with efflorescent halite and ridges. Most recreation occurs during this stage. Image dates: (A1) October 3, 2019, (A2) May 15, 2018. (B1) March 11, 2019, (B2) November 6, 2016, (B2) December 18, 2017, (C1) September 14, 2017, (C2) September 5, 2016.

COLOR

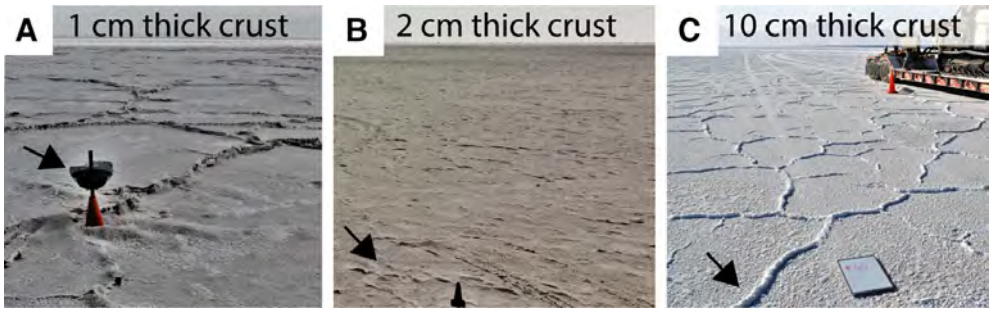

Fig. A2. Images of primary types of surficial sedimentary structures. (A) Pressure-buckled halite crust at the saline pan's eastern edge. Dust trap on left (arrow). Traffic cone for scale in (A) and (B). (B) relatively flat crust near middle of saline pan with small pressure buckles and efflorescent ridges (arrow). Surface halite layer is two centimetres thick. (C) Polygonal fractures filled by efflorescent ridges (arrow) in area with 10-cm-thick surface halite layer. Image dates and locations: (A) September 14, 2017 (Dust-3), (B) September 9, 2020 (weather station), (C) September 7, 2016 (D-60).

COLOR

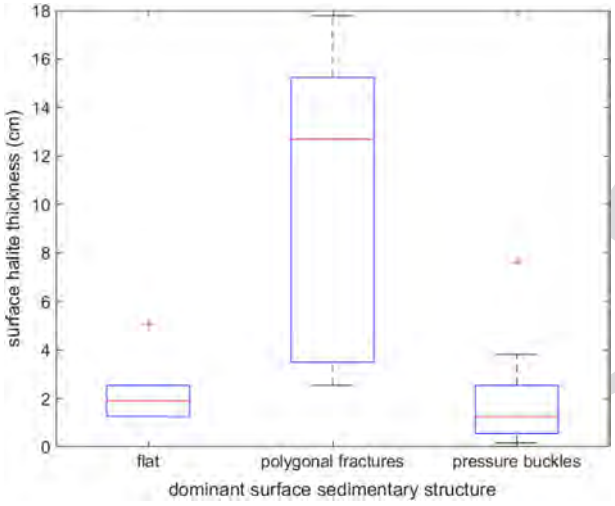

Fig. A3. Surficial sedimentary structures observed at the end of the desiccation stage and associated crust thicknesses (Table A2). Flat and pressure buckled crust occurs in areas with thin (ca 2 cm-thick) crust, while polygonally fractured crust is thicker. Flat crust is concentrated along the western edge of BSF where seasonal ponding is persistent (Bowen *et al.,* 2017; Craft & Horel, 2019). Polygonal fractures are concentrated within and to the north-east of the Salduro Loop. Pressure buckles consistently occur at saline pan edges.

ra_explorer.cgi (Camera: Bonneville Salt Flats) and along with imagery from other locations (Table A1) at https://doi.org/10.5281/zenodo.4171331.

Table A1. Time-lapse imagery locations and camera types.

Location name	Latitude	Longitude	Camera type(s)
BFLAT	40.784636°	−113.829749°	Brinno TLC200; Axis Communications web camera
LEMSA	40.765730°	−113.784140°	Brinno TLC200
LEMSB	40.761325°	−113.844183°	Brinno TLC200

Table A2. Surface layer halite thickness and dominant surface sedimentary structure recorded in September 2016 (in association with Bowen *et al.,* 2018).

Core ID	Latitude	Longitude	Dominant surface sedimentary structure	Surface halite layer thickness (cm)
D-02	40.86465596	−113.756457	Pressure buckles	1.3
D-03	40.86129595	−113.752766	NA	NA
D-04	40.85590411	−113.746705	Flat	1.3
D-05	40.850298	−113.740494	Pressure buckles	1.3
D-06	40.86229385	−113.76634	NA	NA
D-07	40.85109981	−113.754008	Flat	1.3
D-08	40.84586735	−113.748137	NA	NA
D-09	40.85281402	−113.78085	Pressure buckles	1.3
D-10	40.84737991	−113.774781	Flat	2.5
D-11	40.8417149	−113.768771	Pressure buckles	2.5
D-12	40.82899447	−113.754479	NA	NA
D-13	40.83846444	−113.7898	Pressure buckles	1.3
D-14	40.83247636	−113.783255	Flat	2.5
D-15	40.82130043	−113.770984	NA	NA
D-16	40.81576683	−113.764811	NA	NA
D-17	40.81029867	−113.758703	Pressure buckles	0.3
D-18	40.8317475	−113.807495	NA	NA
D-19	40.81202881	−113.785622	NA	NA
D-20	40.80649049	−113.779542	NA	NA
D-21	40.8009573	−113.773369	NA	NA
D-22	40.81940429	−113.81864	NA	NA
D-23	40.81379657	−113.812521	NA	NA
D-24	40.80275545	−113.800242	Flat	2.5
D-25	40.79161413	−113.787938	NA	NA
D-26	40.78609781	−113.781838	NA	NA
D-27	40.81150945	−113.834651	Pressure buckles	0.2
D-28	40.80450888	−113.827057	NA	NA
D-29	40.79349134	−113.814864	Flat	2.5
D-30	40.78240099	−113.802618	NA	NA
D-31	40.77128724	−113.79031	NA	NA
D-32-2	40.80069416	−113.847702	Pressure buckles	2.5
D-33	40.79525798	−113.841705	Pressure buckles	3.8
D-34	40.7842146	−113.829461	Flat	1.3
D-35	40.76790735	−113.811532	Pressure buckles	1.3
D-36	40.78868735	−113.859362	Pressure buckles	1.3
D-37	40.75746238	−113.824861	Flat	5.1
D-38	40.74719054	−113.813298	Polygonal fractures	17.8
D-39	40.77659723	−113.870946	Pressure buckles	0.6
D-41	40.76852012	−113.886781	Flat	1.3
D-42	40.76416628	−113.88194	Polygonal fractures	15.2
D-43	40.74526226	−113.860979	Flat	1.3
D-44	40.75934984	−113.901557	Flat	2.5
D-45	40.75155906	−113.91789	Polygonal fractures	12.7
D-46	40.74881291	−113.914653	Flat	1.3
D-48	40.74534954	−113.9263	Pressure buckles	1.3
D-49	40.74204245	−113.922144	NA	NA
D-50	40.7463882	−113.887093	NA	NA
D-51	40.74888132	−113.840229	NA	NA
D-52	40.75630236	−113.873357	Polygonal fractures	2.5
D-53	40.76195867	−113.804892	Polygonal fractures	3.8
D-54	40.76299847	−113.830926	Polygonal fractures	8.9
D-55	40.76573254	−113.78414	NA	NA
D-56	40.77309283	−113.817193	Polygonal fractures	12.7
D-57	40.7772148	−113.79685	Pressure buckles	0.2
D-58	40.7786566	−113.82333	Polygonal fractures	2.5

Table A2. (continued)

Core ID	Latitude	Longitude	Dominant surface sedimentary structure	Surface halite layer thickness (cm)
D-59	40.78056464	−113.775631	NA	NA
D-60	40.77939422	−113.873894	Polygonal fractures	15.2
D-61	40.78793265	−113.808733	NA	NA
D-62	40.79544563	−113.767284	Pressure buckles	7.6
D-63	40.79717406	−113.794075	NA	NA
D-64	40.80281142	−113.850116	Pressure buckles	0.3
D-65	40.82305496	−113.797814	NA	NA
D-66	40.8228829	−113.822376	Pressure buckles	3.8
D-67	40.82863615	−113.803882	NA	NA
D-68	40.83068555	−113.756371	NA	NA
D-69	40.84356297	−113.795465	NA	NA
D-70	40.8566778	−113.760148	Flat	1.3

APPENDIX B. WEATHER STATION DATA

Weather station data was collected from the MesoWest weather station data repository found online at https://mesowest.utah.edu/, station ID: BFLAT (Horel *et al.,* 2002). Incoming and outgoing longwave and shortwave radiation were measured with an Apogee SN-500 net radiometer (Logan, Utah, USA). Albedo was calculated using equation B-1, where the integral of daily outgoing shortwave radiation (SW_{out}) between sunrise and sunset (dt) is divided by the sum of daily incoming shortwave radiation (SW_{in}) over the same period.

$$\text{Albedo} = \frac{\int SW_{out}\,dt}{\int SW_{in}\,dt} \quad \text{(B1)}$$

APPENDIX C. PRESSURE-TEMPERATURE TRANSDUCER AND BRINE SAMPLE DATA

Pressure transducers were installed at several wells (Table C1) from June 2017 to December 2020 (data available at https://doi.org/10.5281/zenodo.4268710). Logged water depth below the surface was calculated using brine density and the measured depth to water (Table C2), if available. Brine density and temperature were measured in the field with a digital hydrometer at the beginning and end of the logging period. (Table C3; Densito 30PX, Mettler Toledo, Columbus, Ohio, USA). Samples were collected from specific depths within some wells by using small-diameter tubing (1.59 mm inner diameter) at set depths in the well to collect samples (Table C2).

Seasonal temperature-controlled (0 to 30°C) changes in brine density are less than 0.01 g cm^{-3} (Fig. D3). These density changes would lead to <1 centimetre of water column height change for one meter of water column, making density-controlled changes in measured water column minor relative to other processes. Seasonal variations in salinity with temperature fluctuations contributed to larger density changes (<0.025 g cm^{-3}; Table C2; Fig. C1).

To prevent potential corrosion, transducers installed before June 2020 were sealed in plastic bags that were filled with tap water. Excess water and air bubbles were removed from bags before they were sealed. Transducers installed after June 2020 were not placed in bags. Two or more transducers were installed in some wells to observe vertical thermal gradients. Transducers were attached to plastic rods to ensure that they did not move while logging data and to ensure that they were installed at consistent depths between data retrievals.

To make the water level of the co-located wells of BLM-93 and BLM-93C directly comparable, the equivalent pressure head was calculated for each well (equation C1). The equivalent pressure head corrects hydraulic head measurements for differences in density and screened interval (Post *et al.,* 2007). The brine density for each well was extrapolated between measurements using shape-filling cubic interpolation (Fig. C1).

$$h_1 = \frac{\rho_2}{p_1} * h_2 - \frac{p_2 - p_1}{p_1} * z \quad \text{(C1)}$$

Equation to calculate equivalent or freshwater head for wells with variable water density.

Table C1. Well construction parameters, including screened intervals and water sample locations. BLM-93C is the only well completely screened within saline pan sediments. The depth of the saline pan base was extrapolated from borings collected by Bowen *et al.* (2018b). The wells and sites listed here were sampled (Tables C2 and D1) or had their water level measured (https://doi.org/10.5281/zenodo.4268710), only the wells with the best data continuity are shown on Figs 1B and 4C to E (BLM-93C, BLM-93, BLM-34 and BLM-37).

			Casing			Screened interval relative to total casing length			Reported Screened interval Measurements Below Surface (Mason et al., 1995)		
Site/Well ID	Latitude	Longitude	Casing top height above surface* (m)	Casing width (cm)	Total casing length (m)	From (m)	To (m)	Saline pan base below surface (m)	Upper (m)	Lower (m)	Total Depth (m)
BLM-6	40.739110°	−113.822520°	NA	6.35	NA	NA	NA	ca 0.70	0.76	5.79	5.79
BLM-12†	40.741049°	−113.912796°	0.52	5.08	6.31	3.26	6.31	0.61	2.74	5.79	5.79
BLM-17	40.776880°	−113.912240°	NA	NA	NA	NA	NA	ca 10	0.91	2.44	2.44
BLM-19	40.805768°	−113.878906°	0.32	6.35	3.06	1.54	3.06	NA	1.22	2.74	2.74
BLM-22a	40.847711°	−113.853628°	0.27	5.08	4.53	2.70	4.23	NA	2.44	3.96	4.27
BLM-31	40.776800°	−113.768250°	0.43	5.08	3.17	1.34	2.87	0.30	0.91	2.44	2.74
BLM-34	40.762437°	−113.795570°	0.18	5.08	1.71	0.49	1.71	0.25	0.30	1.52	1.52
BLM-37	40.761325°	−113.844183°	0.51	6.35	5.08	2.04	5.08	1.65	1.52	4.57	4.57
BLM-41	40.776327°	−113.788070°	0.24	6.35	5.73	2.68	5.73	0.33	2.44	5.49	5.49
BLM-43A	40.811881°	−113.823627°	0.21	22.00	4.24	NA	NA	0.58	NA	NA	4.02
BLM-45	40.815490°	−113.780014°	0.49	5.08	3.23	1.55	3.08	0.64	1.07	2.59	2.74
BLM-50A	40.817436°	−113.757747°	0.24	5.08	4.66	NA	NA	0.32	NA	NA	4.42
BLM-50B	40.817436°	−113.757747°	0.51	5.08	3.04	2.09	2.86	0.32	1.58	2.35	2.53
BLM-53	40.817424°	−113.750287°	0.27	5.08	4.84	NA	NA	0.13	NA	NA	4.57
BLM-53A	40.817424°	−113.750287°	0.74	5.08	20.86	16.74	19.79	0.13	16.00	19.05	20.12
BLM-53B	40.817424°	−113.750287°	0.49	5.08	3.08	1.87	2.66	0.13	1.37	2.16	2.59
BLM-63	40.818267°	−113.844183°	0.27	5.08	3.31	NA	NA	0.00	NA	NA	3.04
BLM-64	40.834937°	−113.821683°	0.31	5.08	3.05	3.05	1.52	ca 0.15	2.74	1.22	2.74
BLM-93	40.784636°	−113.829749°	0.96	10.16	4.62	2.94	4.47	0.77	1.98	3.51	3.66
BLM-93A	40.784636°	−113.829749°	0.75	5.08	19.95	16.60	19.64	0.77	15.85	18.90	19.20
BLM-93C	40.784636°	−113.829749°	0.49	5.08	1.26	0.65	1.26	0.77	0.15	0.76	0.76
BLM-93D	40.784636°	−113.829749°	NA	5.08	NA	NA	NA	0.77	24.99	28.04	NA
BLM-93F	40.784636°	−113.829749°	NA	5.08	NA	NA	NA	0.77	68.28	71.32	NA
Access Road‡	40.763160°	−113.895190°									
Rest Stop‡	40.741108°	−113.851304°									

* Casing height above surface is the average of field measurements (Table C2). Field measurements vary because of salt deposition/dissolution, the maximum range in casing height between measurements is 5.2 cm, while the mean range between measurement heights is 2.8 cm. † BLM-12 is on a roadway elevated above saline pan surface by *ca* 30 cm. ‡ Surface brine sample.

Table C2. Measured water depth at wells.

Well ID	Date (YYYY-MM-DD)	Time (hh:mm)	Casing top height above surface (cm)	Depth to water from casing top (cm)	Water level below surface (cm)
BLM-12	2017-09-14		52.1	110.6	58.5
BLM-12	2018-05-03		52	106.7	54.7
BLM-12	2018-08-06		50.0	109.4	59.4
BLM-12	2018-10-01	17:00	50.0	121.6	71.6
BLM-12	2019-05-01	13:00	49.3	82.9	33.6
BLM-12	2019-07-15		50.9	118.9	68.0
BLM-31	2018-10-01		41.9	127.4	85.5
BLM-31	2019-09-08		42.1	71.3	29.3
BLM-31	2020-09-19	16:10	41.1	107.9	66.8
BLM-34	2019-09-08		28.3	62.2	33.8
BLM-34	2020-06-04	morning	31.8	40.6	8.9
BLM-34	2020-09-19	16:30	29.9	97.5	67.7
BLM-34	2020-11-23	afternoon	29.9	102.1	72.2
BLM-34	2020-12-21	10:20	29.6	91.7	62.2
BLM-37	2019-05-01		50.3	45.2	−5.1
BLM-37	2019-09-08		47.9	57.6	9.8
BLM-37	2020-06-04	morning	52.1	55.8	3.7
BLM-37	2020-09-19	11:00	49.1	66.1	17.1
BLM-37	2020-11-23	11:00	48.5	81.4	32.9
BLM-37	2020-12-21	9:45	49.4	79.6	30.2
BLM-41	2018-10-01		19.1	77.4	58.4
BLM-41	2019-09-08		19.5	51.2	31.7
BLM-41	2020-09-19	15:45	17.4	65.4	48.0
BLM-43A	2020-12-21		21.3	75.3	53.9
BLM-45	2019-09-08		46.6	65.8	19.2
BLM-45	2020-09-19	15:00	49.1	66.1	17.1
BLM-45	2020-11-23	afternoon	49.1	93.0	43.9
BLM-45	2020-12-21		49.4	81.4	32.0
BLM-50A	2020-12-21		24.4	79.2	54.9
BLM-50B	2018-10-01		48.8	96.9	48.2
BLM-50B	2019-09-08		49.4	82.0	32.6
BLM-50B	2020-12-21		49.1	104.2	55.2
BLM-53	2020-12-21		27.4	104.2	76.8
BLM-53A	2020-12-21		74.4	60.7	−13.7
BLM-53B	2020-12-21		49.4	125.6	76.2
BLM-63	2020-12-21		26.5	133.8	107.3
BLM-64	2020-12-21		30.5	136.6	106.1
BLM-93	2017-06-08		94.5	97.2	2.7
BLM-93	2017-09-14		94.5	98.5	4.0
BLM-93	2018-05-03		94.5	96.5	2.0
BLM-93	2018-08-05		94.5	103.3	8.8
BLM-93	2018-10-01		94.5	110.9	16.5
BLM-93	2019-07-14		96.0	99.1	3.0
BLM-93	2019-09-08		97.5	99.4	1.8
BLM-93	2020-06-04	afternoon	99.1	96.5	−2.5
BLM-93	2020-09-19	12:30	96.9	110.0	13.1
BLM-93	2020-11-23	noon	96.3	127.7	31.4
BLM-93	2020-12-21	11:00	96.0	129.5	33.5
BLM-93A	2020-09-19	13:00	74.7	37.2	−37.5
BLM-93A	2020-11-23	afternoon	74.5	42.4	−32.2
BLM-93A	2020-12-21	11:00	74.4	45.3	−29.1
BLM-93C	2019-09-08		45.7	58.5	12.8
BLM-93C	2020-06-04	morning	50.9	50.9	0.0
BLM-93C	2020-09-19	13:00	48.5	64.6	16.2
BLM-93C	2020-11-23	afternoon	48.5	79.6*	31.1
BLM-93C	2020-12-21	11:00	47.2	75.9*	28.7

* Transducers removed before measuring water column height.

Table C3. Brine sample density, temperature, quasi-salinity and degree of halite saturation.

Site-ID	Date (YYYY-MM-DD)	Sample depth from casing top (cm)	Field density (g cm^{-3}) ± 0.001 g cm^{-3}	Field temp. (°C) ±0.2°C	Density at 30°C (g cm^{-3}) ±0.001 g cm^{-3}	Temp. *ca* 30°C (±0.2°C)	Quasi-salinity σ_{30} (kg m^{-3}) ±1 kg m^{-3}	Degree of halite saturation (kg m^{-3}) ±2 kg m^{-3}
Access road	2019-01-09	pond	1.206	7.0	1.198	30.5	203	−1
Access road	2019-05-01	pond	1.208	18.6	1.202	30.1	206	3
Access road	2020-01-29	pond	1.202	4.0	1.189	30.1	194	−6
BLM-12	2017-09-14		1.201	16.7	NA	NA	NA	−7
BLM-12	2019-05-01	114	1.203	14.4	1.196	30.4	200	−6
BLM-12	2019-05-01	80	1.203	14.4	1.196	29.8	200	−6
BLM-12	2019-05-01	pond	1.208	17.6	NA	NA	NA	NA
BLM-12	2019-07-14	114	1.200	23.5	1.196	30.4	201	−5
BLM-12	2019-07-14	80	1.200	23.5	1.196	30	201	−5
BLM-31	2019-09-08		1.185	26.7	1.183	30	187	−19
BLM-31	2020-09-19		1.184	27.0	1.182	30.2	187	−19
BLM-34	2019-09-08	140	1.196	25.7	1.195	30	199	−9
BLM-34	2020-06-04	140	1.195	24.7	1.195	30.3	199	−10
BLM-34	2020-06-04	100	1.194	28.5	NA	NA	NA	−10
BLM-34	2020-09-19	100	1.194	28.6	NA	NA	NA	−9
BLM-34	2020-09-19	140	1.195	28.7	1.194	30.2	199	−9
BLM-34	2020-11-23		1.205	10.8	1.196	30	200	−6
BLM-34	2020-12-21		1.203	5.85	1.196	30.1	200	−8
BLM-37	2019-05-01	156	NA	11.7	1.198	30.2	202	NA
BLM-37	2019-05-01	180	NA	11.7	1.199	30	203	NA
BLM-37	2019-05-01	pond	NA	NA	1.201	30.1	205	NA
BLM-37	2019-07-14	156	1.201	21.8	1.198	30.2	203	−9
BLM-37	2019-07-14	180	1.202	21.7	1.198	30	202	−9
BLM-37	2019-09-08	156	1.200	26.0	1.200	30.3	204	−9
BLM-37	2019-09-08	180	1.200	26.2	NA	NA	NA	−9
BLM-37	2020-06-04	156	1.190	28.6	1.199	30.2	203	−17
BLM-37	2020-06-04	180	1.191	27.8	NA	NA	NA	−17
BLM-37	2020-09-19	156	1.201	22.5	1.197	30.1	202	−9
BLM-37	2020-09-19	180	1.201	22.8	1.198	30.3	202	−9
BLM-37	2020-11-23	180	1.208	12.5	1.200	30.2	205	−6
BLM-37	2020-12-21		1.212	7.5	1.201	30.1	205	−3
BLM-41	2019-09-08		1.193	25.1	1.191	30.2	195	−14
BLM-41	2020-09-19		1.192	25.7	1.190	30.2	195	−15
BLM-43A	2020-12-21		1.211	6.9	1.200	30.1	205	1
BLM-45	2019-09-08	100	1.197	23.2	1.195	30.1	199	−13
BLM-45	2020-09-19	50	1.194	26.3	1.195	30.2	199	−15
BLM-45	2020-11-23		1.205	10.5	1.194	30.1	199	−9
BLM-45	2020-12-21		1.207	7.3	1.195	30.1	199	−8
BLM-50A	2020-12-21		1.200	10.0	1.189	30.1	194	−10
BLM-50B	2019-09-08		1.192	25.9	1.190	30.4	195	−12
BLM-53	2020-12-21		1.194	13.1	1.185	30.1	189	−16
BLM-53A	2020-12-21		1.110	10.5	1.103	30.1	107	−97
BLM-53B	2020-12-21		1.194	12.0	1.184	30.1	189	−16
BLM-63	2020-12-21		1.189	12.3	1.180	30.1	184	−21
BLM-64	2020-12-21		1.194	12.6	1.185	30.1	189	−16
BLM-93	2017-06-08		1.187	15.5	NA	NA	NA	−27
BLM-93	2017-09-14		1.187	16.8	NA	NA	NA	−26
BLM-93	2019-07-14	210	1.189	17	1.184	30	189	−24
BLM-93	2019-07-14	175	1.189	20.1	1.185	30	189	−23
BLM-93	2019-07-14	270	1.192	12.5	1.183	30	188	−22
BLM-93	2019-07-14	130	1.189	21.8	1.185	30	190	−21
BLM-93	2019-07-14	330	NA	11	1.185	30.2	189	NA
BLM-93	2019-09-08	330	1.186	24.3	1.184	30.3	188	−24

Table C3. (continued)

Site-ID	Date (YYYY-MM-DD)	Sample depth from casing top (cm)	Field density (g cm^{-3}) ± 0.001 g cm^{-3}	Field temp. (°C) ±0.2°C	Density at 30°C (g cm^{-3}) ±0.001 g cm^{-3}	Temp. *ca* 30°C (±0.2°C)	Quasi-salinity σ_{30} (kg m^{-3}) ±1 kg m^{-3}	Degree of halite saturation (kg m^{-3}) ±2 kg m^{-3}
BLM-93	2019-09-08	270	1.185	25.1	NA	NA	NA	−24
BLM-93	2019-09-08	130	1.185	26.4	1.183	30.4	188	−24
BLM-93	2020-06-04		1.185	29.2	1.184	30	188	−22
BLM-93	2020-09-19	330	1.184	26.5	1.183	30.2	187	−25
BLM-93	2020-09-19	270	1.185	25.1	1.184	30.3	188	−25
BLM-93	2020-09-19	210	1.184	25.8	1.182	30	187	−25
BLM-93	2020-09-19	130	1.185	24.8	1.183	30.2	188	−24
BLM-93	2020-09-19	175	1.185	25.5	1.183	30.3	187	−24
BLM-93	2020-11-23	330	1.194	9.1	NA	NA	NA	−21
BLM-93	2020-11-23	130	1.195	9.9	1.184	30.2	189	−20
BLM-93	2020-11-23	210	1.195	9.5	NA	NA	NA	−20
BLM-93	2020-12-21		1.198	7.8	1.188	30.1	192	−17
BLM-93A	2020-09-19		1.120	26.8	1.118	30.5	123	−83
BLM-93A	2020-11-23		1.127	8.7	1.118	30	123	−83
BLM-93A	2020-12-21		1.129	4.9	1.118	30.1	123	−81
BLM-93C	2019-09-08	50	1.207	25.1	1.204	30.2	209	−1
BLM-93C	2020-06-04		1.204	29.7	1.204	30.1	208	−1
BLM-93C	2020-09-19		1.205	29.1	1.204	30.2	209	−1
BLM-93C	2020-11-23		1.216	4.5	1.203	30.3	207	2
BLM-93C	2020-12-21		1.216	3.3	1.202	30.1	207	3
Rest Stop	2020-01-29	pond	1.202	3.0	1.169	30.1	173	−3

Where ρ_1 is the reference density to adjust the sample to [1.209 g cm^{-3} (BLM-93C density)], ρ_2 is the density of the well-water, h_2 is the height of the water level above a datum (sea-level used here) and z is the elevation (above the datum, sea-level) of the mid-point of the screened interval and h_1 is the equivalent head relative to the datum.

The brine density difference between BLM-93 and BLM-93C was fairly constant. This difference in hydraulic head between the wells varied throughout the year. The vertical flow gradients at the site of BLM-93 may depress summer groundwater temperatures at 1 m depth by 1 to 2°C. Groundwater at 1 m depth at BLM-93 was slightly cooler than other wells at the same depth during the summer. Brine extraction impacted water levels at BLM-34. Within days of the cessation of brine extraction, water levels at BLM-34 quickly rose by >10 cm (Fig. C2).

Quasi-salinity and degree of halite saturation calculated using methods outlined in Appendix D. Some samples were not measured in the field, so the calculation of halite saturation state at field conditions was not possible. Negative halite saturation indicates the sample was undersaturated. Samples collected from surface ponded water are described as 'pond' under sample depth, the sample depth of some samples was not precise and is not listed.

APPENDIX D. BRINE QUASI-SALINITY AND HALITE SATURATION METHODS AND DATA

This appendix outlines the methods and data used to calculate (1) quasi-salinity, (2) the relationship between density and total dissolved solids (TDS) for Bonneville Salt Flats' brines, (3) the empirical degree of halite saturation and (4) the effect of temperature changes on the degree of halite saturation.

QUASI-SALINITY CALCULATION

Many different methods have been used to calculate or approximate salinity (Anati, 1999). Quasi-salinity is calculated here by measuring

COLOR

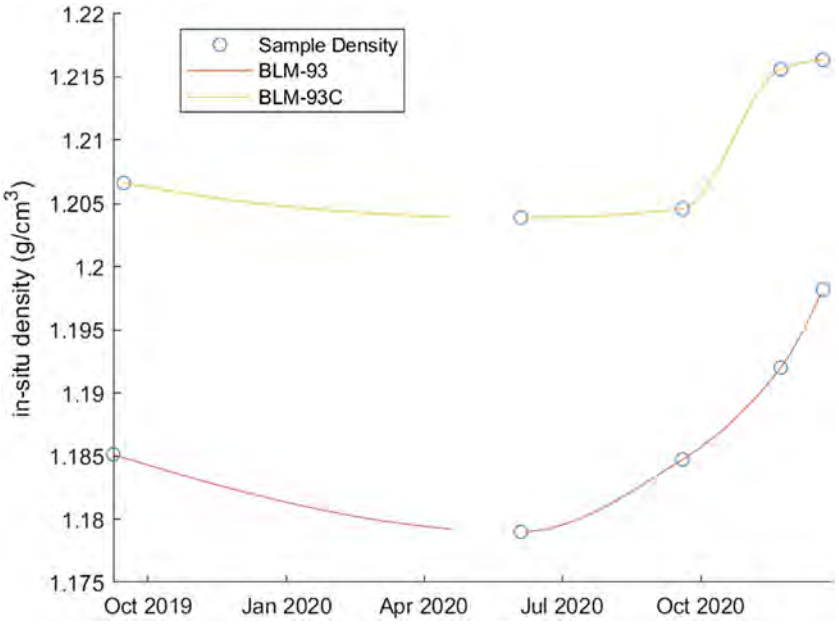

Fig. C1. Field density measurements and extrapolated *in-situ* density. Shape-filling cubic interpolation used to extrapolate data measurements. Note the long winter period with no density measurements.

COLOR

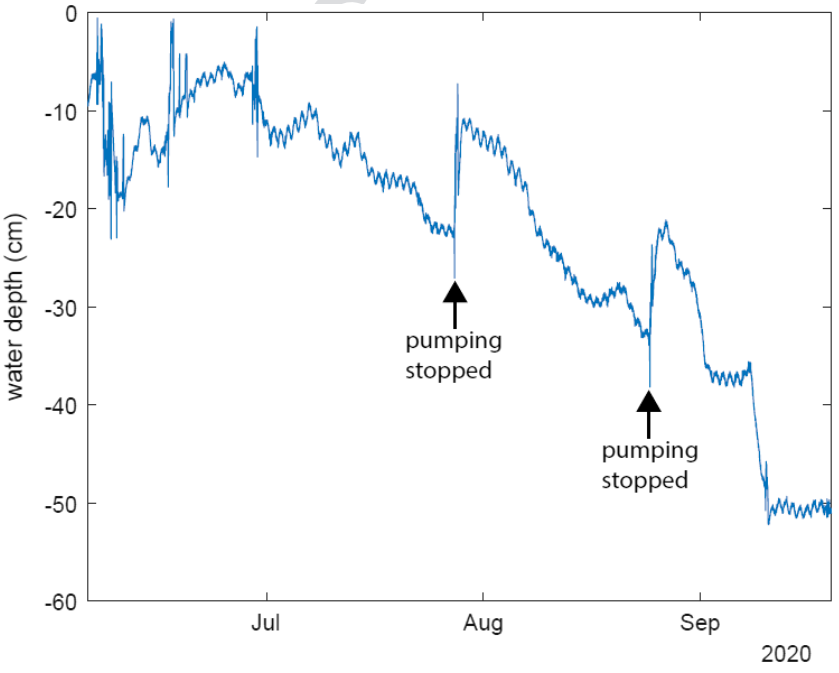

Fig. C2. Groundwater level at BLM-34, near the eastern edge of BSF, during the summer of 2020. Note the sharp jumps in groundwater level (black arrows), which are associated with cessation of brine extraction. The gradual decline in water level is associated with brine extraction, with evaporation playing a minor role in groundwater drawdown. The summer of 2020 was a very dry period and the sharp jumps in water level are not associated with meteoric precipitation.

sample density at a constant temperature. Density was measured with a Densito 30PX (Mettler Toledo, Columbus, Ohio, USA) with an accuracy of ±0.001 g cm^{-3} (1 kg m^{-3}) and ±0.2°C and a precision of 0.0001 g cm^{-3} (0.1 kg m^{-3}). This accuracy is higher than salinity measurements of these brines based upon total dissolved solids (with average charge balances of 7% and individual major ion reporting limits up to 2 g L^{-1}; Table D1). Quasi-salinity is an effective and inexpensive measurement of relative salinity within brines of similar composition. Quasi-salinity is calculated by subtracting the density of pure water (equation D1) at a reference temperature from the sample density at that same reference temperature (equation D2; Anati, 1999; Tanaka *et al.,* 2001; Gertman & Hecht, 2002; Sirota *et al.,* 2016).

$$\rho_{H2OT}\,(\mathrm{kg\,m^{-3}}) = \left(999.97495*\left(1-\left(\left(T-3.983035\right)^2\right)*\frac{T+301.797}{522528.9*(T+69.34881)}\right)\right) \quad \text{(D1)}$$

Where ρ_{H2O} is the density of pure water (kg m^{-3}) at temperature T (°C).

$$\sigma_{30}(\mathrm{kg\,m^{-3}}) = (\rho_{\mathrm{sample30}}(\mathrm{g\,cm^{-3}})*1000 - \rho_{H2O\,30}(\mathrm{kg\,m^{-3}})) \quad \text{(D2)}$$

where $\rho_{sample30}$ is the sample density at 30°C, $\rho_{H2O\ 30}$ is the density of pure water at 30°C and σ_{30} is the quasi-salinity at 30°C.

RELATIONSHIP BETWEEN SAMPLE DENSITY, QUASI-SALINITY AND TOTAL DISSOLVED SOLIDS

To confirm the effectiveness of quasi-salinity as a measure of brine composition, density data and TDS from a set of Bonneville Salt Flats brines were compared (Table 1; Fig. D1). Kipnis *et al.* (2020) Bonneville Salt Flats brine chemistry data was used to identify a linear fit between total dissolved solids, sample density and quasi-salinity (equations D4 and D5, Fig. D1, Table D1). Brine densities were measured at room temperature (21.6 to 24.5°C, mean temperature 22.5°C). Brine densities at other temperatures were not available. Sample density ranged from 1.092 to 1.223 g cm^{-3}. To partially correct for the effect of temperature on density, sample

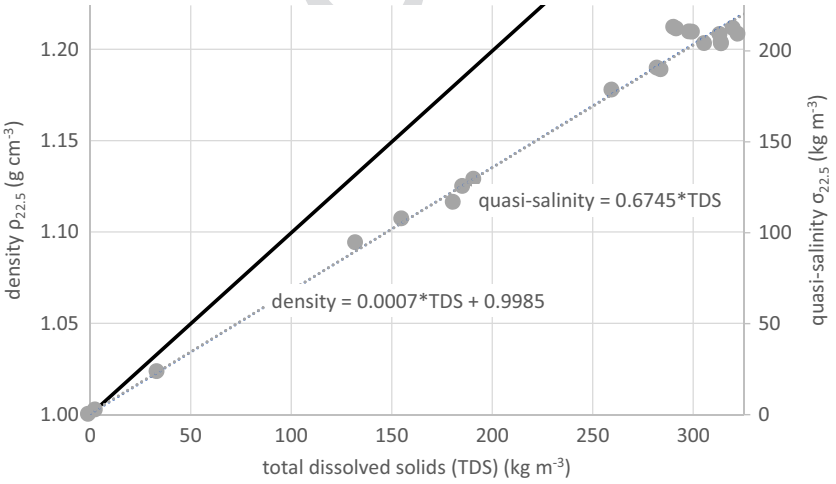

Fig. D1. Linear relationship between total dissolved solids, sample density adjusted to mean temperature of 22.5°C and quasi-salinity of samples at 22.5°C of Bonneville Salt Flats brines using data from Table D1 (grey circles). Black line shows parity between quasi-salinity and salinity from total dissolved solids, demonstrating that these values are not directly comparable. Deviation from the linear relationship between TDS and sample density is related to variation in sample composition. Above a TDS of 100 kg m^{-3}, the predicted TDS from sample density is within 10% of actual sample TDS. Accuracy decreases with lower salinity. Linear fits between TDS and sample density and quasi-salinity were used to determine the empirical relationships in equations D4 and D5. The relationship between density and TDS for BSF brines was previosly calculated and shown in fig. 45 of Lines (1979) as TDS = (ρ_{20} – 1.000)*1590, where ρ_{20} is the sample's density at 20°C. For the data in Table D1 (shown here), TDS is calculated as *ca* TDS = (ρ_{20} – 1.000)* 1470.1. The difference in equations indicates a change in measured TDS values between datasets.

COLOR

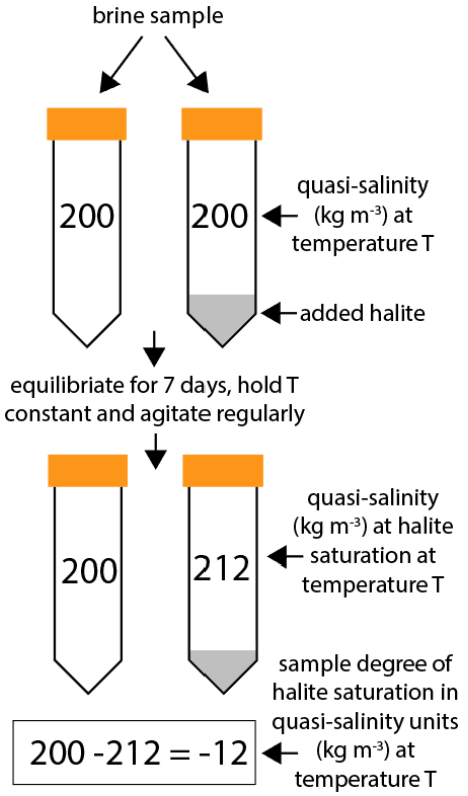

Fig. D2. Schematic representation of methodology used to calculate the empirical degree of halite saturation in quasi-salinity units. Sample was split, one part had halite added to it and was allowed to equilibrate with the halite, bringing it to halite saturation. The difference in quasi-salinity units between the two sample splits was used to calculate the empirical degree of halite saturation. Method and figure adapted from Sirota *et al.* (2016). The convention used in this paper reports halite undersaturated brines with negative values.

density was corrected to the mean temperature of 22.5°C (equation D3).

$$\rho_{\text{sample } T2} = \rho_{\text{sample } T1} - \rho_{H20\,T1} + \rho_{H2O\,T2} \quad \text{(D3)}$$

where $\rho_{\text{sample T2}}$ is the sample density corrected to temperature 2, $\rho_{\text{sample T1}}$ is sample density measured at temperature 1 and $\rho_{\text{H20 T1}}$ and $\rho_{\text{H20 T2}}$ are the density of pure water at temperatures 1 and 2 (calculated with equation D1). This correction is inappropriate for temperature corrections > 2.5°C and high precision measurements.

$$\text{Total Dissolved Solids } (\text{g L}^{-1} \text{ or kg m}^{-3}) = 1{,}455.6 * \rho_{\text{sample } 22.5} - 1{,}449.5 \quad \text{(D4)}$$

$$\text{Total Dissolved Solids } (\text{g L}^{-1} \text{ or kg m}^{-3}) = 0.6668 * \sigma_{22.5} + 3.0377 \quad \text{(D5)}$$

where $\rho_{\text{sample } 22.5}$ is sample density at 22.5°C (equation D3) and $\sigma_{22.5}$ is sample quasi-salinity at 22.5°C. The standard deviation of sample total dissolved solids determined using this technique is 10.5 g l^{-1} TDS, due in part to variable sample chemistry. Equations D4 and D5 are specific to Bonneville Salt Flats brines.

EMPIRICAL DEGREE OF HALITE SATURATION

Sirota *et al.* (2016) calculated the degree of halite saturation with high precision in brines by measuring the difference in density (and quasi-salinity) between a sample and the same sample that had been equilibrated with reagent grade halite (Equation D6). Samples were filtered and then spiked with 10 g of halite for a 50 ml volume, regularly agitated and held at sample collection temperature for a week and then measured with high precision (Fig. D2).

$$\text{Degree of halite saturation } (\text{kg m}^{-3}) = \sigma_{T1} - \sigma_{\text{halite}T1} \quad \text{(D-6)}$$

The empirical degree of halite saturation shown in kg m^{-3} (quasi-salinity; Fig. D2). σ_{T1} is the sample quasi-salinity at field temperatures and σ_{haliteT1} is the calculated or measured quasi-salinity of the sample at halite saturation at field temperatures (Table C3). Positive values are oversaturated, while negative values indicate the sample was undersaturated at field conditions.

Because field temperatures could not be consistently replicated with available equipment, these methods were adapted to measure the degree of halite saturation in Bonneville Salt Flats samples. Equipment includes a digital hydrometer (Densito 30PX), Ecocell 55 drying oven (MMM Group, Munich, Germany) and refrigerator. Unaltered samples and samples with added halite were held for a week at a constant temperature, regularly agitated and then measured. Samples were measured at heated (*ca* 30°C), room (*ca* 15 to 20°C) and cooled (*ca* 5°C) temperatures (Table D2). Additional measurements at other temperatures were made for some samples.

COLOR

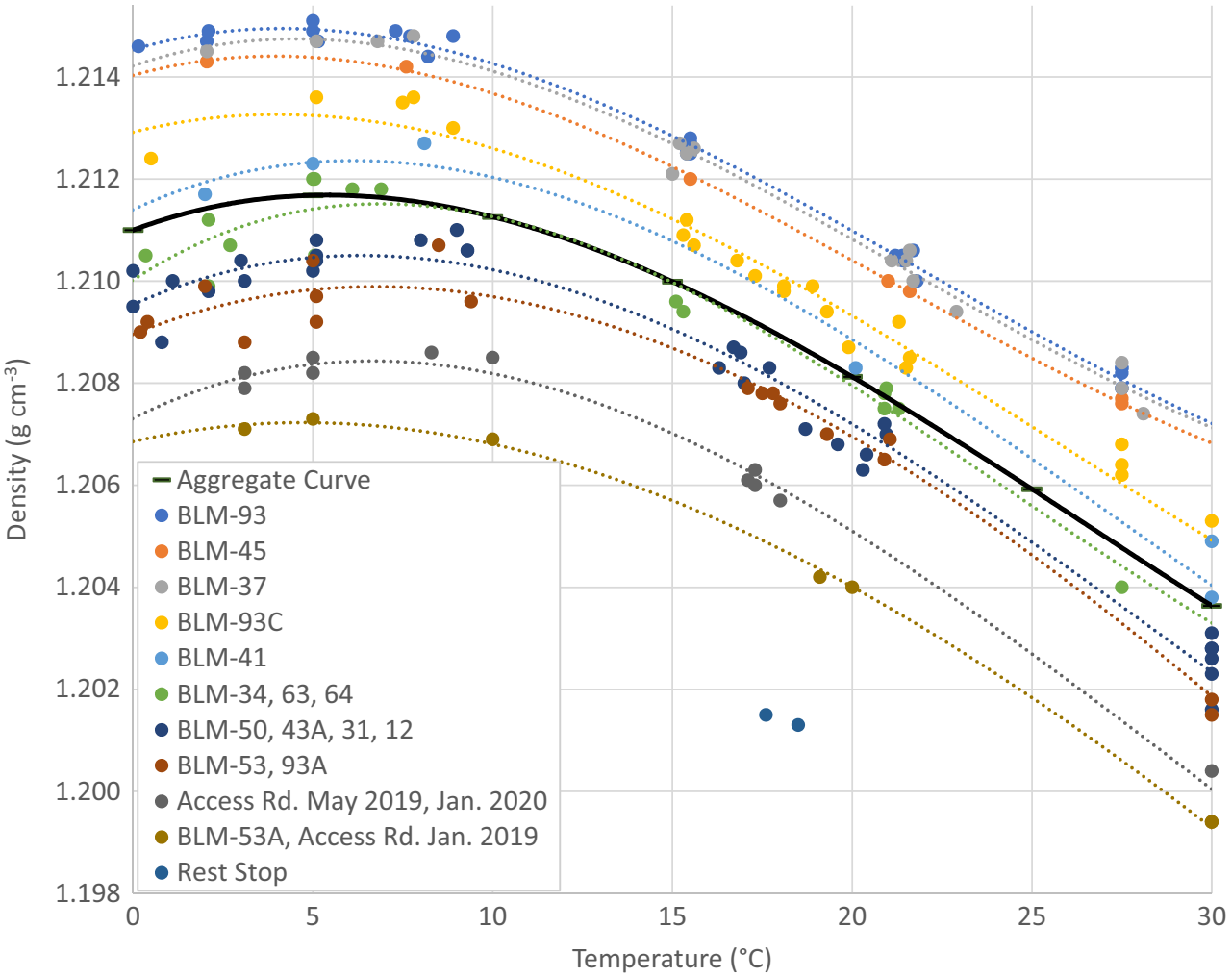

Fig. D3. Samples' densities at different temperatures when saturated with halite (Table D2). Note the different brine types, with BLM-93 at the top likely being the most potassium and magnesium rich. The polynomial equations of the trendlines (Table D3) were used to create an aggregate saturated density curve and equation (thick black line). This generalized aggregate equation was adjusted for each brine type by changing the constant added to the curve (Table D4) and was applied to the dataset to determine sample densities at halite saturation at different temperatures with an accuracy of ±1 kg m^{-3} or 0.001 g cm^{-3}. The density of brine samples at halite saturation from the same well did not change markedly between sample periods.

Measurements of a sample's density at halite saturation at different temperatures were used to create a third-degree polynomial fit for the data (Table D3; Fig. D3; Equation D7). This equation is applicable to calculate the density of samples at temperatures between 0-30°C. To improve the generalizability of this equation to BSF brines of differing compositions (σ_{30} of 200 to 211 kg m^{-3} at halite saturation) an aggregate halite-saturated density polynomial equation was created by averaging the coefficients for each brine type. The input of the halite-saturated sample density at 0°C for each brine type was calibrated such that the model residual was less than measurement accuracy (0.001 g cm^{-3} or 1 kg m^{-3}; Tables D3 and D4).

$$\rho_{\text{sample+halite}T} = A*T^3 + B*T^2 + C*T + \rho_0 \quad \text{(D-7)}$$

where $\rho_{\text{sample+halite}}$ is the sample density (g cm^{-3}) at halite saturation at temperature T (°C). T is the sample temperature at field conditions. A, B, and C are coefficients (Table D3) and ρ_0 is the brine density at 0°C (Tables D3 and D4).

The density of samples with added halite were used to identify general changes in brine

COLOR

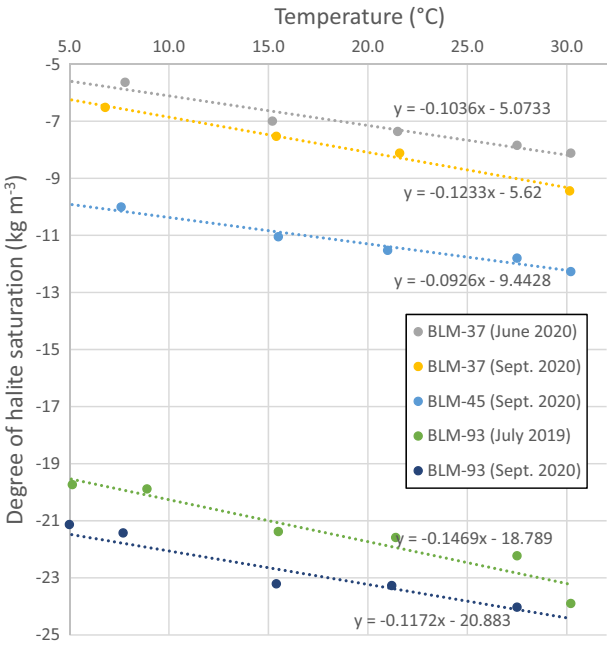

Fig. D4. Change in degree of undersaturation at different temperatures (wells near the centre of BSF). The slopes of the fit lines are aggregated in Table D5. Degree of halite undersaturation and halite solubility decreases with decreasing temperature.

composition. Samples from wells with groundwaters with historically higher potassium and magnesium concentrations had higher densities at halite saturation while samples with historically lower potassium and magnesium concentrations had lower densities at halite saturation (Table D4; Turk, 1973; Lines, 1979).

IMPACT OF CHANGING TEMPERATURE ON SAMPLE HALITE SATURATION STATE AND HALITE SOLUBILITY

The effect of temperature on halite saturation state was used to quantify the degree that temperature could contribute to daily or seasonal changes in quasi-salinity. Brine's degree of halite saturation at different temperatures were plotted (using data from Table D2; Fig. D4). The slope for the effect of temperature upon degree of halite saturation from different samples was aggregated (Table D5). This slope demonstrated the effect of temperature on brine quasi-salinity and the comparable change in total dissolved solids (Table D5). The effect of seasonal changes in groundwater temperature (*ca* 10°C) upon quasi-salinity would be relatively small (1.2 kg m^{-3}). This value is similar to previously calculated increases in halite solubility of pure halite of 1.2 g kg^{-1} H_2O with a 10°C temperature change (+0.14 moles NaCl/1000 moles H_20 per °C in a NaCl-H_2O system; Braitsch, 1971).

Table D1. Physical properties and total dissolved solids of groundwater samples from different depths beneath the Bonneville Salt Flats. Sample density and temperature were measured in the lab. Data from Kipnis *et al.* (2020). Samples were analysed at American West Analytical Laboratories with ICP-OES/IC, with individual ion reporting limits up to 2 g l^{-1}. The well parameters for BLM sites are described in Table C1. Samples denoted with a 'D' are from excavated pits.

Site ID	Sample Date (YYYY-MM-DD)	Latitude	Longitude	Density (g cm^{-3}) ±0.001 g cm^{-3}	Temp. (°C) ±0.2°C	TDS (g l^{-1}) or (kg m^{-3}) ±>2 g l^{-1}
BLM-6	6/10/2016	40.73911°	−113.82252°	1.202	21.7	307
BLM-12	6/10/2016	40.74105°	−113.91280°	1.202	21.9	315
BLM-12	9/25/2016	40.74105°	−113.91280°	1.201	24.5	315
BLM-17	6/9/2016	40.77688°	−113.91224°	1.176	21.9	260
BLM-93	6/8/2017	40.78464°	−113.82975°	1.188	23.9	283
BLM-93	9/25/2016	40.78464°	−113.82975°	1.187	24.4	285
BLM-93A	6/8/2017	40.78464°	−113.82975°	1.123	23.7	186
BLM-93C	6/8/2017	40.78464°	−113.82975°	1.208	23.6	299
BLM-93D	2016-06-09	40.78464°	−113.82975°	1.114	21.8	182
BLM-93D	2016-09-25	40.78464°	−113.82975°	1.127	21.8	192
BLM-93E	2016-09-25	40.78464°	−113.82975°	1.092	23.9	133
BLM-93F	2016-09-25	40.78464°	−113.82975°	1.105	24.3	156
D-12B	2016-09-07	40.84172°	−113.76877°	1.211	21.7	291
D-33	2016-09-06	40.80069°	−113.84770°	1.223	21.6	324
D-35	2016-09-06	40.78422°	−113.82946°	1.210	21.6	321
D-45	2016-09-08	40.74526°	−113.86098°	1.210	21.7	293
D-54	2016-09-08	40.75630°	−113.87336°	1.207	21.7	323
D-56	2016-09-07	40.76300°	−113.83093°	1.208	21.9	300
D-56*	2016-09-07	40.76300°	−113.83093°	1.021	21.2	34
D-56*	2016-09-07	40.76300°	−113.83093°	1.000	21.5	3
D-67B	2016-09-05	40.82306°	−113.79781°	1.207	21.7	314

* Two samples from D56 were gravimetrically diluted by 10 and 100x and then measured for sample density.

Table D2. Calculated degree of sample halite undersaturation of Bonneville Salt Flat brines at different temperatures using the methods of Sirota *et al.* (2016). See Table C3 for field measurements of sample density, temperature and calculated degree of halite saturation at field conditions. Positive values for degree of halite saturation indicate sample was oversaturated. The standard deviation of the residual of the aggregate model (Tables D3 and D4) was 0.6 quasi-salinity units (within measurement error of 1 kg m^{-3}). Not all samples had paired measurements of the original sample at the same temperature. To improve the model the sample density at halite saturation is shown with the greatest precision available. Negative values for degree of halite saturation indicate the sample is undersaturated with respect to halite.

Sample/Well ID	Sample date (YYYY-MM-DD)	Depth (cm)	Temp. (°C) ±0.2°C	Sample density (g cm^{-3}) ±0.001 g cm^{-3}	Sample density at halite saturation (g cm^{-3}) ±0.001 g cm^{-3} (measured)	Sample density at halite saturation (g m^{-3}) ±0.001 g cm^{-3} (modelled)	Model residual (kg m^{-3}) quasi-salinity	Degree of halite saturation (kg m^{-3}) quasi-salinity ± 2 kg m^{-3}
Access Road	2019-01-09		5.0	1.205	1.2073	1.2075	0.2	−2
Access Road	2019-01-09		10.0	1.207	1.2069	1.2071	0.2	0
Access Road	2019-01-09		34.0	NA	1.1970	1.1978	0.8	NA
Access Road	2019-01-09		32.0	NA	1.1981	1.1986	0.5	NA
Access Road	2019-01-09		30.0	NA	1.1994	1.1995	0.1	NA
Access Road	2019-01-09		20.0	NA	1.2040	1.2040	0.0	NA
Access Road	2019-01-09		19.1	NA	1.2042	1.2044	0.2	NA
Access Road	2019-01-09		3.1	NA	1.2071	1.2074	0.3	NA
Access Road	2019-01-09		3.1	NA	1.2079	1.2079	0.0	NA
Access Road	2019-01-09		5.0	NA	1.2082	1.2080	−0.2	NA
Access Road	2019-01-09		10.0	NA	1.2085	1.2076	−0.9	NA
Access Road	2019-01-09		18.4	NA	1.206	1.2051	−0.9	NA
Access Road	2019-01-09		17.3	NA	1.2063	1.2055	−0.8	NA
Access Road	2019-01-09		30.0	NA	1.2004	1.1999	−0.5	NA
Access Road	2019-01-09		32.0	NA	1.1992	1.1991	−0.1	NA
Access Road	2019-01-09		34.0	NA	1.1980	1.1982	0.2	NA
Access Road	2020-01-29		3.1	NA	1.2082	1.2079	−0.3	NA
Access Road	2020-01-29		5.0	NA	1.2085	1.2080	−0.5	NA
Access Road	2020-01-29		8.3	NA	1.2086	1.2078	−0.8	NA
Access Road	2020-01-29		17.1	NA	1.2061	1.2056	−0.5	NA
Access Road	2020-01-29		18.0	NA	1.2057	1.2052	−0.5	NA
Access Road	2020-01-29		30.1	NA	1.2001	1.1999	−0.2	NA
Access Road	2020-01-29		32.0	NA	1.1988	1.1991	0.3	NA
Access Road	2020-01-29		33.9	NA	1.1976	1.1983	0.7	NA
BLM-12	2019-05-01	80	16.3	NA	1.2083	1.2081	−0.2	NA
BLM-12	2019-05-01	80	30.0	NA	1.2031	1.2022	−0.9	NA
BLM-12	2019-05-01	80	32.0	NA	1.2018	1.2013	−0.5	NA
BLM-12	2019-05-01	80	34.0	NA	1.2005	1.2005	0.0	NA
BLM-12	2019-05-01		17.0	NA	1.2080	1.2079	−0.1	NA
BLM-12	2019-07-15	114	30.0	NA	1.2028	1.2022	−0.6	NA
BLM-12	2019-07-15	114	32.0	NA	1.2015	1.2013	−0.2	NA
BLM-12	2019-07-15	114	34.0	NA	1.200	1.2005	0.5	NA
BLM-12	2019-07-15		20.4	NA	1.2066	1.2065	−0.1	NA

Table D2. (continued)

Sample/Well ID	Sample date (YYYY-MM-DD)	Depth (cm)	Temp. (°C) ±0.2°C	Sample density (g cm^{-3}) ±0.001 g cm^{-3}	Sample density at halite saturation (g cm^{-3}) ±0.001 g cm^{-3} (measured)	Sample density at halite saturation (g m^{-3}) ±0.001 g cm^{-3} (modelled)	Model residual (kg m^{-3}) quasi-salinity	Degree of halite saturation (kg m^{-3}) quasi-salinity ± 2 kg m^{-3}
BLM-31	2020-09-19		34.0	1.176	1.2001	1.2005	0.4	−24
BLM-31	2020-09-19		30.0	1.182	1.2026	1.2022	−0.4	−20
BLM-31	2020-09-19		1.1	1.190	1.2100	1.2098	−0.2	−20
BLM-31	2020-09-19		3.0	1.190	1.2104	1.2101	−0.3	−20
BLM-31	2020-09-19		0.0	1.190	1.2102	1.2096	−0.6	−19
BLM-31	2020-09-19		5.1	1.191	1.2108	1.2103	−0.5	−20
BLM-31	2020-09-19		9.0	1.191	1.2110	1.2100	−1.0	−19
BLM-31	2020-09-19		16.9	NA	1.2086	1.2079	−0.7	NA
BLM-31	2020-09-19		32.0	NA	1.2013	1.2013	0.0	NA
BLM-34	2020-06-04		27.5	1.196	1.2040	1.2041	0.1	−8
BLM-34	2020-06-04		20.9	1.200	1.2075	1.2071	−0.4	−8
BLM-34	2020-06-04		15.3	1.202	1.2094	1.2092	−0.2	−7
BLM-34	2020-06-04		5.1	1.203	1.2120	1.2110	−1.0	−8
BLM-34	2020-06-04		6.9	1.205	1.2118	1.2110	−0.8	−6
BLM-34	2020-06-04		2.1	1.205	1.2112	1.2108	−0.4	−6
BLM-34	2020-09-19		27.5	1.196	1.2050	1.2041	−0.9	−8
BLM-34	2020-09-19		21.3	1.200	1.2075	1.2069	−0.6	−7
BLM-34	2020-09-19		2.7	1.202	1.2107	1.2109	0.2	−9
BLM-34	2020-09-19		15.1	1.202	1.2096	1.2093	−0.3	−7
BLM-34	2020-09-19		5.0	1.203	1.212	1.2110	−1.0	−8
BLM-34	2020-09-19		0.4	1.203	1.2105	1.2104	−0.1	−8
BLM-34	2020-09-19		6.1	1.206	1.2118	1.2110	−0.8	−6
BLM-37	2019-05-01	156	30.2	1.198	1.2068	1.2066	−0.2	−9
BLM-37	2019-05-01	156	28.1	1.199	1.2074	1.2076	0.2	−9
BLM-37	2019-05-01	156	22.9	1.202	1.2094	1.2099	0.5	−8
BLM-37	2019-05-01	156	21.7	1.202	1.2100	1.2105	0.5	−8
BLM-37	2019-05-01	156	15.0	1.205	1.2121	1.2131	1.0	−8
BLM-37	2019-05-01	156	5.1	1.209	1.2147	1.2148	0.1	−6
BLM-37	2019-05-01	156	2.1	1.208	1.2145	1.2145	0.0	−7
BLM-37	2019-05-01	180	30.1	1.199	1.2067	1.2067	0.0	−8
BLM-37	2019-07-14	156	27.5	1.199	1.2084	1.2078	−0.6	−8
BLM-37	2019-07-14	156	21.1	1.203	1.2104	1.2107	0.3	−8
BLM-37	2019-07-14	156	15.6	1.205	1.2126	1.2129	0.3	−8
BLM-37	2020-06-04		30.2	1.199	1.2074	1.2066	−0.8	−8
BLM-37	2020-06-04		27.5	1.200	1.2079	1.2078	−0.1	−8
BLM-37	2020-06-04		21.5	1.203	1.2104	1.2106	0.2	−7
BLM-37	2020-06-04		15.2	1.206	1.2127	1.2130	0.3	−7

Table D2. (continued)

Sample/Well ID	Sample date (YYYY-MM-DD)	Depth (cm)	Temp. (°C) ±0.2°C	Sample density (g cm^{-3}) ±0.001 g cm^{-3}	Sample density at halite saturation (g cm^{-3}) ±0.001 g cm^{-3} (measured)	Sample density at halite saturation (g m^{-3}) ±0.001 g cm^{-3} (modelled)	Model residual (kg m^{-3}) quasi-salinity	Degree of halite saturation (kg m^{-3}) quasi-salinity ± 2 kg m^{-3}
BLM-37	2020-06-04		7.8	1.209	1.2148	1.2146	−0.2	−6
BLM-37	2020-09-19	156	30.2	1.197	1.2074	1.2066	−0.8	−9
BLM-37	2020-09-19	156	21.6	1.202	1.2106	1.2105	−0.1	−8
BLM-37	2020-09-19	156	15.4	1.205	1.2125	1.2129	0.4	−8
BLM-37	2020-09-19	156	6.8	1.208	1.2147	1.2147	0.0	−7
BLM-41	2019-09-08		30.0	NA	1.2038	1.2040	0.2	NA
BLM-41	2019-09-08		32.0	NA	1.2025	1.2032	0.7	NA
BLM-41	2019-09-08		33.9	NA	1.2014	1.2024	1.0	NA
BLM-41	2020-09-19		34.0	1.188	1.2026	1.2023	−0.3	−15
BLM-41	2020-09-19		31.9	1.189	1.2037	1.2032	−0.5	−14
BLM-41	2020-09-19		30.0	1.190	1.2049	1.2040	−0.9	−14
BLM-41	2020-09-19		-0.2	NA	1.2114	1.2113	−0.1	NA
BLM-41	2020-09-19		2.0	NA	1.2117	1.2118	0.1	NA
BLM-41	2020-09-19		5.0	NA	1.2123	1.2121	−0.2	NA
BLM-41	2020-09-19		8.1	NA	1.2127	1.2119	−0.8	NA
BLM-41	2020-09-19		20.1	NA	1.2083	1.2085	0.2	NA
BLM-43A	2020-12-21		30.2	1.200	1.2028	1.2021	−0.7	−2
BLM-43A	2020-12-21		21.0	1.206	1.2070	1.2063	−0.7	−1
BLM-43A	2020-12-21		3.1	NA	1.2100	1.2101	0.1	NA
BLM-43A	2020-12-21		5.1	NA	1.2104	1.2103	−0.1	NA
BLM-43A	2020-12-21		9.3	NA	1.2106	1.2099	−0.7	NA
BLM-43A	2020-12-21		16.7	NA	1.2087	1.2080	−0.7	NA
BLM-43A	2020-12-21		17.7	NA	1.2083	1.2076	−0.7	NA
BLM-43A	2020-12-21		30.0	NA	1.2028	1.2022	−0.6	NA
BLM-43A	2020-12-21		32.0	NA	1.2014	1.2013	−0.1	NA
BLM-43A	2020-12-21		34.0	NA	1.2001	1.2005	0.4	NA
BLM-45	2019-09-08		27.5	1.196	1.2077	1.2080	0.3	−12
BLM-45	2019-09-08		21.6	1.199	1.2098	1.2107	0.9	−12
BLM-45	2019-09-09		30.2	1.195	1.2069	1.2068	−0.1	−12
BLM-45	2020-09-19		30.2	1.195	1.2066	1.2068	0.2	−12
BLM-45	2020-09-19		27.5	1.196	1.2076	1.2080	0.4	−12
BLM-45	2020-09-19		21.0	1.199	1.2100	1.2109	0.9	−12
BLM-45	2020-09-19		15.5	1.202	1.2120	1.2130	1.0	−11
BLM-45	2020-09-19		7.6	1.205	1.2142	1.2148	0.6	−10
BLM-45	2020-09-19		2.1	NA	1.2143	1.2146	0.3	NA
BLM-50A	2020-12-21		30.2	1.189	1.2030	1.2021	−0.9	−13
BLM-50A	2020-12-21		20.9	1.194	1.2072	1.2063	−0.9	−12

Table D2. (continued)

Sample/Well ID	Sample date (YYYY-MM-DD)	Depth (cm)	Temp. (°C) ±0.2°C	Sample density (g cm^{-3}) ±0.001 g cm^{-3}	Sample density at halite saturation (g cm^{-3}) ±0.001 g cm^{-3} (measured)	Sample density at halite saturation (g m^{-3}) ±0.001 g cm^{-3} (modelled)	Model residual (kg m^{-3}) quasi-salinity	Degree of halite saturation (kg m^{-3}) quasi-salinity ± 2 kg m^{-3}
BLM-50A	2020-12-21		0.8	1.197	1.2088	1.2098	1.0	−12
BLM-50A	2020-12-21		5.0	NA	1.2102	1.2103	0.1	NA
BLM-50A	2020-12-21		9.3	NA	1.2106	1.2099	−0.7	NA
BLM-50A	2020-12-21		20.3	NA	1.2063	1.2066	0.3	NA
BLM-50A	2020-12-21		30.0	NA	1.2023	1.2022	−0.1	NA
BLM-50A	2020-12-21		32.0	NA	1.2010	1.2013	0.3	NA
BLM-50A	2020-12-21		34.0	NA	1.1999	1.2005	0.6	NA
BLM-50B	2019-09-08		0.0	NA	1.2095	1.2096	0.1	NA
BLM-50B	2019-09-08		2.1	NA	1.2098	1.2100	0.2	NA
BLM-50B	2019-09-08		5.1	NA	1.2105	1.2103	−0.2	NA
BLM-50B	2019-09-08		8.0	NA	1.2108	1.2101	−0.7	NA
BLM-50B	2019-09-08		18.7	NA	1.2071	1.2072	0.1	NA
BLM-50B	2019-09-08		19.6	NA	1.2068	1.2069	0.1	NA
BLM-50B	2019-09-08		30.0	NA	1.2016	1.2022	0.6	NA
BLM-50B	2019-09-08		32.0	NA	1.2003	1.2013	1.0	NA
BLM-53	2020-12-21		30.2	1.185	1.2028	1.2026	−0.2	−18
BLM-53	2020-12-21		21.1	1.190	1.2069	1.2067	−0.2	−17
BLM-53	2020-12-21		2.0	NA	1.2099	1.2105	0.6	NA
BLM-53	2020-12-21		5.0	NA	1.2104	1.2107	0.3	NA
BLM-53	2020-12-21		8.5	NA	1.2107	1.2105	−0.2	NA
BLM-53	2020-12-21		17.8	NA	1.2078	1.2081	0.3	NA
BLM-53	2020-12-21		19.3	NA	1.2070	1.2075	0.5	NA
BLM-53A	2020-12-21		33.9	NA	1.1971	1.1978	0.7	NA
BLM-53A	2020-12-21		32.0	NA	1.1982	1.1986	0.4	NA
BLM-53A	2020-12-21		30.0	NA	1.1994	1.1995	0.1	NA
BLM-53B	2020-12-21		30.2	1.184	1.2025	1.2016	−0.9	−17
BLM-53B	2020-12-21		20.9	1.190	1.2065	1.2058	−0.7	−16
BLM-53B	2020-12-21		0.4	1.192	1.2092	1.2092	0.0	−18
BLM-53B	2020-12-21		5.1	1.193	1.2097	1.2097	0.0	−17
BLM-53B	2020-12-21		0.2	NA	1.2090	1.2091	0.1	NA
BLM-53B	2020-12-21		3.1	NA	1.2088	1.2096	0.8	NA
BLM-53B	2020-12-21		5.1	NA	1.2092	1.2097	0.5	NA
BLM-53B	2020-12-21		9.4	NA	1.2096	1.2094	−0.2	NA
BLM-53B	2020-12-21		17.1	NA	1.2079	1.2073	−0.6	NA
BLM-53B	2020-12-21		18.0	NA	1.2076	1.2070	−0.6	NA
BLM-53B	2020-12-21		30.0	NA	1.2018	1.2017	−0.1	NA
BLM-53B	2020-12-21		31.9	NA	1.2005	1.2009	0.4	NA

Table D2. (continued)

Sample/Well ID	Sample date (YYYY-MM-DD)	Depth (cm)	Temp. (°C) ±0.2°C	Sample density (g cm^{-3}) ±0.001 g cm^{-3}	Sample density at halite saturation (g cm^{-3}) ±0.001 g cm^{-3} (measured)	Sample density at halite saturation (g m^{-3}) ±0.001 g cm^{-3} (modelled)	Model residual (kg m^{-3}) quasi-salinity	Degree of halite saturation (kg m^{-3}) quasi-salinity ± 2 kg m^{-3}
BLM-53B	2020-12-21		34.1	NA	1.1995	1.1999	0.4	NA
BLM-63	2020-12-21		21.0	1.185	1.2079	1.2071	−0.8	−22
BLM-64	2020-12-21		30.2	1.185	1.2034	1.2029	−0.5	−18
BLM-64	2020-12-21		20.9	1.190	1.2078	1.2071	−0.7	−17
BLM-64	2020-12-21		2.1	1.193	1.2099	1.2108	0.9	−18
BLM-64	2020-12-21		5.1	1.194	1.2105	1.2110	0.5	−17
BLM-93	2019-07-14	130	30.2	1.183	1.2072	1.2070	−0.2	−24
BLM-93	2019-07-14	130	27.5	1.186	1.2079	1.2082	0.3	−22
BLM-93	2019-07-14	130	21.4	1.189	1.2105	1.2110	0.5	−22
BLM-93	2019-07-14	130	15.5	1.192	1.2128	1.2133	0.5	−21
BLM-93	2019-07-14	130	8.9	1.195	1.2148	1.2149	0.1	−20
BLM-93	2019-07-14	130	5.2	1.195	1.2147	1.2151	0.4	−20
BLM-93	2019-07-14	130	30.2	NA	1.2072	1.2070	−0.2	NA
BLM-93	2019-07-14	330	30.2	1.185	1.2069	1.2070	0.1	−22
BLM-93	2019-07-14	330	27.5	1.186	1.2083	1.2082	−0.1	−23
BLM-93	2019-07-14	330	21.7	1.189	1.2106	1.2109	0.3	−22
BLM-93	2019-07-14	330	15.5	1.191	1.2125	1.2133	0.8	−22
BLM-93	2020-06-04		30.2	1.185	1.2072	1.2070	−0.2	−22
BLM-93	2020-06-04		27.5	1.185	1.2083	1.2082	−0.1	−23
BLM-93	2020-06-04		21.4	1.188	1.2104	1.2110	0.6	−23
BLM-93	2020-06-04		15.4	1.191	1.2126	1.2133	0.7	−23
BLM-93	2020-06-04		8.2	1.194	1.2144	1.2150	0.6	−21
BLM-93	2020-09-19	130	27.5	1.184	1.2082	1.2082	0.0	−24
BLM-93	2020-09-19	130	21.2	1.188	1.2105	1.2111	0.6	−23
BLM-93	2020-09-19	130	15.4	1.190	1.2125	1.2133	0.8	−23
BLM-93	2020-09-19	130	7.7	1.194	1.2148	1.2150	0.2	−21
BLM-93	2020-09-19	130	5.0	1.194	1.2149	1.2151	0.2	−21
BLM-93	2020-09-19	330	30.2	1.183	1.2071	1.2070	−0.1	−24
BLM-93	2020-09-19	330	27.5	1.185	1.2079	1.2082	0.3	−24
BLM-93	2020-09-19	330	21.8	1.187	1.2100	1.2108	0.8	−24
BLM-93	2020-09-19	330	15.5	1.190	1.2127	1.2133	0.6	−23
BLM-93	2020-09-19	330	7.3	1.193	1.2149	1.2151	0.2	−22
BLM-93	2020-09-19	330	5.0	1.194	1.2151	1.2151	0.0	−21
BLM-93	2020-09-19	130	2.1	1.193	1.2147	1.2149	0.2	−21
BLM-93	2020-09-19	330	0.2	1.193	1.2146	1.2145	−0.1	−21
BLM-93	2020-09-19	330	2.1	1.194	1.2149	1.2149	0.0	−21
BLM-93A	2020-09-19		30.1	1.118	1.2010	1.2017	0.7	−83

Table D2. (continued)

Sample/Well ID	Sample date (YYYY-MM-DD)	Depth (cm)	Temp. (°C) ±0.2°C	Sample density (g cm^{-3}) ±0.001 g cm^{-3}	Sample density at halite saturation (g cm^{-3}) ±0.001 g cm^{-3} (measured)	Sample density at halite saturation (g m^{-3}) ±0.001 g cm^{-3} (modelled)	Model residual (kg m^{-3}) quasi-salinity	Degree of halite saturation (kg m^{-3}) quasi-salinity ± 2 kg m^{-3}
BLM-93A	2020-09-19		17.5	NA	1.2078	1.2072	−0.6	NA
BLM-93A	2020-11-23		30.0	NA	1.2015	1.2017	0.2	NA
BLM-93A	2020-11-23		31.9	NA	1.2003	1.2009	0.6	NA
BLM-93A	2020-11-23		33.9	NA	1.1995	1.2000	0.5	NA
BLM-93C	2019-09-08		27.5	1.206	1.2068	1.2063	−0.5	0
BLM-93C	2019-09-08		21.3	1.209	1.2092	1.2091	−0.1	0
BLM-93C	2019-09-08		15.4	1.211	1.2112	1.2113	0.1	0
BLM-93C	2019-09-08		7.8	1.214	1.2136	1.2131	−0.5	1
BLM-93C	2019-09-08		16.8	NA	1.2104	1.2109	0.5	NA
BLM-93C	2019-09-08		32.0	NA	1.2037	1.2042	0.5	NA
BLM-93C	2020-06-04		30.1	1.204	1.2055	1.2051	−0.4	−1
BLM-93C	2020-06-04		27.5	1.206	1.2064	1.2063	−0.1	−1
BLM-93C	2020-06-04		21.5	1.209	1.2083	1.2090	0.7	0
BLM-93C	2020-06-04		15.6	1.211	1.2107	1.2113	0.6	−1
BLM-93C	2020-06-04		5.1	1.214	1.2136	1.2132	−0.4	1
BLM-93C	2020-06-04		7.5	1.214	1.2135	1.2131	−0.4	1
BLM-93C	2020-06-04		17.3	NA	1.2101	1.2107	0.6	NA
BLM-93C	2020-06-04		18.9	NA	1.2099	1.2101	0.2	NA
BLM-93C	2020-06-04		19.9	NA	1.2087	1.2097	1.0	NA
BLM-93C	2020-06-04		33.4	NA	1.2033	1.2037	0.4	NA
BLM-93C	2020-09-19		34.3	1.201	1.2027	1.2033	0.6	−2
BLM-93C	2020-09-19		30.0	1.204	1.2053	1.2051	−0.2	−1
BLM-93C	2020-09-19		32.0	1.204	1.2040	1.2042	0.2	0
BLM-93C	2020-09-19		27.5	1.206	1.2062	1.2063	0.1	0
BLM-93C	2020-09-19		21.6	1.209	1.2085	1.2089	0.4	0
BLM-93C	2020-09-19		15.3	1.211	1.2109	1.2114	0.5	0
BLM-93C	2020-09-19		0.5	NA	1.2124	1.2126	0.2	NA
BLM-93C	2020-09-19		8.9	NA	1.2130	1.2129	−0.1	NA
BLM-93C	2020-09-19		18.1	NA	1.2098	1.2104	0.6	NA
BLM-93C	2020-09-19		19.3	NA	1.2094	1.2099	0.5	NA
BLM-93C	2020-12-21		18.1	NA	1.2099	1.2104	0.5	NA
Rest Stop	2020-01-29		17.6	NA	1.2015	1.2024	0.9	NA
Rest Stop	2020-01-29		18.5	NA	1.2013	1.2021	0.8	NA
Rest Stop	2020-01-29		30.0	NA	1.1970	1.1970	0.0	NA
Rest Stop	2020-01-29		32.0	NA	1.1962	1.1961	−0.1	NA
Rest Stop	2020-01-29		33.9	NA	1.1949	1.1953	0.4	NA

Table D3. Coefficients for the equation of brine density at halite saturation at different temperatures (equation D7). These values have been averaged to create the aggregate curve, where ρ_0 (the sample's density at halite saturation at 0°C) varies between samples (Table D4) but all other model inputs remain the same.

Sample ID	A	B	C	ρ_0
BLM-93	4.18494E−07	−2.75785E−05	2.06611E−04	1.21454
BLM-45	4.66153E−07	−2.99339E−05	2.42244E−04	1.21422
BLM-37	4.64628E−07	−2.90131E−05	2.11019E−04	1.21407
BLM-93C	3.15457E−07	−2.38555E−05	1.62230E−04	1.21299
BLM-41	3.62281E−07	−2.99152E−05	3.25970E−04	1.21140
BLM-34, 63, 64	5.68100E−07	−3.97025E−05	4.45772E−04	1.21035
BLM-50, 43A, 31, 12	2.83540E−07	−2.67454E−05	3.05225E−04	1.20957
BLM-53, 93A	4.64472E−08	−1.71115E−05	2.24342E−04	1.20906
Access Rd. May 2019, Jan. 2020	3.33024E−07	−2.98090E−05	3.52319E−04	1.20731
BLM-53A, Access Rd. Jan 2019	1.37812E−07	−1.78710E−05	1.59853E−04	1.20686
Aggregate	3.39594E−07	−2.71536E−05	2.63559E−04	(see Table D4)

Table D4. Inputs for ρ_0 (the halite saturated density at 0°C) for equation D7 for different sample compositions. Increasing Mg^{2+} and K^+ in wells from past studies (Turk, 1973; Lines, 1979) are associated with increasing ρ_0 values.

Sample/Well ID	ρ_0 (halite saturated density at 0°C)	
Rest Stop	1.2044	increasing Mg^{2+} and $K^+ \Rightarrow$
BLM-53A, Access Rd. Jan 2019	1.2069	
Access Rd. May 2019, Jan. 2020	1.2073	
BLM-53B	1.2091	
BLM-93A	1.2091	
BLM-50B, 50A,43A,31,12	1.2096	
BLM-53	1.2101	
BLM-34,63,64	1.2104	
BLM-41	1.2114	
BLM-93C	1.2124	
BLM-37	1.2141	
BLM-45	1.2142	
BLM-93	1.2145	

Table D5. Average impact of changing temperature on halite saturation in quasi-salinity units (change in quasi-salinity for 1°C temperature change) in Bonneville Salt Flat samples (from Fig. D4). An increase in temperature will make a brine more halite undersaturated by increasing halite's solubility. Brines become more halite saturated as temperature decreases (Fig. D4). The change in quasi-salinity with a daily temperature change of 5, 10 and 15°C was calculated. To make these results more broadly comparable, they were converted from quasi-salinity units to TDS using equation D-4. Because of variability in temperature, there is decreased accuracy in this calculated salinity. These values indicate that a 10°C brine temperature change could change the salinity of brines in equilibrium with halite by 1.2 kg m^{-3} (quasi-salinity). This is comparable to a change in total dissolved solids by *ca* 6.9 g L^{-1}

Change in degree of halite saturation with temperature

Quasi-salinity slope (kg m^{-3}°C^{-1})	Quasi-salinity change (kg m^{-3})			Comparable total dissolved solids change (g L^{-1})		
	ΔT 5°C	ΔT 10° C	ΔT 15°C	ΔT 5°C	ΔT 10° C	ΔT 15°C
−0.1165	−0.6	−1.2	−1.8	−3.5	−6.9	−10.3

APPENDIX E. DUST TRAP SEDIMENTS

Soluble materials were dissolved from samples before making final measurement of sediments collected with dust traps (Tables E1 and E2). A sediment density of 1.6 g cm^{-3} was used to calculate the depositional rate as mm $year^{-1}$. A parallel experiment to estimate rates of sediment reworking and deposition measured sediments

Table E1. Dust trap locations, data sampling interval and insoluble material depositional rate.

Dust trap ID	Latitude	Longitude	Deployment date (YYYY-MM-DD)	Collection date (YYYY-MM-DD)	Insoluble material depositional rate (mg m^{-2} day^{-1})
D1	40.748810°	−113.914650°	2016-05-27	2016-09-04	56
			2016-09-04	2017-01-16	454
			2017-01-16	2017-05-10	831
			2017-05-10	2017-07-27	133
			2017-07-27	2017-09-14	121
			2017-09-14	2018-03-09	76
			2018-03-09	2018-05-03	159
			2018-05-03	2018-10-01	109
D1-V2			2017-09-14	2018-03-09	91
			2018-03-09	2018-10-01	118
D2	40.764170°	−113.881940°	2016-04-10	2016-05-27	77
			2016-05-27	2016-09-04	45
			2016-09-04	2017-01-07	281
			2017-01-07	2017-06-27	153
D3	40.765730°	−113.784140°	2016-05-10	2016-06-28	72
			2016-06-28	2016-09-04	29
			2016-09-04	2016-11-06	179
			2016-11-06	2017-05-10	162
			2017-05-10	2017-09-14	93
			2017-09-14	2018-05-03	92
			2018-05-03	2018-10-01	51
D4	40.812030°	−113.785620°	2016-09-06	2016-11-06	365
			2016-11-06	2017-05-10	111
			2017-05-10	2017-09-14	183
			2017-09-14	2018-05-03	71
			2018-05-03	2018-10-01	110

Table E2. Synthesis of dust trap depositional rates.

Dust Trap	Average depositional rate (mg m^{-2} day^{-1})	Time weighted average depositional rate (mg m^{-2} day^{-1})	Standard deviation (mg m^{-2} day^{-1})	Median depositional rate (mg m^{-2} day^{-1})
D1	215	207	231	120
D2	139	157	91	115
D3	97	100	51	92
D4	168	131	105	111
Aggregate	163	155	164	111

Table E3. Calculated rates of surficial reworking and deposition from cloths placed on the surface of the saline pan. Cloths were secured on the surface of the salt flat at the end of the desiccation period and left for several months to years. The cloths were collected, with care taken to only collect material above the cloth, including salt and sediments that were deposited or reworked onto the cloths. Halite was dissolved from these samples and the remaining non-soluble material was weighed to determine the rate of reworking and deposition.

Sample ID	Date installed (YYYY-MM-DD)	Date collected (YYYY-MM-DD)	Depositional/reworking rate (mg m^{-2} day^{-1})
Weather station blue	2017-12-08	2018-10-12	58
Weather station white	2017-12-08	2018-10-12	68
Weather station blue	2017-12-08	2020-09-19	257
LEMSA	2019-09-08	2020-09-19	387

accumulated on top of cloths placed at the surface (Table E3). The surface cloths were placed before the flooding period and were subsequently covered by reworked sediments (primarily gypsum), bottom-growth halite and efflorescence. They were collected with care being taken to only gather the material on top of the cloth.

APPENDIX F. PETROGRAPHIC SAMPLES AND PHOTOMICROGRAPHS

This appendix includes petrographic sample information, a selection of photomicrographs and a paragenetic diagram. Petrographic sample information includes collection location, sample depth, type and thick-section thickness (Tables F1 and F2). Photomicrographs (Figs F1 to F3 and https://doi.org/10.5281/zenodo.4197277) include representative examples of evaporite morphologies. The syndepositional sequence and petrographic features are outlined in the paragenetic diagram (Fig. 4). Subsurface samples collected with a continuous track-mounted vibracore and free-standing vibracore were *ca* 7.5 cm in diameter. Supplementary photomicrographs and photomosaics of thick sections can be found online at https://doi.org/10.5281/zenodo.4197277.

Table F1. Petrographic sample locations, depths and descriptions

Sample ID	Collection date (YYYY-MM-DD)	Latitude	Longitude	Sample type	Epoxy colour	Sample depth (cm)	Section thickness (mm)
D-12B	2016-09-07	40.8417149°	−113.7687711°	Slab	–	0.0–15.6	–
D-12B_9				Large format thick section	Pink	0.0–5.0	1.60
D-12B_10						3.8–8.6	1.70
D-12B_11						10.5–14.9	1.50
D-12B_12						0.0–5.0	1.55
D-12B_13						10.3–15.4	1.45
D-12B_14						3.9–8.9	1.45
D-35	2016-09-07	40.784215°	−113.829461°	Slab	–	0.0–7.9	-
D-35_5				Small format thin section	Clear	~30–40	0.03
D-35_1				Large format thick section	Clear	0.0–5.8	2.95
D-35_9					Clear	~65–75	2.95
D-35_15					Pink	0–4.3	1.45
D-35_16					Pink	4.6–7.6	1.70
D-35_17					Pink	0.0–4.0	1.45
D-35_18					Pink	4.2–7.8	1.45
D-42_11	2016-09-07	40.759968°	−113.852619°	Large format thick section	Clear	~70–80	2.90
D-45	2016-09-07	40.745262°	−113.860979°	Slab	–	0.0–12.7	–
D-45_25				Large format thick section	Pink	0.0–5.7	1.70
D-45_26					Pink	6.5–12.3	1.45
D-45_27					Pink	0.0–5.7	1.45
D-45_28					Pink	6.9–12.7	1.45
D-45-1					Clear	0.0–6.0	2.85
D-54A	2016-09-07	40.756302°	−113.873357°	Slab	–	0.0–11.3	–
D-54A_19				Large format thick section	Pink	0.0–4.5	1.65
D-54A_20						4.1–7.6	1.70
D-54A_21						0.0–4.5	1.60
D-54A_22						4.2–7.6	1.70
D-54B_23						7.8–13	1.60
D-54B_24						7.8–12.7	1.60
D-56	2016-09-07	40.762998°	−113.830926°	Slab	-	0.0–11.3	-
D-56_1-A				Large format thick section	Clear	0.0–5.4	2.90
D-56_1-B					Clear	5.6–11	2.90
D-56_5					Pink	5.7–11.1	1.70
D-56_6					Pink	0.0–5.5	1.95
D-56_7					Pink	5.7–11.2	1.60
D-56_8					Pink	0.0–5	1.50
D-60	2016-09-07	40.778657°	−113.823330°	Slab	–	0.0–11.3	-
D-60_1-blue				Large format thick section	Blue	0.0–5.3	3.00
D-60_2-blue					Blue	5.35–10.4	3.10
D-60_3-blue					Blue	0.0–5.5	3.10

Table F1. (continued)

Sample ID	Collection date (YYYY-MM-DD)	Latitude	Longitude	Sample type	Epoxy colour	Sample depth (cm)	Section thickness (mm)
D-60_4-blue					Blue	5.7–11.3	3.00
D-60_1					Pink	0.0–5.4	1.30
D-60_2					Pink	5.4–10.4	1.47
D-60_3					Pink	0.0–5.9	1.70
D-60_4					Pink	5.8–11.2	1.90
OffTack3	2017-08-10	40.77751°	−113.84327°	Slab	–	0.0–5.9	-
TS-OffTack3				Large format thick section	Clear	0.0–5.9	2.90
OffTrack1	2017-07-26	40.78222°	−113.85865°	Slab	-	–	-
TS-OffTrack1				Large format thick section	Clear	0.0–6.2	1.10
OnTrack1	2017-07-26	40.78196°	−113.85838°	Slab	-	–	-
TS-OnTrack1				Large format thick section	Clear	0.0–5.9	0.55
BSF-EQX-WS1_55-62cm (D-35)	2019-09-09	40.812520°	−113.771940°	Large format thick section	Blue	55–62	0.10
BSF-EQX-WS1_63-70cm (D-35)	2019-09-09	40.812520°	−113.771940°	Large format thick section	Blue	63–70	1.50
BSF-EQX-WS1_71-78cm (D-35)	2019-09-09	40.812520°	−113.771940°	Large format thick section	Blue	71–78	1.50
D-35-C	2019-09-09	40.812520°	−113.771940°	Salt crystals	–	65–75	-

Table F2. Location and thickness of thick section samples from evaporation pond for potash production

Sample ID	Latitude	Longitude	Epoxy colour	Section thickness (mm)
IP-30	40.724295°	−113.980502°	Blue	1.35
IP-29	40.724295°	−113.980502°	Blue	1.29

COLOR

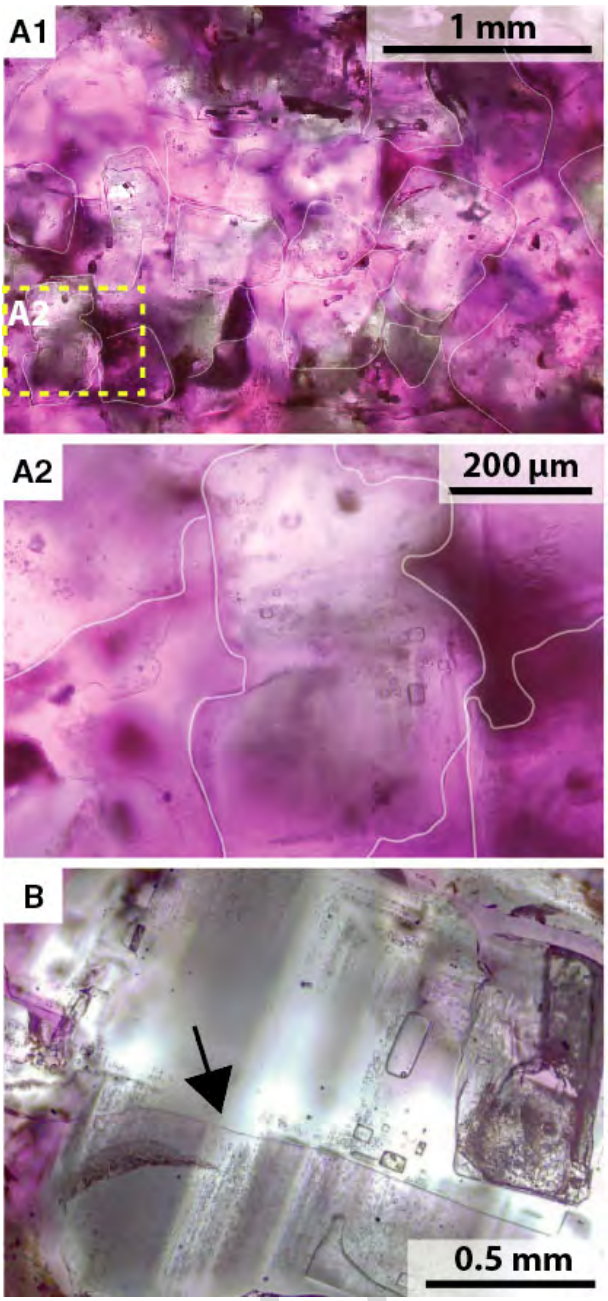

Fig. F1. Microscopic vug-filling crystals and halite overgrowths. (A) Microscopic vug-filling halite crystals range in size from 0.2 to 1 mm wide (from D-45). These crystals occur in voids that are directly connected to surficial efflorescent growths (e.g., Fig. 6B). White outline added to emphasise crystal edges. (A2) Faint fluid inclusion assemblages. (B) Intracrystalline void in chevron crystal filled by halite cement with large all-liquid and liquid-vapour inclusions (black arrow points to the contact between the original crystal and cement; from D-54). Images are oriented with stratigraphic up at the top of the page. Pink (rhodamine B dye) epoxy used. Images have different scales. Imaged using plane polarized light.

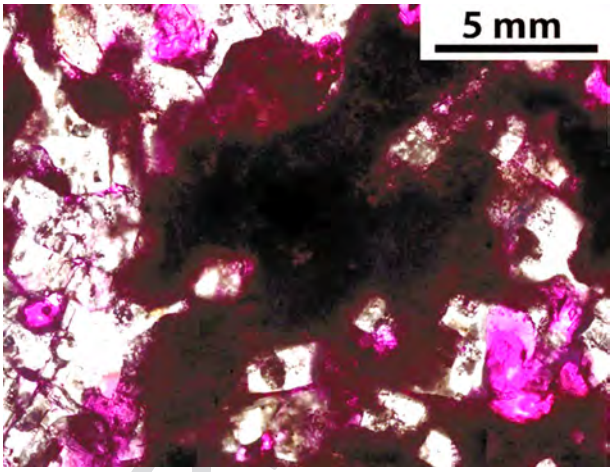

COLOR

Fig. F2. Halite cement crystals in vug filled by gypsum sand (from D-12B) in plane polarized light. Image oriented with stratigraphic up at the top of the page. Pink (rhodamine B dye) epoxy used.

COLOR

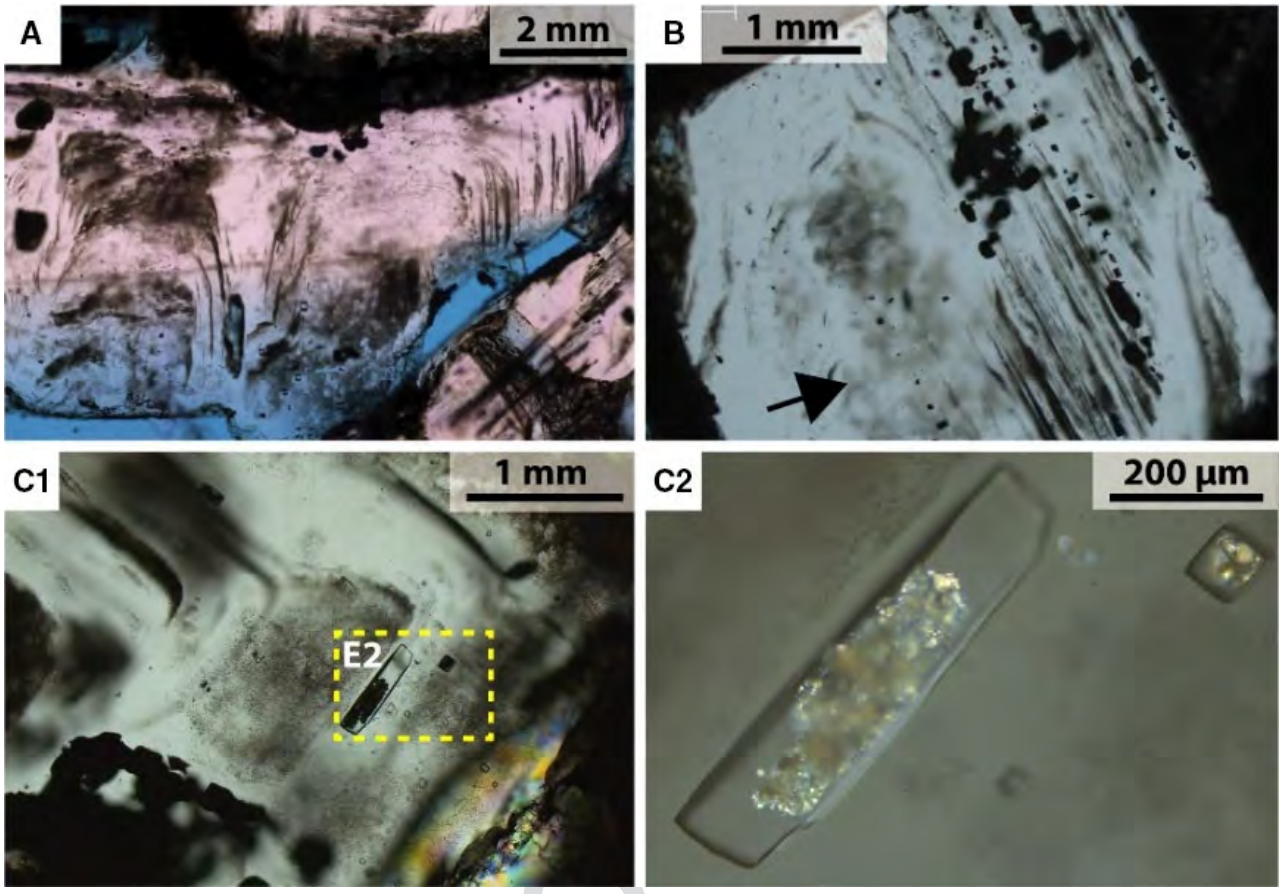

Fig. F3. Deeper (50 to 80 cm depth) diagenetic halite crystals (from D-35). (A) Intergrown halite cement crystals with curving fluid inclusion assemblages and cloudy, inclusion rich sections. (B) Crystal with parallel fluid inclusion assemblages and dissolution features filled by clear to cloudy (black arrow) halite overgrowths. (C1) Halite crystal with parallel to curving fluid inclusion assemblages, a cloudy, fluid inclusion-rich core and solid inclusions of gypsum sand and (C2) large fluid inclusions with accidental daughter crystals of gypsum. Images (A) and (B) are oriented with stratigraphic up at the top of the page. Blue epoxy used in (A-B) and no epoxy used in (C). Images have different scales. Imaged using plane polarized light (A-B) and partially polarized light (C1-C2).

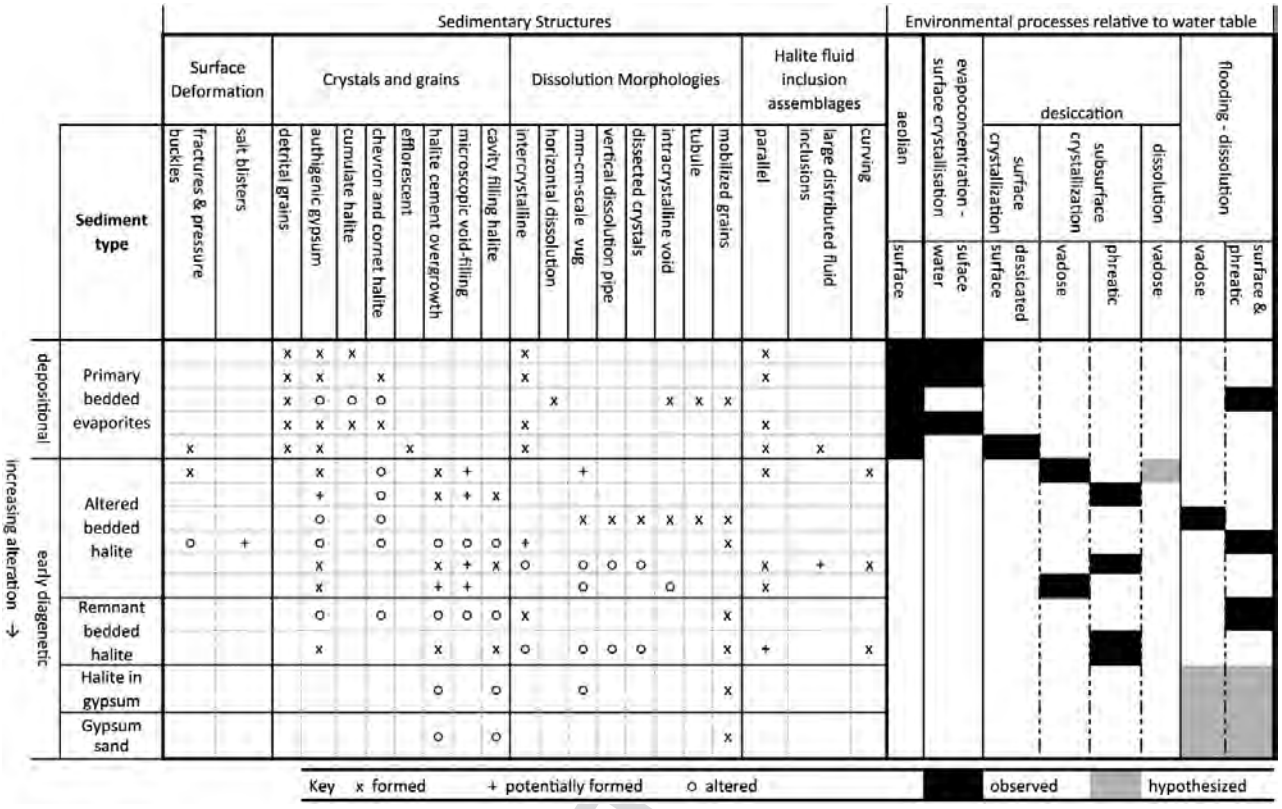

Fig. F4. Paragenetic diagram outlining sediment types, associated sedimentary structures and environmental processes and settings. Sedimentary structures are shown at four scales: surface deformation, crystals and grains, dissolution morphologies and fluid inclusion assemblages in halite. Structures are associated with environmental stages and depth relative to the water level. Structures are denoted with an 'X' if they are being formed, a '+' if they may be formed but evidence is insufficient, or an 'O' if they are being altered during a period. General evolution of bedded evaporite layers across processes is demonstrated by following the development of sedimentary structures downward. This is a general diagram of sediment evolution, in many cases the system may fluctuate between flooding and evapoconcentration, without a desiccation stage in between.

APPENDIX G. GRAIN SIZE DISTRIBUTION AND ANGULARITY IN SAND SAMPLES

Table G1. Gypsum grain sizes and angularity in sediment samples. Core and layer numbers after Bowen *et al.* (2018). An 'x' under ooids present indicates the occurrence of ooids in that sample. Visualization of some of this data available in Bowen *et al.* (2018a).

Core	Latitude	Longitude	Layer	Sample depth (cm)	Angularity	VFS GSD (%)	FS GSD (%)	MS GSD (%)	CS GSD (%)	VCS GSD (%)	Ooids present
SOL	40.763160°	−113.895190°	-	0.5	subangular	10	65	20	5	0	
			-	5.1	subrounded	5	15	70	10	0	
			-	9.9	subangular	0	20	70	10	0	
			-	15	subangular	0	15	70	10	5	
			-	20.1	angular	0	5	25	30	40	
			-	23.4	angular	0	10	20	60	20	
3	40.864656°	−113.756457°	2	5.1	angular	20	74	5	1	0	x
			2	10.2	angular	15	80	5	0	0	x
			2	15.2	angular	10	20	60	10	0	x
			2	20.3	subangular	0	20	70	10	0	x
			2	25.4	subangular	0	25	65	10	0	x
			3	30.5–38.1	subangular	0	10	30	50	10	
12B	40.8417149°	−113.7687711°	2	1.3–5.1	angular	10	20	45	20	5	x
			4	30.5–33	subrounded	5	20	60	15	0	x
			5	33–48.3	subangular	5	20	40	35	0	x
			8	66–68.6	angular	0	5	20	60	15	
18	40.810299°	−113.758703°	2	2.5	angular	10	60	28	2	0	
			2	7.6	subangular	10	50	38	2	0	
			2	12.7	subangular	10	25	60	5	0	
			2	17.8	subrounded	0	20	70	10	0	
			3	25.4–45.7	subangular	5	15	70	10	0	x
			4	45.7–58.4	angular	0	5	50	40	5	x
33	40.800694°	−113.847702°	2	3.8–7.6	subangular	5	60	30	5	0	x
			4	20.3	angular	0	10	90	0	0	
			4	30.5	subangular	0	18	80	2	0	
			4	40.6	subangular	0	10	80	10	0	
			4	50.8	subangular	0	10	40	40	10	
			4	61	subangular	0	10	40	45	5	
35	40.784640°	−113.829890°	-	1.8–2.1	subangular to angular	70.5	19	8.5	2	0	x
			-	4.1–4.4	subangular to rounded	21.5	48	25	6	0	x
			-	4.4–5.1	angular to subangular	50	35	14	1	0	x
			-	5.1–5.8	angular to subangular	10	43	39	8	0	x
			-	5.8–6	subrounded to angular	42	37	18	3	0	x
	40.784215°	−113.829461°	2	1.3–2.5	angular	20	60	19	1	0	
			3	6–6.1	angular to subangular	26	27	40	6	1.5	
			4	25.4–30.5	subrounded	0	10	89	1	0	
			6	33–40.6	angular	0	5	85	10	0	
			8	43.2–50.8	angular	5	5	80	9	1	
			11	96.5–137.2	angular	0	30	10	50	10	x
54	40.756302°	−113.873357°	2	8.9–14	angular	15	75	8	2	0	
			4	26.7–40.6	rounded	0	15	35	40	10	
			6	50.8–63.5	subangular	0	15	40	35	10	
			9	86.4–92.7	angular	0	10	20	30	40	
57	40.765733°	−113.784140°	2	12.7	subangular	5	50	40	5	0	
			2	17.8	subangular	5	50	40	5	0	
			2	2.5	subangular	10	60	28	2	0	
			2	7.6	subangular	10	50	35	5	0	

APPENDIX H. X-RAY COMPUTED TOMOGRAPHY

Several sample sizes (salt block to individual halite crystal) were imaged with X-ray computed tomography (Table H1). Supplementary CT data to this article was processed with the program FIJI and can be found online at https://doi.org/10.5281/zenodo.4167214. Computed tomography volumes were processed with non-local means denoising to remove imaging artifacts (Darbon *et al.,* 2008; Buades *et al.,* 2011). The sigma value for this process is reported in Table H2. CT volumes were also processed by trimming and reorienting samples and applying a threshold to remove the air surrounding the sample [Table H2, threshold value lower (8-bit)].

Total sample porosity was calculated using a lower and upper threshold to designate voxels as air or solid (Table H2). The ratio of solid to air was then calculated to determine the porosity. Permeability (Table H2) was calculated using the binary (solid and air) cube and the methods of Videla *et al.* (2008).

Manuscript received 27 January 2020; revision accepted 21 February 2021

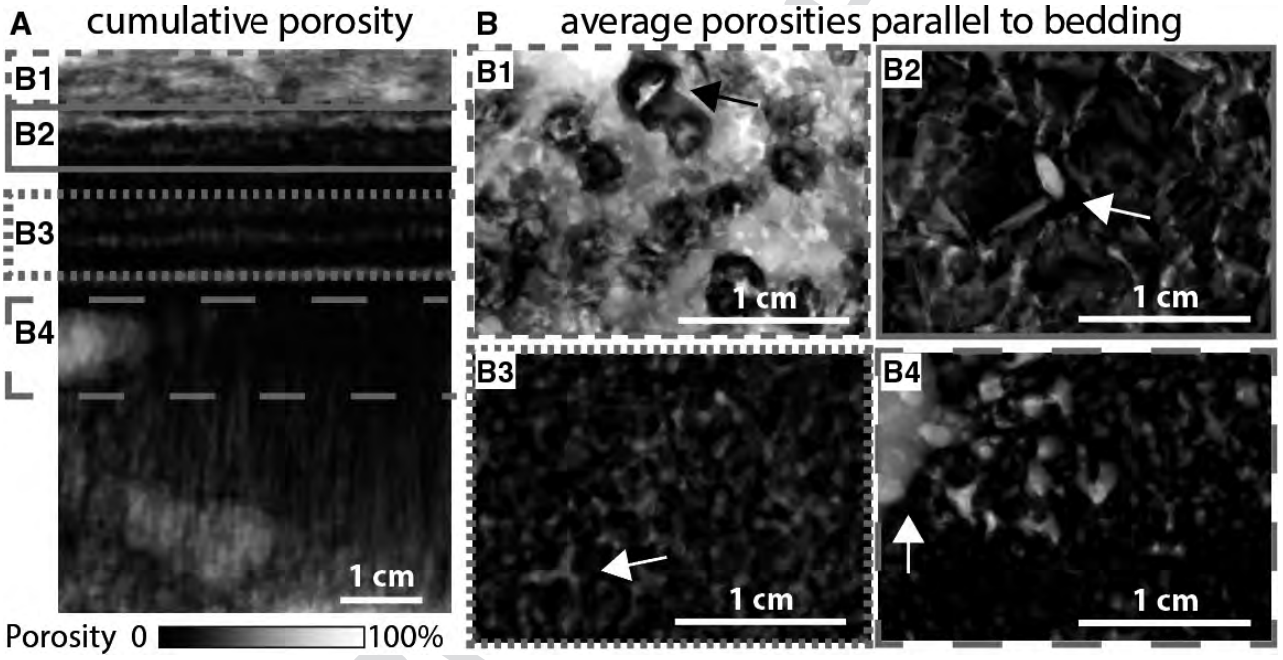

Fig. H1. X-ray computed tomography (CT) porosity data of crust from D-54 (Fig. 7B). Stratigraphic up is the top of the page. Porosity is shown as cumulative values averaged (A) horizontally with the average of slices perpendicular to bedding or (B) vertically with slices parallel to bedding (B1 to B4). Black areas denote lower porosity while light areas denote higher porosity. This sample's bulk porosity is 29% (±5%). The areas denoted to the left of (A) with boxes indicates the sliced and averaged area that is cut parallel to bedding in (B1-B4). (B1) Porous area around bottom growth crystals. (B2) Chevron and cornet crystal layers with planar pores between crystal faces (arrow). (B3) Early vertical dissolution pipes, some occur at the junction of bottom growth crystals (arrow). (B4) Heterogenous horizontal distribution of porosity in altered bedded halite layer with halite cement overgrowths, porosity primarily occurs at vertical dissolution pipes and vugs. Sizeable cm-scale void to the left (arrow).

Table H1. CT sample collection and imaging data and porosity estimates. Sample BSF-54A_CT imaged with a Zeiss Volumax at the University of Minnesota. All other samples imaged with a Zeiss Xradia High-Resolution Micro CT (HRXMT) at the University of Utah

Sample ID	Collection date (YYYY-MM-DD)	Latitude	Longitude	Sample depth (cm)	Resolution (μm/ voxel)	Volume size (voxels)	Images taken	Seconds per image	Voltage (kV)	Current (A)
Syn88F_fluidinclusions_CT	2017-01-12	University of Utah lab	-	1.85	984*1005*986	986	20	80	125	
BSF_35_2.a	2016-09-06	40.784215°	−113.829461°	~20	5.19	992*1013*994	994	9	80	125
BSF_35_2.b	2016-09-06					992*1013*994	994	9	80	125
BSF-54A_CT	2016-09-06	40.756302°	−113.873357°	0–11.5	99.5	1504*985*1046	2000	120	175	3.8
OffTrack_3	2017-08-11	40.777510°	−113.843270°	0–1.7	43.57	1012*1024*1014	1014	6	50	200
OnTrack_3	2017-08-11	40.777510°	−113.843270°	0–1.8	43.57	1012*1024*1014	1014	6	50	200
Salt_flats_no_8 (on track)	2017-07-11	40.782883°	−113.857817°	0–1.4	32.05	450*450* 330	1014	6	50	200
Salt_flats_no_9 (on track)	2017-07-11	40.782883°	−113.857817°	0–1.5	43.57	450*450* 180	1014	6	50	200
Salt_flats_no_14_GG (off track)	2017-07-11	40.782883°	−113.857817°	0–1.9	32.05	450*300* 180	1014	6	50	200

Table H2. Calculated ranges of porosity (using different threshold values) and permeability (calculated using the methods of Videla *et al.* (2008); as well as values used to process samples to remove imaging artifacts. The sigma value is the input used when processing CT data with non-local means denoising (Darbon *et al.,* 2008; Buades *et al.,* 2011)

Sample ID	Threshold value lower (8-bit)	Sigma value (NLM)	Low porosity estimate		High Porosity estimate		Permeability (cm^2)
			Threshold value	Porosity (%)	Threshold value	Porosity (%)	
Syn88F_fluidinclusions_CT	55	25	20	5.8	–	–	–
BSF_35_2.a	1	10	100	16	–	–	–
BSF_35_2.b	1	10	90	3.47	–	–	–
BSF-54A_CT	73	15	130	24	150	33.7	–
Offtrack_3	30	5	60	45	71	25	–
Ontrack_3	30	5	75	20	90	30	–
Salt_flats_no_8	65	5	110	11.4	125	24	5.11E−06
Salt_flats_no_9	30	10	80	10.6	90	19	2.06E−06
Salt_flats_no_14	115	5	125	29.5	130	37	2.89E−06